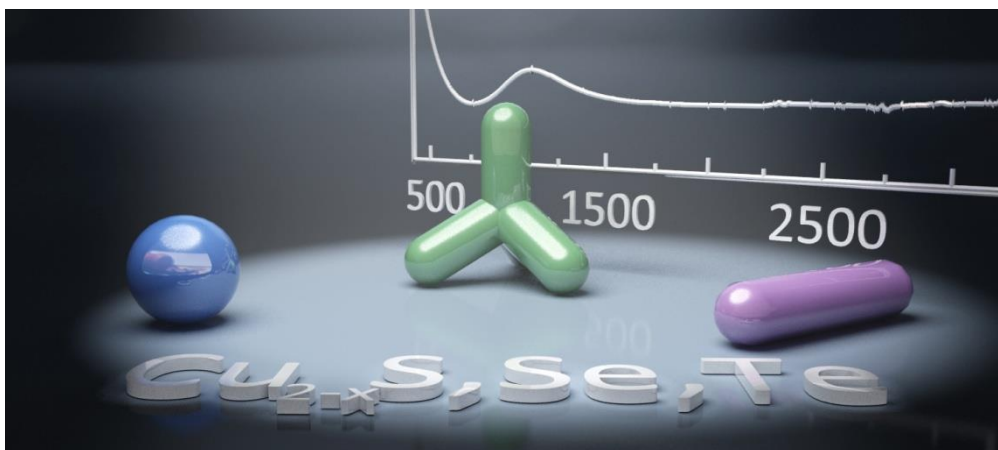

Near-infrared plasmonics with vacancy doped semiconductor nanocrystals

Ilka Kriegel



München, 2013



Near-infrared plasmonics with vacancy doped semiconductor nanocrystals

Ilka Kriegel



Dissertation
an der Fakultät für Physik
der Ludwig-Maximilians-Universität
München

vorgelegt von
Ilka Kriegel
aus
Erlangen

München, 2013

Erstgutachter: Prof. Dr. Jochen Feldmann
Zweitgutachter: Prof. Dr. Christina Scheu
Weitere Prüfungskommissionsmitglieder:
Priv.-Doz. Dr. Bert Nickel (Vorsitzender), Prof. Dr. J. von Delft
Tag der mündlichen Prüfung: 15.11.2013

The graphic on the front page shows the absorbance spectrum of Cu_{2-x}Te nanocrystals in solution. The figure has been designed by **Dipl.-Ing. (FH) Christoph Hohmann**, Nanosystems Initiative Munich.

Für Moritz

Abstract

Plasmonics with heavily doped semiconductor nanocrystals (NCs) is an emerging field in NC science. However, impurity doping of NCs remains far from trivial and is, as yet, dominated by a low chemical control over the incorporated dopant atoms. An appealing alternative is vacancy doping, where the formation of vacancies in the structure is responsible for an increased carrier density and elegantly circumvents the issues related to impurity doping. Due to high carrier densities of around 10^{21} cm^{-3} localized surface plasmon resonances (LSPRs) in the near infrared (NIR) are expected, and as such highlighted to close the gap between conventionally doped NCs and noble metal nanoparticles. Copper chalcogenide NCs, namely copper sulfide (Cu_{2-x}S), copper selenide (Cu_{2-x}Se), and copper telluride (Cu_{2-x}Te), are an attractive example of vacancy doped semiconductor NCs, with spectra dominated by intense NIR resonances. Within this study thorough experimental evidence has been given to prove the plasmonic nature of those NIR resonances. By presenting typical plasmonic characteristics, such as refractive index sensitivity of the LSPR, its intrinsic size dependence, plasmon dynamics, or interparticle plasmon coupling, the LSPRs in copper chalcogenide NCs have unambiguously been identified. The chemical nature of vacancy doping turns out to deliver an additional, highly attractive means of control over the LSPR in vacancy doped copper chalcogenide NCs. Through chemical tailoring of the copper vacancy density via controlled oxidation and reduction, as shown in this study, a reversible tuning of the LSPR over a wide range of frequencies in the NIR (1000 - 2000 nm) becomes feasible. This highlights copper chalcogenide NCs over conventional plasmonic materials. Notably, the complete suppression of the LSPR uncovers the excitonic features present only in the purely semiconducting, un-doped NCs and reveals the unique option to selectively address excitons and highly tunable LSPRs in one material (bandgap $E_g \sim 1.2 \text{ eV}$). As such, copper chalcogenide NCs appear to hold as an attractive material system for the investigation of exciton plasmon interactions. Indeed, a quenching of the excitonic transitions in the presence of the developing LSPR is demonstrated within this work, with a full recovery of the initial excitonic properties upon its suppression. A theoretical study on the shape dependent plasmonic properties of Cu_{2-x}Te NCs reveals a deviation from the usual Drude model and suggests that the carriers in vacancy doped copper chalcogenide NCs cannot be treated as fully free. On the other hand, the Lorentz model of localized oscillators appears to account for the weak shape dependence, as observed experimentally, indicating an essential degree of localization of the carriers in vacancy doped copper chalcogenide NCs.

Taken together, this work delivers a huge step toward the complete optical and structural characterization of plasmonic copper chalcogenide NCs. The advantages of semiconductor NC chemistry have been exploited to provide access to novel plasmonic shapes, such as tetrapods that have not been feasible to produce so far. A precise size, shape and phase control presents the basis for this study, and together with a thorough theoretical investigation delivers important aspects to uncover the tunable plasmonic properties of vacancy doped copper chalcogenide NCs.

Kurzfassung

Plasmonik mit hochdotierten Halbleiternanokristallen ist ein wachsendes Feld. Das Dotieren von Halbleiternanokristallen jedoch stellt sich, aufgrund der geringen Kontrolle über die eingebauten Fremdatome, als schwierig dar. Eine reizvolle Alternative sind selbstdotierende Halbleitermaterialien, die aufgrund von Störstellenformation eine extrem erhöhte Ladungsträgerdichte aufweisen. Somit können die anfallenden synthetischen Schwierigkeiten des herkömmlichen Dotierens elegant umgangen werden. Kupferchalkogenid Nanokristalle, nämlich Kupfersulfid (Cu_{2-x}S), Kupferselenid (Cu_{2-x}Se) und Kupfertellurid (Cu_{2-x}Te) sind interessante Kandidaten solcher selbstdotierender Halbleiter. Mit Ladungsträgerdichten im Bereich von $\sim 10^{21} \text{cm}^{-3}$ sind Partikelplasmonen im Nahinfraroten (NIR) zu erwarten. In dieser Arbeit wurde der plasmonische Charakter dieser Resonanzen im NIR identifiziert indem verschiedene plasmonische Eigenschaften getestet wurden. Dazu gehören die Empfindlichkeit des Partikelplasmons gegenüber dem Brechungsindex des umgebenden Mediums, die Größenabhängigkeit, die Ladungsträgerdynamik und die Kopplung der Partikelplasmonen. Selbstdotierende Kupferchalkogenid Nanokristalle schließen mit Plasmonenresonanzen im NIR die Lücke zwischen metallischen Nanopartikeln, mit Plasmonenresonanzen im sichtbaren und dotierten Halbleiternanokristallen, mit Plasmonenresonanzen im Fern- bis Mittelinfraroten. Der chemische Charakter der Selbstdotierung durch Störstellenformation bringt eine extrem ansprechende Möglichkeit zur Kontrolle über die Plasmonenresonanz mit sich. Durch das chemische Manipulieren der Störstellendichte kann die Ladungsträgerdichte und somit die Plasmonenresonanz über einen weiten Frequenzbereich (1000-2000 nm) gezielt abgestimmt werden. Die komplette Unterdrückung der Plasmonenresonanz legt die exzitonischen Charakteristika der undotierten Nanokristalle frei und demonstriert somit die Möglichkeit in Kupferchalkogeniden selektiv auf Exzitonen und Partikelplasmonen zugreifen zu können (Bandlücke $E_g \sim 1.2 \text{ eV}$). Somit erscheinen Kupferchalkogenid Nanokristalle als interessante Materialsysteme für die Untersuchung von Exziton-Plasmon Wechselwirkungen. Tatsächlich wurde in dieser Arbeit ein Einfluss des sich entwickelnden Partikelplasmons auf die exzitonischen Eigenschaften festgestellt, der durch die komplette Unterdrückung des Plasmons wieder rückgängig gemacht werden kann. Obwohl in dieser Arbeit den Kupferchalkogenid Nanokristallen typische plasmonische Eigenschaften nachgewiesen werden konnten, zeigt eine theoretische Untersuchung eine Abweichung vom üblichen Drude-Modell auf. Weiterhin wurde gezeigt, dass die schwache Morphologieabhängigkeit der Plasmonenresonanzen besser zu beschreiben ist mit dem Lorentz-Modell für lokalisierte Oszillatoren und somit einen gewissen Anteil an Lokalisation der Ladungsträger in Kupferchalkogeniden vorschlägt.

Zusammenfassend wurde in dieser Arbeit ein großer Schritt zum Verständnis der optischen und strukturellen Eigenschaften von plasmonischen Kupferchalkogenid Nanokristallen getan. Die Vorteile der Halbleiternanokristall Chemie wurden ausgenutzt, um den Zugang zu neuen plasmonischen Morphologien, wie Tetrapoden zu ermöglichen. Die präzise Kontrolle über Größe, Form und Phase bilden die Basis dieser Arbeit, um zusammen mit einer theoretischen Untersuchung die wichtigsten Aspekte der plasmonischen Eigenschaften von Kupferchalkogenid Nanokristallen zu bestimmen.



List of Publications

The thesis is based on the following publications:

Tuning the light absorption of Cu_{1.97}S nanocrystals in supercrystal structures

I. Kriegel, J. Rodríguez-Fernández, E. Da Como, A. Lutich, J. Szeifert, J. Feldmann, Chem. Mater. 23, 1830 (2011)

Tuning the Excitonic and Plasmonic Properties of Copper Chalcogenide Nanocrystals

I. Kriegel, C. Jiang, J. Rodríguez-Fernández, R. D. Schaller, D. V. Talapin, E. da Como, and J. Feldmann, J. Am. Chem. Soc. 134, 1583–1590 (2012)

Shedding Light on Vacancy-Doped Copper Chalcogenides: Shape-Controlled Synthesis, Optical Properties, and Modeling of Copper Telluride Nanocrystals with Near-Infrared Plasmon Resonances

I. Kriegel, J. Rodríguez-Fernández, A. Wisnet, H. Zhang, C. Waurisch, A. Eychmüller, A. Dubavik, A. O. Govorov, and J. Feldmann, ACS Nano, accepted (2013), Doi: 0.1021/nn400894d

Further scientific publications:

Charge transfer excitons in polymer/fullerene blends: the role of morphology and chain conformation,

M. Hallermann, I. Kriegel, E. Da Como, J. M. Berger, E. von Hauff, J. Feldmann, Adv. Funct. Mater. 19, 3662-3668 (2009)

Exciton-plasmon interactions in CdTe-Cu_{2-x}Te heterostructures

I. Kriegel, J. Rodríguez-Fernández, A. Wisnet, A. O. Govorov, J. Feldmann, in preparation

Graphene oxide directed self-assembly of Cu_{2-x}S nanoparticles into electronically coupled hybrid structures

S. Neyshtadt, I. Kriegel, S. Hug, B. Lotsch, J. Rodríguez-Fernández, E. Da Como, J. Feldmann, in preparation

Conference contributions

Synthesis and optical properties of copper sulfide nanocrystals,

I. Kriegel, J. Rodríguez-Fernández, E. Da Como, C. Mauser, J. Feldmann (Poster) ‘NANAX 4 - Nanoscience with Nanocrystals International Conference’, Tutzing, Germany (2010)
honored with the **Poster-Award**

Tuning the light absorption properties of Cu_{1.97}S nanocrystals by supercrystal formation,

I. Kriegel, J. Rodríguez-Fernández, E. Da Como, C. Mauser, J. Feldmann (Poster) ‘3rd EuCheMS Chemistry Congress’, Nuremberg, Germany (2010)

Tuning light absorption in close-packed Cu_{1.97}S nanocrystals arrays,

I. Kriegel, J. Rodríguez-Fernández, E. Da Como, J. Feldmann (Poster) ‘NIM Winter School’, St Christoph, Österreich (2011)

Tuning the excitonic and plasmonic properties of copper chalcogenide nanocrystals,

I. Kriegel, J. Rodríguez-Fernández, C. Jiang, R. D. Schaller, D. V. Talapin, E. da Como, and J. Feldmann ‘CeNS Workshop 2011 - Nanosciences: From molecular systems to functional materials’ (Poster), Venice, Italy (2011)

Excitons and localized surface plasmons in copper chalcogenide nanocrystals,

I. Kriegel, C. Jiang, J. Rodríguez-Fernández, R. D. Schaller, D. V. Talapin, E. da Como, and J. Feldmann, (Presentation) ‘MRS Fall Meeting’, Boston, Massachusetts, USA (2011)

The role of plasmon formation on excitons in copper chalcogenide nanocrystals,

I. Kriegel, C. Jiang, J. Rodríguez-Fernández, R. D. Schaller, D. V. Talapin, E. da Como, and J. Feldmann, (Presentation) ‘International Conference on Quantum Dots’, Santa Fe, New Mexico, USA (2012)

Synthesis and Optical Properties of Cu_{2-x}Te Nanocrystals of Various Shapes,

I. Kriegel, J. Rodríguez-Fernández, A. Wisnet, H. Zhang, C. Waurisch, A. Eychmüller, A. Dubavik, A. O. Govorov, and J. Feldmann (Poster) ‘Multifunctional, Hybrid and Nanomaterials’, Sorrento, Italy





Contents

Abstract.....	I
Kurzfassung.....	III
List of Publications	V
Conference contributions	VI
Contents	IX
I. Introduction	1
II. Vacancy doping in copper chalcogenide nanocrystals: semiconducting and metallic properties.....	5
II.1 Synthesis and optical properties of semiconductor nanocrystals.....	6
II.1.1 Synthesis of semiconductor nanocrystals.....	6
II.1.2 Optical properties of semiconductor nanocrystals	7
II.2 Plasmon resonances in metallic nanoparticles	12
II.3 Vacancy-doped semiconductor nanocrystals: copper chalcogenides	26
II.3.1 The role of stoichiometry, crystal structure and copper vacancies	27
II.3.2 Physical properties of vacancy doped copper chalcogenides.....	28
II.4 Copper chalcogenide nanocrystals: State of research and open questions	29
III. Experimental methods and sample preparation	31
III.1 Characterization of nanocrystals: structure, shape and composition	31
III.1.1 Structural characterization with X-ray diffraction	31
III.1.2 Electron microscopy for the investigation of the nanocrystal shape and composition	32
III.1.3 FTIR-spectroscopy: a tool to identify surface ligands	36
III.2 Optical spectroscopy	37
III.2.1 Absorption and scattering.....	37
III.2.2 Photoluminescence	41
III.2.3 Pump-probe spectroscopy	43
III.3 Sample preparation	44

III.3.1	Synthesis of Cu_{2-x}S superlattices	44
III.3.2	Synthesis of stoichiometric and copper deficient copper chalcogenide nanocrystals	45
III.3.2.1	Synthesis of copper chalcogenide nanocrystals	45
III.3.2.2	Oxidation and reduction experiments	46
III.3.3	Ion exchange for the synthesis of Cu_{2-x}Te nanocrystals of various shapes	47
III.3.3.1	Synthesis of Cd based nanocrystals of various shapes	47
III.3.3.2	Cation exchange reactions to synthesize Cu_{2-x}Te nanocrystals of various shapes	50
IV.	Identifying the plasmonic nature of the near-infrared resonances in copper chalcogenide nanocrystals	53
IV.1	Localized surface plasmon resonances in copper chalcogenide nanocrystals	54
IV.1.1	Refractive index sensing with copper chalcogenide nanocrystals	57
IV.1.2	Intrinsic size effect of the localized surface plasmon resonance in Cu_{2-x}S nanocrystals	59
IV.1.3	Near-infrared plasmon dynamics in copper chalcogenide nanocrystals	60
IV.2	Interparticle plasmon coupling of Cu_{2-x}S nanocrystals in close packed superlattice arrays	64
IV.2.1	Cu_{2-x}S nanocrystal superlattice arrays	64
IV.2.2	Blue-shift of the plasmon resonance upon ligand induced disassembly	65
IV.3	Chapter Summary	68
V.	Tuning the excitonic and plasmonic properties of copper chalcogenide nanocrystals	69
V.1	Excitonic and plasmonic properties of Cu_{2-x}S nanocrystals	70
V.2	Tuning the plasmonic properties upon controlled oxidation	73
V.3	Suppressing the plasmon resonance via chemical reduction	76
V.4	Probing the causes of copper vacancy formation	78
V.5	Plasmon induced quenching of the excitonic transitions	79
V.6	Chapter summary	82

VI. Free carriers or carrier localization? – Deviation from the usual Drude model	83
VI.1 Shape dependent extinction of Cu_{2-x}Te nanocrystals.....	84
VI.2 Optical modeling of Cu_{2-x}Te nanocrystals of various shapes	86
VI.3 Shape dependent near-field properties of Cu_{2-x}Te nanocrystals	95
VI.4 Chapter summary	96
VII. Conclusions and outlook	97
Appendix	101
Abbreviations	111
Bibliography	113
Acknowledgements	127



I. Introduction

In the past an intensive growth of activities in the field of nanoparticle science has emerged.[1-17] The changes of their optical properties, when reaching length scales of nanometers, are of fundamental interest. Depending on the material investigated it is a different cause that leads to their extraordinary optical characteristics. For semiconductor nanocrystals (NCs) huge efforts have been made to synthesize highly sophisticated shapes, thereby offering an excellent control over their morphology and composition.[14-16] The so created novel nanostructures require an exact understanding of their size and shape dependent optical properties.[1,3] In semiconductor NCs, it is the confinement of the electronic motion to a length scale that is comparable to the exciton Bohr radius that results in a quantization of the energy levels and leads to their exceptional optical characteristics.[3] Those make them interesting candidates for a number of applications, such as lighting [18] or solar cells.[4,19] In noble metal nanoparticles the optical properties are characterized by a completely different process. When reaching sizes in the nanometer regime strong resonances are observed arising from the collective oscillations of the electrons in the conduction band.[5,13] These oscillations can be stimulated by an electromagnetic wave resulting in the so called localized surface plasmon resonance (LSPR).[5,13] Due to their remarkable light scattering and absorption properties plasmonic nanoparticles attract an ever growing attention, finding application in biosensing,[20,21] spectroscopy techniques, such as surface enhanced Raman spectroscopy (SERS),[22] or photothermal therapy.[23] LSPRs have so far mostly been investigated in noble metal nanostructures such as gold, silver or copper. Charge carrier densities in the range of 10^{22} – 10^{23} cm^{-3} lead to LSPRs in the visible spectral range. Size and geometry of those nanostructures largely influence the LSPR and provide to a certain degree the tunability of the optical properties.[24] However, this tunability is limited to the stage of synthesis. Thereafter the plasmon resonance is defined and may only be influenced to a small extent by changes of the surrounding medium refractive index.[25] Considering that LSPRs are not limited to metallic nanostructures only, but found in any nanostructure providing a

sufficiently high free carrier density, doping appears to be an attractive alternative.[26,27] Efforts to dope semiconductor NCs through the insertion of impurity atoms remains far from trivial, as self-purification during NC growth expels the dopant atom from the crystal to the surface.[28] Due to low carrier densities achieved in this way LSPRs in doped semiconductor NCs are located in the mid to far IR.[20,29,30] A way to overcome these internal barriers is vacancy doping, where vacancies in the structure are responsible for an increased carrier density reaching values up to 10^{21}cm^{-3} . [26,29,31] This extremely high number of carriers confined to a small volume gives rise to LSPRs located in the near-infrared (NIR). As such, vacancy doped semiconductor NCs close the gap between conventional plasmonic and impurity doped materials. Furthermore, vacancy doped semiconductor NCs may cover both, semiconducting and metallic properties, depending on their level of doping. This is achieved through the exact tailoring of the vacancy density in the structure and further delivers the opportunity to effectively tune the LSPR.[20,27-35] It is the chemical nature of vacancy doping that promises these attractive characteristics and highlights this type of plasmonic material over conventional metallic nanostructures.[26,29,31,32,34]

Interesting candidates of vacancy doped semiconductor NCs are copper chalcogenides, namely copper sulfide (Cu_{2-x}S), copper selenide (Cu_{2-x}Se), and copper telluride (Cu_{2-x}Te). A particularly interesting feature of copper chalcogenide NCs is their essential degree of doping based on the formation of copper vacancies in the structure.[21,26,27,32,34,36-39] Within this work it has been demonstrated that the high level of vacancy doping is responsible for an increased carrier density that ultimately leads to LSPRs in the NIR. The experimental evidence has been given by probing typical plasmonic characteristics, such as refractive index sensing, size dependence, carrier dynamics, or interparticle plasmon coupling (chapter IV). Another key feature of copper chalcogenide NCs is the possibility to chemically tailor the copper vacancy density. This appealing characteristic allows the reversible tuning of the LSPR over a wide range of frequencies, as demonstrated in chapter V. The control over the vacancy density further facilitates to access excitons and plasmons in one structure, depending on the level of doping. In copper chalcogenide NCs the LSPR comes close in energy to the interband transitions ($E_g \sim 1.2\text{eV}$). [40-42] Thus, a possible influence of the LSPR on the interband transitions is conceivable and has been studied within this work (chapter V). Shape dependent optical properties of copper chalcogenide NCs are provided in Chapter VI. In comparison with theoretical models a basic understanding of the plasmon resonances in this type of material is delivered, uncovering a deviation from the usual Drude model. For a better comprehension of the main findings of this work, at first, a brief introduction to the

theoretical background is provided. In particular the optical properties of semiconducting and metallic nanoparticles, together with a discussion on vacancy doping in copper chalcogenides is given in chapter II. This chapter concludes by presenting the state of research in the field of copper chalcogenide NCs unveiling open questions, which provide the basis of this work. The experimental techniques employed to address those points, together with a detailed description of the sample preparation are summarized in chapter III. Chapter IV to VI present the results obtained within this work, which concludes with a summary of the main findings and an outlook to possible applications of vacancy doped copper chalcogenide NCs (chapter VII).



II. Vacancy doping in copper chalcogenide nanocrystals: semiconducting and metallic properties

Nanoscale materials are gaining an increasing attention due to their extraordinary optical properties arising from the confinement in size. At the length scale of those nanosized materials new properties result from scaling in the nanometer regime. In semiconductor NCs, a striking property is the change of the optical spectra as a function of NC size. With reduced sizes the electronic excitations shift to higher energies and most of the oscillator strength is concentrated in a few transitions.[43] Similarly, scaling in the nanometer regime largely influences the optical response of metallic nanoparticles, resulting in the so called localized surface plasmon resonances (LSPRs).[44] Those are also size and shape dependent. While in metal nanoparticles the optical properties are governed by the high charge carrier density ($\sim 10^{22} \text{cm}^{-3}$ in gold), it is the confinement of the electronic motion to a length scale that is comparable to the exciton Bohr radius that is responsible for the exceptional optical properties in semiconductor NCs.[13,44] By means of doping, it is possible to obtain an increased carrier density also in semiconductor NCs. Nevertheless, the carrier densities stay far beyond those of metals, and LSPRs in doped semiconductors are found in the far IR only. In copper chalcogenide NCs, however, this limitation can be overcome. Here, vacancy doping leads to carrier densities of $\sim 10^{21} \text{cm}^{-3}$. In the following chapter the basic principles of semiconductor NC synthesis will be presented. Thereafter, theoretical concepts will be discussed covering the exceptional optical properties of those nanosized objects. Later in this chapter, vacancy doping in copper chalcogenides will be introduced and the state of research for copper chalcogenide NCs given.

II.1 Synthesis and optical properties of semiconductor nanocrystals

II.1.1 Synthesis of semiconductor nanocrystals

Wet-chemical synthesis

Emerging advances in NC research allow for the precise synthesis of nanoscale structures with defined geometries, monodisperse sizes, and exact composition. Representative examples of NCs with various shapes and compositions are shown in Figure II-1.

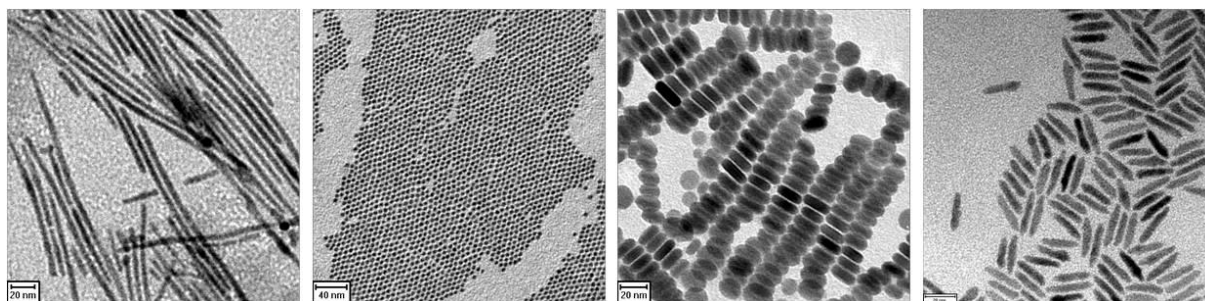


Figure II-1 Representative examples of NCs of various shapes synthesized within this work. From left to right: Cu_{2-x}S nanowires, spheres, disks, and CdS nanorods.

Generally, it is the combination of reactants and organic capping ligands that determines the reaction and controls the shape of the NCs. Their synthesis is evoked by the dramatic decrease in solvability of the reactants in solution leading to the supersaturation of the reaction solution. This is followed by nucleation and growth of the NCs. These are the three stages that control NC synthesis, ensure monodispersity and determine the shape.[13]

Supersaturation and nucleation in NC synthesis is triggered by the injection of a metal-organic precursor into a high boiling point coordinating solvent at sufficiently high temperatures to decompose the reactants. These are the atomic species that constitute the NC and are released rapidly to provoke the sudden supersaturation, finally leading to fast nucleation.[8] In homogeneous nucleation the monomers combine in solution to form the nuclei. When the concentration of precursors drops below a critical level no further nuclei are formed. Thereafter, molecular addition leads to NC growth, which occurs until the equilibrium concentration is reached.[13] Consumption of the reactants via NC growth prevents that new nuclei are formed and the NCs grow evenly. This largely influences size distribution and shape of the NCs.[13] Monodisperse NCs are produced when there is a

temporally discrete nucleation event where all nuclei are formed at once followed by a slower growth on the existing nuclei.[2] Monodispersity can be ensured by stopping the reaction rapidly at a certain stage of reaction. The nucleation process also determines anisotropic growth.[13] The choice of appropriate ligands, according to their binding strength to certain crystallographic facets of the NCs is a key factor here.[14] If the surface ligands bind more strongly to certain facets, those may be blocked. This promotes the growth in specific crystallographic directions only.[8,45] As the synthesis of NCs is controlled through kinetics, the synthesis can be stopped at any stage to allow a metastable shape to be frozen in before equilibrium is reached.[14]

Ion exchange reactions in nanocrystals

Insertion and exchange of ions leading to chemical transformations in semiconducting NCs is known for many years [46-48] and has been proven to occur in diverse structures at room temperature.[47,49,50] This complete exchange enables to move from one crystal lattice with certain composition, crystal structure, and defined optical properties to a completely different material.[46-50] Reactions as such, involving chemical transformations, are for bulk material very slow because of high activation energies, *i.e.*, high temperatures or pressures to force the reaction. Those reaction parameters are incompatible with kinetically controlled non-equilibrium structures as NCs.[49] But for crystals in nanometer size the surface to volume ratio changes kinetics and mechanisms such as to enable similar reactions at ambient conditions.[49] In cation exchange reactions, shape and size of the initial NC is preserved even over multiple complete exchange cycles.[47,49,51] As such, ion exchange is an interesting alternative for the synthesis of certain types of NCs were the direct one pot synthesis of precise shapes with wet-chemical methods is not developed to date.

II.1.2 Optical properties of semiconductor nanocrystals

Typically, NCs reach dimension of a few nanometers only. This confinement in size alters their optical properties significantly with respect to the bulk material. In bulk-like crystals the properties are size independent and only dependent on the chemical composition. When reaching the nanometer regime, however, the size of the particle influences the properties of the crystal. In metals, a number of important physical properties can be described by the free electron model, that is, the valence electrons of the crystal atoms move nearly free through the volume of the metal.[52] However, in semiconductors the electrostatic potential of the ion cores influences the valence electrons in a crystal. Here, the concept of free electrons has to

be expanded taking the periodic potential of the lattice into account. This results in bands of electronic states in the energy space separated by forbidden regions, the so called bandgap.[52,53] In the following, the quantum mechanical solution of the Schrödinger equation for the free electron will be presented; thereafter the influence of the periodic potential will be introduced. Generally the Schrödinger equation is given by $\mathcal{H}\psi = E\psi$. By only taking into account the kinetic energy $\mathcal{H} = \frac{p^2}{2m}$ with the impuls p being $p = -i\hbar \frac{d}{dx}$, the Schrödinger equation can be written as:[52,53]

$$\mathcal{H}\psi_n = -\frac{\hbar^2}{2m} \frac{d^2\psi_n}{dx^2} = E_n\psi_n \quad (\text{II-1})$$

E_n gives the energy of the free electron in the n^{th} energy level. With the appropriate boundary conditions for the wavefunction, $E\psi_n(0) = 0$ and $\psi_n(L) = 0$, the solution of the Schrödinger equation in three dimensions is given as[52,53]

$$\psi_{\vec{k}}(\vec{r}) = e^{i\vec{k}\cdot\vec{r}} \quad (\text{II-2})$$

with the components of the wavevector being

$$k_x, k_y, k_z = 0, \pm \frac{2\pi}{L}, \pm \frac{4\pi}{L}, \dots = \pm \frac{2n\pi}{L} \text{ with } n = 0, \pm 1, \pm 2, \dots \quad (\text{II-3})$$

This leads to the energy levels for free electrons as a function of k , where m depicts the electron mass:[52,53]

$$E_{\vec{k}} = \frac{\hbar^2}{2m} (k_x^2 + k_y^2 + k_z^2) \quad (\text{II-4})$$

The stationary Schrödinger equation by taking into account the periodic potential of the bulk crystal with lattice constant a and potential V , with $V(x) = V(x+a)$, can be solved by:[52]

$$\varphi_{\vec{k}}(\vec{r}) = u_{\vec{k}}(\vec{r}) \cdot e^{i\vec{k}\cdot\vec{r}} \quad (\text{II-5})$$

The Eigenfunction of the wave equation of a periodic potential is the product of a plane wave $e^{i\vec{k}\cdot\vec{r}}$ and a periodic function $u_{\vec{k}}(\vec{r})$ with the same periodicity as the lattice: $u_{\vec{k}}(\vec{r}) = u_{\vec{k}}(\vec{r} + a)$. This is also known as Bloch's theorem.[52,53]

A physical picture describes a propagating wave through a periodic crystal in one dimension with lattice constant a that is disturbed by Bragg reflection. The Bragg condition is given as follows:[52,53]

$$(\vec{k} + \vec{G})^2 = k^2 \quad (\text{II-6})$$

In one dimension the condition becomes:[52,53]

$$k = \pm \frac{n\pi}{a}, \quad (\text{II-7})$$

with $n = 1, 2, 3, \dots$. The first reflection occurs at $k = \pm \frac{\pi}{a}$. Here also the first energy gap appears. The region in \vec{k} -space between $+\frac{\pi}{a}$ and $-\frac{\pi}{a}$ is called the first Brillouin zone (BZ). The branches of the parabola extending into the 2nd BZ may be folded back into the 1st BZ, this is called the reduced zone scheme. The Bragg reflection at $k = \pm \frac{\pi}{a}$, produces standing waves in the crystal. These are determined by the linear combination of a left and a right propagating wave.[52,53] This leads to a probability distribution of electron density either concentrated around the positive ion cores, which means that the average potential energy will be lower than for a free traveling wave, or between the ion cores, effectively increasing the potential energy. The energy difference between the standing waves is responsible for an energy gap. This effectively means that solutions to Schrödinger's equation are allowed at certain energies, while others are not.[52,53] The range of energies with no solution is referred to as the bandgap, which energetically separates the highest occupied energy level in the conduction band (CB) and the lowest unoccupied energy level in the valence band (VB) with the bandgap energy E_g . At $T = 0K$ the VB is fully occupied while the CB is completely empty. In semiconductors with a direct bandgap the band edges of VB and CB will be in the centre of the Brillouin zone. The threshold frequency for continuous absorption in a semiconductor determines the bandgap of the semiconductor with $E_g = \hbar\omega_p$. It can be well characterized with absorption spectroscopy. A photon with energy larger than the bandgap is absorbed and excites an electron from the VB to the CB leaving a hole behind in the VB .[52,53]

Effective mass

Electron and hole are quasiparticles with an ascribed effective mass $m_{e,h}^*$. The effective mass describes the influence of the crystal lattice on the electron/hole. It basically describes that an electron travelling through a periodic potential will be accelerated through an external electric or magnetic field as if it had an effective mass m_e^* . [52,53] The dispersion relation for small values of k can be assumed to be parabolic. From (II-4) we see that the coefficient of k^2 determines the curvature of $E_{\vec{k}}$ as

$$\frac{1}{m_e^*} = \frac{1}{\hbar^2} \frac{\partial^2 E_{\vec{k}}}{\partial k^2}, \quad (\text{II-8})$$

which determines the electron effective mass. At $k = 0$ it can be taken as constant. [52,53] Usually it is given as units of the vacuum electron mass m_e .

Exciton Bohr radius

After light absorption a bound electron-hole pair is formed due to Coulomb interaction, known as exciton. The Hamilton of an exciton can be written as:

$$\mathcal{H} = -\frac{\hbar^2}{2m_e^*} \nabla_e^2 - \frac{\hbar^2}{2m_h^*} \nabla_h^2 - \frac{e^2}{4\pi\epsilon\epsilon_0 |\vec{r}_e - \vec{r}_h|}. \quad (\text{II-9})$$

This is the same Hamilton operator as for the hydrogen atom, thus, similar as for hydrogen, a Bohr radius, the so called exciton Bohr radius may be determined as:

$$a_{ex} = \frac{4\pi\epsilon_0\epsilon\hbar^2}{\mu e^2}, \quad (\text{II-10})$$

with $\frac{1}{\mu} = \frac{1}{m_h^*} + \frac{1}{m_e^*}$. Together with an effectively smaller dielectric constant the exciton Bohr radii are in the range of a few nanometer. Thus, excitons may be delocalized over several thousand of atoms in the lattice. Absorption into an exciton occurs below the bandgap with a lower energy, equal to the binding energy of the exciton. [52]

Quantized energy levels in semiconductor nanocrystals

When the size of a semiconductor crystallite, such as a NC, comes close to the dimensions of the exciton Bohr radius of the material, the optical properties become size dependent. The carriers are confined by the boundaries of the material and the continuous electronic state densities of *VB* and *CB* become quantized/discrete, rather comparable to molecular electronic structures. This effect is known as the quantum size effect. [3] It results from the quantization of the bulk bands due to its finite dimensions, *i.e.*, the *VB* and *CB* will be quantized into

discrete energy hole and electron levels.[52] The resulting optical spectra are therefore a series of discrete electronic transitions rather than a broad continuous absorption. These discrete energy levels are sensitive to the level of confinement and with this they are strongly size dependent.[3] A spherical NC can to a good approximation be described by considering an electron in a spherical potential well with infinite potential barriers. This leads to a quantization of the electron and hole levels, as given by

$$E_{l,n}^{e,h} = \frac{\hbar^2 \phi_{l,n}^2}{2m_{e,h}^* R^2} \quad (\text{II-11})$$

with the angular momentum quantum number l , $m_{e,h}^*$ the electron and hole effective mass, R is the NC radius, $\phi_{l,n}$ is the n^{th} root of the spherical Bessel function.[3,52] From (II-11) we see a $1/R^2$ size dependence. The total energy difference is increasing with decreasing NCs size, resulting in a blue-shift of the absorption onset.[3]

II.2 Plasmon resonances in metallic nanoparticles

When metallic particles with diameters small with respect to the incoming wavelength interact with light, the oscillating field of the incoming electromagnetic wave excites the free carriers in the material to oscillations, which are coherent with the incoming wave.[44]

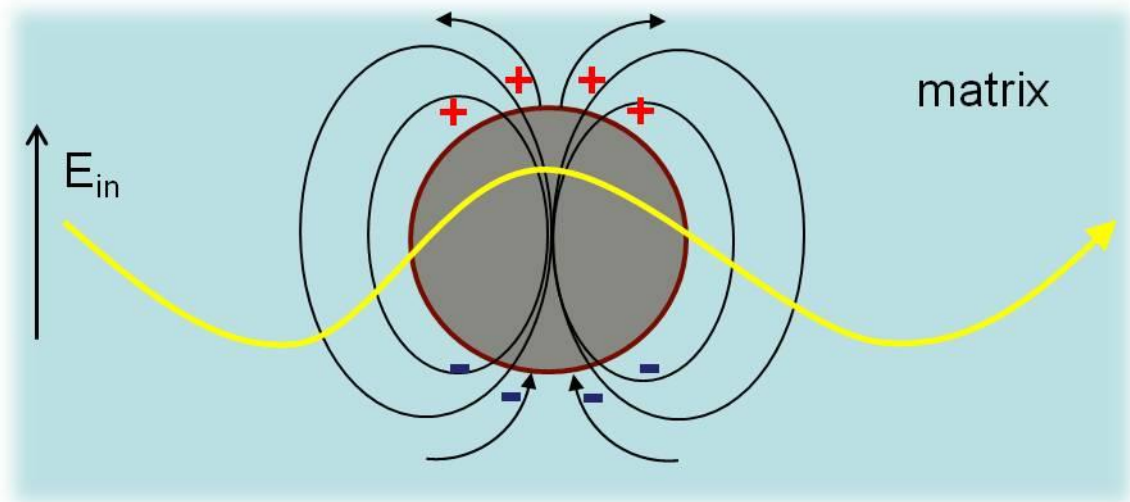


Figure II-2 Schematical depiction of the collective oscillations of the electrons in a metallic nanoparticle. When the electromagnetic wave penetrates the metal the electrons oscillate with the incoming electric field relative to the positive cores. This induced dipole itself creates an electromagnetic field that produces radiation.

The carriers are displaced with respect to the nuclei, which results in a restoring force. As a consequence this leads to net charges at the nanoparticles surface.[44] This is shown schematically in Figure II-2. At a certain frequency, which depends on the nanoparticle size, pronounced absorption is found. This resonance is commonly termed the localized surface plasmon resonance (LSPR).[44] It can be detected as enhanced intensity in the scattering spectrum of the particle. For metallic nanoparticles with sizes of tens to hundreds of nanometers such as gold and silver this plasmon resonance is found in the visible spectral range.[44]

The surface plasmon has two decay channels. One is the radiation of energy in form of an electromagnetic wave, analogous to a Hertz dipole. In the far field of the particle this is detected as scattered light.[44] On the other hand absorption takes place. Both processes are included in the extinction cross section (C_{ext}), *i.e.*, the sum of scattering cross section (C_{scat}) and absorption cross section (C_{abs}):

$$C_{ext} = C_{abs} + C_{sca}. \quad (\text{II-12})$$

Both depend on the polarizability α of the nanoparticles, which includes the dielectric function of the metal.[44]

Drude model

Drude ascribed the thermal as well as the electrical properties of metals to the motion of electrons based on the kinetic gas theory.[54] He was considering the electrons as quasi-free. That is, the electrons move nearly free between collisions without interactions among them or with the cores. After an elastic scattering event with lattice defects or phonons, the electrons move with a constant velocity.[54] This idea was further developed by Arnold Sommerfeld and is valid if the electronic and optical properties are determined by the conduction electrons alone.[54] Based on this, the response of metals to an external electric field is described by the Drude-Lorentz-Sommerfeld model (in the following termed Drude model), where only electrons of the conduction band contribute to an answer to an external electric field. The macroscopic effect is described by multiplying the effect of a single electron by the electron density.[44] For metals, the low energy values are well described by the Drude model. At higher energies there are contributions to the optical spectra ascribed to interband transitions. Those excitations of electrons from lower bands to the conduction band are neglected in this model.[44,54]

In the Drude approach, the incoming electromagnetic wave is considered to drive the free carriers to oscillations following the frequency of the incoming field. The free carriers are displaced with respect to the positive core, which leads to Coulomb attraction acting as a restoring force for the electrons.[44,54] The carriers oscillate with the driving frequency of the electromagnetic wave. In a classic picture it can be described by a harmonic oscillator with damping constant $\gamma = 1/\tau$. For bulk metals the damping constant is proportional to the Fermi velocity v_F of the metal and inversely proportional to the bulk mean free path l_∞ ($\gamma = v_F/l_\infty$).[44] When the object of observation becomes smaller than the bulk mean free path

($2R < l_\infty$, with R being the radius) a finite size effect comes into play.[24,44] This effect will be discussed later in this chapter. The response of a metal to an external field can be described by assuming the electric field of an electromagnetic wave travelling in x direction with a polarization along z direction. The magnetic field contribution can be neglected as the magnetic permeability is assumed to be unity in the visible spectral region.[44] With

$$\vec{E}_z = \vec{E}_0 e^{i\omega t} \quad (\text{II-13})$$

the equation of motion of an electron with mass m_e and charge e is given by:

$$m_e \frac{\partial^2 x}{\partial t^2} + m_e \gamma \frac{\partial x}{\partial t} + m_e \omega_0^2 x = -e \vec{E}_0 e^{i\omega t}. \quad (\text{II-14})$$

The solution of this equation is:[44]

$$x(t) = -\frac{e}{m_e} \frac{1}{(\omega_0^2 - \omega^2 - i\gamma\omega)} \vec{E}_0 e^{i\omega t}. \quad (\text{II-15})$$

The microscopic dipole moment p is connected to the polarization P with a carrier density n via:

$$P = n \cdot p = -n \cdot e \cdot x. \quad (\text{II-16})$$

And the frequency dependent polarization $P(\omega)$ is connected to the frequency dependent dielectric function by the following equation:[44]

$$\varepsilon(\omega) = 1 + \frac{P(\omega)}{\varepsilon_0 \cdot \vec{E}}. \quad (\text{II-17})$$

This finally leads to the complex dielectric function:

$$\varepsilon(\omega) = 1 + \frac{ne^2}{\varepsilon_0 m_e} \frac{1}{(\omega_0^2 - \omega^2 - i\gamma\omega)} = 1 - \frac{\omega_p^2}{(\omega_0^2 - \omega^2 - i\gamma\omega)}, \quad (\text{II-18})$$

Where

$$\omega_p^2 = \frac{ne^2}{\epsilon_0 m_e} \quad (\text{II-19})$$

is the bulk plasma frequency ω_p , with ϵ_0 the vacuum permittivity.[44] To account for interactions of the electrons with the lattice the electron effective mass m^* is used instead of m_e . Finally the frequency dependent dielectric function can be written as:[54]

$$\epsilon(\omega) = \epsilon'(\omega) + i\epsilon''(\omega) = 1 + \omega_p^2 \frac{(\omega_0^2 - \omega^2)}{(\omega_0^2 - \omega^2)^2 + \gamma^2 \omega^2} + i\omega_p^2 \frac{\gamma \omega}{(\omega_0^2 - \omega^2)^2 + \gamma^2 \omega^2} \quad (\text{II-20})$$

The damping of the collective oscillations is due to scattering of the electrons at electrons, phonons, lattice defects or impurities. In the free electron theory the damping constant is given by the inverse of the scattering time of the electron:[44]

$$\gamma = \tau^{-1} = \tau_{e-e}^{-1} + \tau_{e-ph}^{-1} + \tau_{e-d}^{-1} \quad (\text{II-21})$$

As already mentioned, the Drude theory neglects electrons in the valence band and thereby inter- and intraband transitions, which have a significant contribution to the dielectric response of the material at higher photon energies. However, it well describes the region where electrons only contribute to the optical spectra.

In Figure II-2 the modeled C_{ext} of a 40 nm gold sphere is given. The calculated spectra represent a pronounced resonance corresponding to the LSPR of the 40 nm diameter gold sphere at ~530 nm. The spectra were calculated using on the one hand the empirical bulk dielectric function of gold [55] (dashed line) as input for the simulation, and on the other hand the Drude dielectric function (solid line). While both represent the LSPR, the region of interband transitions (below ~450 nm) are not represented in the Drude model. Nevertheless, the Drude model delivers good results close to the plasmon resonance, if the contribution of core transitions does not affect the spectral signature in this region.

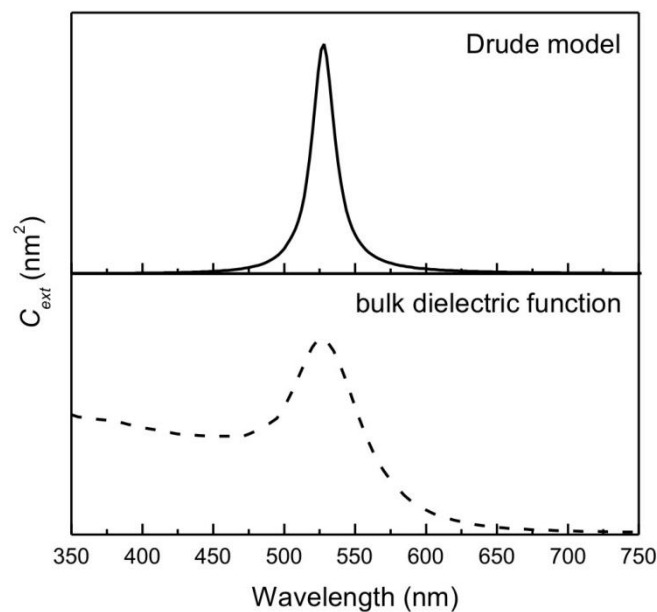


Figure II-3 Modeled extinction cross section for a gold sphere of 40 nm diameter in water using the Drude dielectric function (solid line) and the bulk dielectric function [55] (dashed line) as input data. Both show a resonance peak at ~530 nm. For the Drude model only the region of free carrier absorption is represented, while the region of interband transitions (below ~450 nm) is neglected. For the modeling of the sphere, the BEMAX program based on the boundary element method has been used.[24,56,57]

Mie theory

The analytical solution of the response of a small metallic sphere to electromagnetic radiation within the frame of electrodynamics was first described by Gustave Mie. In 1908 [58] he solved Maxwell's equations by choosing appropriate boundary conditions and used multipole expansions of the electric and magnetic field with the input parameters particle size, and optical material functions of the particle and the surrounding medium.[44] In the following

the general solution of this method will be described for particles much smaller than the incoming light wave, *i.e.*, $R \ll \lambda$ (quasi-static regime). For spherical particles the C_{ext} is given as:[44]

$$C_{ext} = \frac{2\pi}{k^2} \sum (2n + 1) Re(a_L + b_L), \quad (\text{II-22})$$

with $k = \frac{2\pi}{\lambda}$ and a_L and b_L being the scattering coefficients. These are functions of the size parameter α of the particle:[44]

$$a_L = \frac{m\psi_L(m\alpha)\psi_L'(\alpha) - \psi_L'(m\alpha)\psi_L(\alpha)}{m\psi_L(m\alpha)\eta_L'(\alpha) - \psi_L'(m\alpha)\eta_L(\alpha)}, \quad (\text{II-23})$$

$$b_L = \frac{\psi_L(m\alpha)\psi_L'(\alpha) - m\psi_L'(m\alpha)\psi_L(\alpha)}{\psi_L(m\alpha)\eta_L'(\alpha) - m\psi_L'(m\alpha)\eta_L(\alpha)}, \quad (\text{II-24})$$

where $m = \frac{n}{n_m}$, and n is the complex index of refraction of the particle and n_m is the real index of refraction of the surrounding medium. With n , the dielectric function of the bulk material $\varepsilon(\omega) = \varepsilon'(\omega) + i\varepsilon''(\omega)$ is included. α is defined as:

$$\alpha = \frac{2\pi R}{\lambda} \quad (\text{II-25})$$

ψ_L and η_L are related to Ricatti-Bessel cylindrical functions, where the prime indicates the first derivative with respect to the argument.[44] L is the summation index. It gives the order of spherical multipole excitations in the particle. Thus, $L = 1$ stands for dipolar fields, $L = 2$ to quadrupolar fields and so on.[44] For small particles only dipolar contributions, *i.e.*, with $L = 1$ play a dominant role. Thus, in the dipolar regime C_{ext} for a spherical particle is simplified to:[24]

$$C_{ext} = \frac{18\pi V \varepsilon_m^{3/2}}{\lambda} \frac{\varepsilon''(\omega)}{(\varepsilon'(\omega) + 2\varepsilon_m)^2 + \varepsilon''^2(\omega)}. \quad (\text{II-26})$$

ε_m is the surrounding dielectric constant, $\varepsilon(\omega)$ is the dielectric function of the particle. V is the particle volume. C_{ext} has a resonance where $(\varepsilon'(\omega) + 2\varepsilon_m)^2 + \varepsilon''^2(\omega)$ is minimal. When $\varepsilon''(\omega)$ is small this condition gives:[44]

$$\varepsilon'(\omega) = -2\varepsilon_m. \quad (\text{II-27})$$

Influence of solvent refractive index on the LSPR

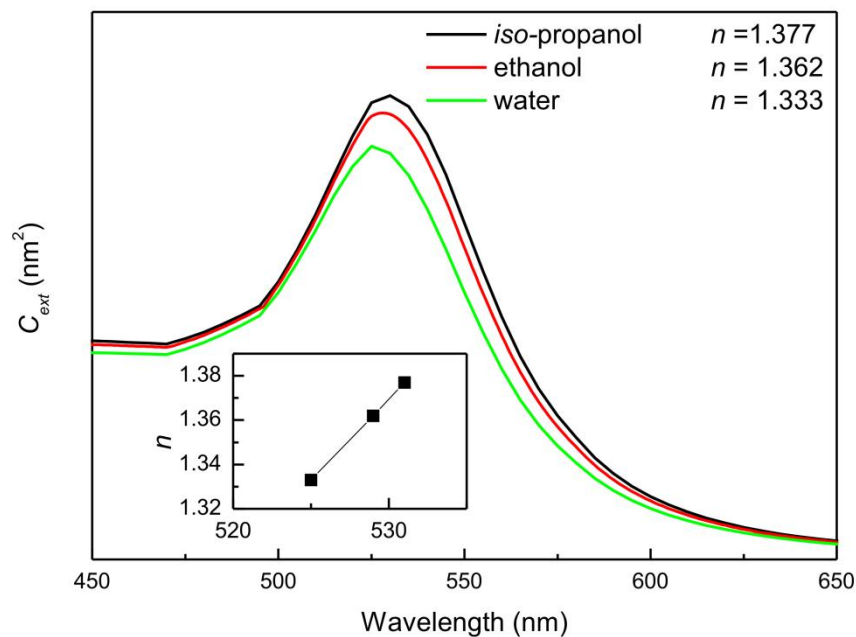


Figure II-4 BEMAX modeling of a 40 nm gold sphere in different environments, water, ethanol, and iso-propanol, using the empirical bulk dielectric function of gold [55]. The refractive indices are different for the three solvents and depicted in the upper right corner. Inset: LSPR peak position vs. refractive index. For the modeling, the BEMAX program based on the boundary element method has been used.[24,56,57]

Equation (II-27) shows the influence of the surrounding medium refractive index n ($n^2 = \varepsilon_m$) on the dielectric function of the material and with this, the dependence of the plasmon resonance on the refractive index n of the surrounding medium.[25] An increased medium dielectric constant results in a decrease of the Coulombic restoring force of the electron cloud, which in turn leads to a decrease of the plasmon frequency.[25] Figure II-4 shows the calculated extinction cross sections for a 40 nm gold sphere in three different solvents, such as *iso*-propanol, ethanol, and water, using the empirical bulk dielectric function of gold as input data.[55] A red-shift of the LSPR with increasing refractive index of the solvent is observed.

This shift is summarized in the inset of Figure II-4, where the maximum peak position is plotted versus the refractive index of the respective solvent. The refractive index sensitivity of the LSPR can be exploited in biosensing applications.[59,60]

Influence of nanoparticle size on the LSPR

With increasing size a higher number of carriers are present in the nanoparticle contributing to the plasmonic properties. Thus, the extinction of the particle increases with its volume, as seen from Mie extinction cross section (Formula (II-26)) in the dipolar limit.[44]

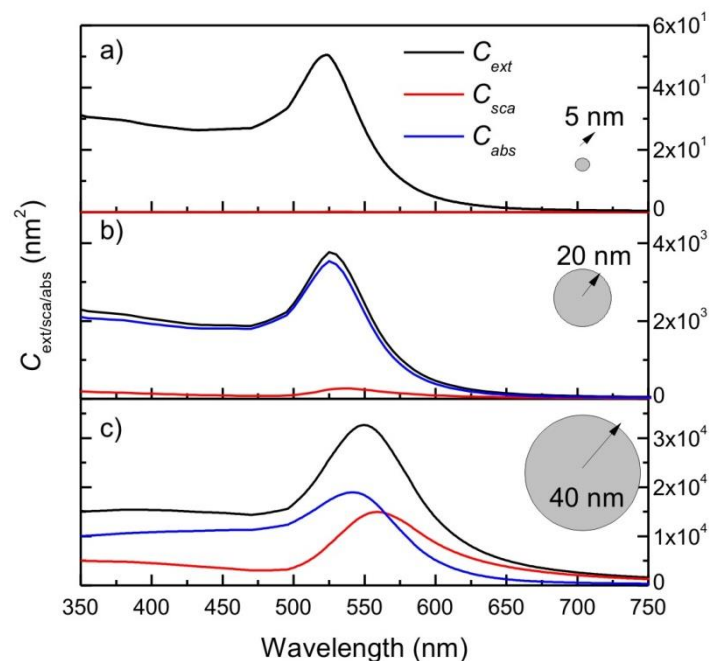


Figure II-5 Calculated extinction spectra for gold nanospheres of different sizes, a) 5 nm radius, b) 20 nm radius, and c) 40 nm radius. The extinction cross section is given in black, scattering and absorption cross sections are given in red and blue, respectively. For bigger nanoparticles, the extinction is higher and the contribution of scattering to the extinction spectrum gains more importance. For the modeling, the BEMAX program based on the boundary element method has been used.[24,56,57]

Figure II-5 shows the calculated extinction spectra of gold nanospheres of varying sizes of 5 nm, 20 nm, and 40 nm radius (Figure II-5a, b, and c, respectively). The overall extinction increases with nanoparticle size. Further, an increased scattering contribution for larger particles is observed, while for the 5 nm radius particle only absorption contributes to the extinction spectrum. When the particle size becomes close to the wavelength of the incoming light, phase retardation effects lead to a red-shift of the plasmon resonance.[24] The

nanoparticles no longer are homogeneously polarized by the electric field of light. This results in higher order oscillation modes that contribute to the extinction spectrum and result in additional peaks (not shown here), as well as broadening of the spectra due to a loss in phase coherence.

For particles much smaller than the incoming light wave, *i.e.*, $R \ll \lambda$ (quasi-static regime), the extinction cross section in Mie theory becomes independent of the particle volume.[44] This is in contrast to observations found experimentally for small metallic nanoparticles.[61,62] To account for size effects within the Mie theory it has been proposed that electron scattering at the nanoparticle surface plays an enhanced role in such small particles, as the mean free path of the conduction electron is larger than the particle radius.[62,63] Thus, the carriers scatter with the surface elastically and by this lose coherence more quickly. As a consequence the plasmon resonance will be broadened and red-shifted with decreasing particle size.[62] It has been shown that the plasmon resonance bandwidth is inversely proportional to the particle radius.[62,63] In the free electron Drude model γ is introduced as a phenomenological damping constant. For the case of a perfectly free electron gas it is equal to the plasmon absorption bandwidth Γ , provided that $\gamma \ll \omega$. [62] As already described above, the damping of electrons (γ_0) is due to collisions of the coherent electron oscillations with electrons, phonons or lattice defects. To account for surface scattering in nanoparticles that are smaller than the mean free path of the electrons an additional term has to be included. Then $\gamma(R)$ accounts for the size dependence as: [62]

$$\gamma(R) = \gamma_0 + \frac{v_F}{R} \quad (\text{II-28})$$

where v_F is the Fermi velocity of the electrons. As this effect is a size effect dependent on the dielectric function itself it is considered as an intrinsic size effect, with respect to the extrinsic effects of particles with larger radius R . [62,63]

Influence of nanoparticle shape on the LSPR: ellipsoids

Due to the high symmetry of a spherical particle, the excitation of the LSPR is independent of the polarization of excitation. In rods however, light polarization plays a significant role as two main directions can be identified: along the main axis of the rod or perpendicular to it (sketch in Figure II-6b). Indeed, for gold nanorods, the extinction spectrum splits into two bands, corresponding to the oscillations along (longitudinal or L-band) and perpendicular to the long axis (transverse or T-band).[62]

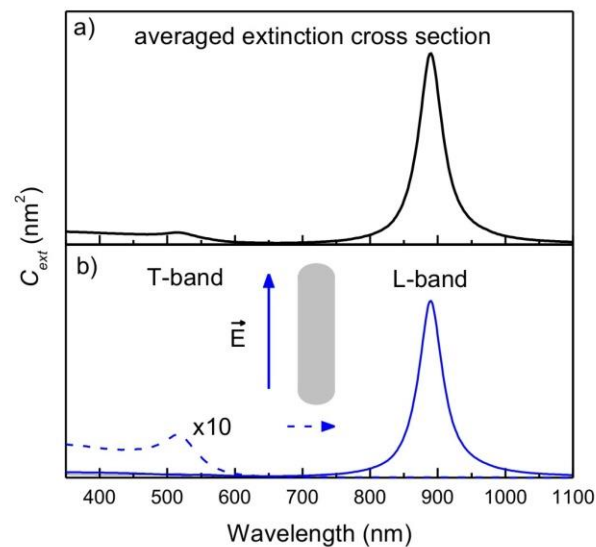


Figure II-6 BEMAX calculated extinction cross sections for a gold nanorod of 5 nm width and 21 nm total length. Two distinct bands are observed, the higher energy band at ~510 nm is called the transverse or T-band and attributed to the oscillations perpendicular to the long axis of the nanorod. The low energy band at ~890 nm is more intense and arises due to the plasmon oscillations along the nanorod axis (longitudinal or L-band). a) Calculated extinction spectrum averaged over all possible excitation directions. This is coming close to an ensemble measurement of nanorods in solution. b) Separate excitation of the nanorod along the nanorods axis (L-band, blue solid line) and perpendicular to it (T-band, blue dashed line).

Figure II-6 depicts the calculated extinction cross section of a gold nanorod of 5 nm width and 21 nm length. The aspect ratio (AR) has been set to 4.1. Figure II-6a shows the averaged extinction spectrum. A typical measurement of unordered nanoparticles in solution is an average over all possible excitation directions, thus, the averaged extinction spectrum is a close representation of an ensemble measurement in solution. Figure II-6b shows the extinction spectrum of gold nanorods separately excited along (longitudinal or L-band) and perpendicular to the long axis (transverse or T-band) of the nanorod. The longitudinal plasmon mode is strongly red-shifted with respect to the transverse mode. The L-band depends on the AR. It increases and red-shifts with increasing AR, while the short axis plasmon resonance (T-band) is only weakly dependent on the particle's AR.[64]

For ellipsoid particles the Mie theory might be extended according to R. Gans [65], calculated in the quasi-static regime for ellipsoid particles:

$$C_{ext} = \frac{2\pi V \varepsilon_m^{3/2}}{3\lambda} \sum_j \frac{(1/P_j^2) \varepsilon''(\omega)}{(\varepsilon'(\omega) + \frac{1-P_j}{P_j} \varepsilon_m)^2 + \varepsilon''^2(\omega)}. \quad (\text{II-29})$$

P_j are the depolarization factors for the three axes $j = A, B,$ and C of the particle with $A > B = C$. [62]

$$P_A = \frac{1-e^2}{e^2} \left[\frac{1}{2e} \ln \left(\frac{1+e}{1-e} \right) - 1 \right], \quad (\text{II-30})$$

$$P_B = P_C = \frac{1-P_A}{2} \quad (\text{II-31})$$

with the aspect ratio AR being included in the formula as:

$$e = \sqrt{1 - \left(\frac{B}{A}\right)^2} = \sqrt{1 - \frac{1}{AR^2}}. \quad (\text{II-32})$$

Within this formulation it becomes clear that the different axis of the ellipsoid contribute differently to the nanoparticle spectrum. Two distinct bands arise from excitation along the long axis of the ellipsoid (A) and perpendicular to it (B and C). [64]

Other shapes: Discrete-dipole approximation

The Mie theory regards solely spherical particles. [58] Later this theory was extended for ellipsoidal particles. [65] Even more sophisticated shapes do not allow to solve Maxwell's equations analytically. [66] For nanoparticles of arbitrary geometry the discrete dipole approximation (DDA) is a powerful technique to calculate scattering (C_{sca}) and absorption cross sections (C_{abs}). The basic idea of the DDA is the approximation of a continuous particle by a finite number of dipoles organized in a cubic lattice. [67] The inspiration goes back to Lorentz who in 1909 showed that the dielectric properties of metals are related to the

polarizabilities α of its individual atoms. The Clausius-Mossotti (or Lorentz-Lorenz) relation, when assuming the atoms are located on a cubic lattice, accounts for the dipole moment that each atom carries when interacting with an external electric field \vec{E}_0 . [52,67] Then, the local electric field \vec{E}_{loc} at an atom can be expressed as the superposition of the external surrounding field \vec{E}_0 and the fields of the surrounding induced dipoles \vec{E}_{ind} . The Clausius-Mossotti relation by taking into account the embedding medium dielectric constant ϵ_m is given as: [44,52]

$$\alpha = \frac{3\epsilon_0}{n} \cdot \frac{(\epsilon - \epsilon_m)}{(\epsilon + 2\epsilon_m)}. \quad (\text{II-33})$$

This equation relates the microscopic polarizability α to the macroscopic dielectric function ϵ of the material. This solution in the quasi-static regime is a good estimate for sufficiently small particles and gives reasonable results in small size ranges. However, it needs to be extended considerably for larger particles and particles of arbitrary shapes. [24]

The DDA is a numerical method which may be used to describe the extinction spectra of metal nanoparticles of any given shape. [24] A continuous material is approximated as discrete elements that are polarized by the superposition of the external electric field and the polarization of the surrounding elements. [24,67] The dipole moments \vec{p}_j of the element j centered in r_j with dipolar polarizability α_j are acquired in response to a local electric field $\vec{E}_j(r_j)$: [67]

$$\vec{p}_j = \alpha_j \cdot \vec{E}_j(r_j) \quad (\text{II-34})$$

The local field is composed of the incident field ($\vec{E}_{inc,j} = \vec{E}_0 \exp(i\vec{k} \cdot \vec{r}_j - i\omega t)$) plus each contribution of the other N-1 dipoles:

$$\vec{E}_j(r_j) = \vec{E}_{inc,j} + \sum_{k \neq j} \mathbf{A}_{jk} \vec{p}_k \quad (\text{II-35})$$

where $\mathbf{A}_{jk} \vec{p}_k$ is the electric field at r_j that is due to the dipole \vec{p}_k at location r_k . [67] The metal dielectric constant and that of the surrounding medium are contained in the polarizabilities α_j .

Finally the extinction cross section is given as follows:

$$C_{ext} = \frac{4\pi k}{|E_0|^2} \sum_{k=1}^N \text{Im} \left(\vec{E}_{inc,j}^* \cdot \vec{p}_j \right). \quad (\text{II-36})$$

From this the absorption and scattering cross sections can be calculated.[67] Calculations with the DDA are an intensive numerical effort because of the large number of coupling terms.[24] It has advantages when addressing very complex geometries such as tetrapods, as will be shown later in this work.

Electromagnetic field enhancement and interparticle coupling

So far the discussion has focused on the far-field properties of metallic materials. However, for certain properties taking place in the close vicinity of the nanoparticle, it is the electromagnetic field at or near the particle's surface that counts.[66] The enhanced electric field created in close vicinity of the particle's surface due to the plasmon oscillation, decays exponentially with distance to the surface.[68] In Figure II-7 the near-field enhancement (NFE) maps for the same gold nanorod of 5 nm width and 21 nm total length, as given in Figure II-6, excited with the polarization perpendicular (left image) and along (right image) the long axis of the nanorod at the respective extinction maximum as determined from Figure II-6 are given. The enhancement factors for the T-band and L-band are ~4 and ~90, respectively. Such high enhancement factors may be exploited for applications such as surface enhanced Raman spectroscopy (SERS).[69]

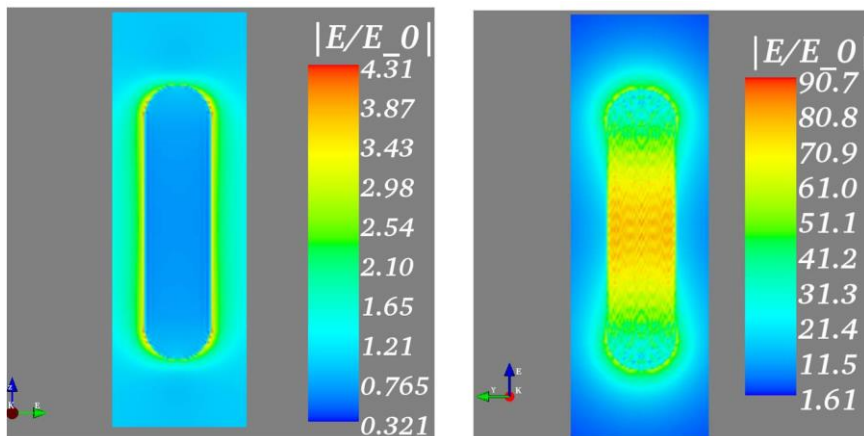


Figure II-7 NFE maps for the same gold nanorod of 5 nm width and 21 nm total length, as given in Figure II-6, upon excitation of the T-band (left image) and L-band (right image).

Interparticle plasmon coupling is a result of the strong interaction between plasmonic particles, when close enough together so that the near-fields of the particles overlap. The coupling through the electrostatic field of the particles, depending on the orientation of the polarization of the particle with respect to each other, leads to red- or blue-shifted spectra of the coupling particles with respect to the isolated ones.[70,71] The coupling-induced shifts can be controlled with interparticle distance and number of particles involved in the coupling.[71] Interparticle plasmon coupling finds application in biosensing or SERS.[72]

Plasmon dynamics in metallic nanoparticles

The plasmon dynamics can be probed by using transient absorption spectroscopy with an intense laser pulse exposed to the sample, followed by a weak probe pulse monitoring the temporal evolution of the system. Differential spectra show a non-linearity in the region of the surface plasmon resonance caused by an optically induced broadening of the surface plasmon due to an increase in electron and lattice temperature.[5,13] The bandwidth of the plasmon resonance is a measure of the dephasing of the coherent oscillations of the electron gas. Increased electron or lattice temperature leads to changes in its collision frequency and with this to a broadening of the plasmon resonance.[73]

After the initial excitation with an intense laser pulse energetic electrons are created that thermalize via electron-electron scattering. The new Fermi distribution results in a carrier gas with higher temperature than the lattice.[5,13] This is observed as an initial rise in the kinetics.[5,13] Thereafter, two distinct temporal dynamics, on the time scale of picoseconds for the short-time dynamics and hundreds of picoseconds for the long-time dynamics are detected. Those temporal evolutions are assigned to elevated temperatures of the carrier gas (initial decay) and the lattice (second decay) induced by the pump-pulse.[73,74] While the first decay is ascribed to the temperature equilibration of the electron gas due to electron-phonon scattering evoking an elevated lattice temperature, the second decay is related to the cooling of lattice via phonon-phonon scattering with the surrounding medium.[73,74] The difference between the time constants of electron and lattice heating is understood in the difference between electronic and lattice heat capacity which differs in about two orders of magnitude.[13]

II.3 Vacancy-doped semiconductor nanocrystals: copper chalcogenides

Localized surface plasmon resonances (LSPRs) have been highly investigated in recent years focusing on noble metal nanostructures such as gold, silver or copper, with charge carrier densities in the range of 10^{22} – 10^{23} cm^{-3} . In those structures the resonance frequency of the plasmon resonance is determined at the stage of synthesis, with strong influence of their size or shape on the plasmon frequency (as discussed in the previous chapter).[24,66,71] Nevertheless, with a fixed carrier density the tunability of the plasmon resonance is very limited. Unlike in metals, the LSPRs in vacancy doped, or degenerately doped materials can be tailored by tuning their carrier density through the control over their doping level.[20,27-35] This is connected to the stoichiometry of the crystal structure that in turn represents the vacancy density. The formation of vacancies within the crystal structure causes a severely increased charge carrier density up to about 10^{21} cm^{-3} . This initiates a character more associated with a metal than a semiconductor.[26,29,31,32,34] To be more precise, the stoichiometric compound, not possessing vacancies, exhibits purely semiconducting properties, while the non-stoichiometric or deficient counterpart is dominated by metallic character. A typical degenerate semiconductor is indium tin oxide (ITO). Its large bandgap of 4 eV makes it a transparent conducting candidate that is widely used in organic electronics. ITO is a heavily-doped n-type semiconductor. An increase in carrier density and with this in conductivity comes along with oxygen vacancies in the structure.[75-77] Those create extra electrons that lead to an increase in the carrier density. Charge carrier densities are in the range of $\sim 10^{20}$ – 10^{21} cm^{-3} , depending on the number of oxygen vacancies in the structure.[77] In spectroscopy, pronounced absorption in the NIR spectral range is attributed to free carrier absorption.[77,78] Another prominent vacancy doped semiconductor is tungsten oxide ($WO_{3-\delta}$), with a variety of discrete phases and precise stoichiometries, such as WO_3 , $WO_{2.72}$, $WO_{2.8}$, or $WO_{2.9}$. [31] With an oxygen deficiency of $\delta = 0.1$, the transition from insulator to metal takes place, indicating an increased charge carrier density.[79] The carrier density in this material is determined to be $\sim 10^{21}$ cm^{-3} and is equal to twice the number of oxygen vacancies.[79] Similar characteristics are found in the family of copper chalcogenides, namely copper sulfide ($Cu_{2-x}S$), copper selenide ($Cu_{2-x}Se$), and copper telluride ($Cu_{2-x}Te$), where copper vacancies generate a highly increased carrier density. This material system will be introduced in the following chapters.

II.3.1 The role of stoichiometry, crystal structure and copper vacancies

Copper chalcogenides, namely copper sulfide (Cu_{2-x}S), copper selenide (Cu_{2-x}Se), and copper telluride (Cu_{2-x}Te), show degenerate doping arising from copper vacancies in the structure. ($2-x$) in the chemical formula depicts the stoichiometry factor which varies between 0 and 2.[36] The variation of x leads to different stoichiometries ascribed to precise crystal structures. For Cu_{2-x}S these structures include for example the Cu-rich chalcocite Cu_2S or the copper-poor covellite CuS with intermediate phases such as djurleite $\text{Cu}_{1.97}\text{S}$ or digenite $\text{Cu}_{1.8}\text{S}$. [36] These phases are of complex crystal structures and sometimes difficult to distinguish. It took several years until it was accepted that beside chalcocite Cu_2S a second phase of comparable crystal structure, djurleite ($\text{Cu}_{1.97}\text{S}$), exists. Due to large unit cells their solution required a considerable effort.[80,81] In their selenium and tellurium counterpart similar versatile phases are observed.[82] The copper deficient stoichiometries are formed due to thermodynamic instabilities of the stoichiometric compound to ambient conditions.[32,34,82,83] With a rather high free energy, with respect to the copper deficient structures, it tends to relax into the thermodynamically favored structure, that is, the copper deficient structure.[84] Indeed, it has been shown that structures of lower deficiency may be obtained from the stoichiometric compounds ($x = 0$) under thermal treatment in air or anodic oxidation.[85,86] The suggested process is explained by surface oxidation of Cu^+ to Cu^{2+} with oxygen binding to the surface, forming a copper oxide layer.[82-84,86,87] A detailed study on Cu_{2-x}Se NCs revealed that the exposure to ambient conditions evokes a solid state conversion from the stoichiometric ($x = 0$) crystal structure to the copper-deficient ($x > 0$) phase.[82] Accurately, in Cu_2Se ($x = 0$) only Cu^+ sites as well as Se^{2-} binding sites in a consistent bonding environment with a Cu:Se ratio of 2:1 has been shown via X-ray photoelectron spectroscopy (XPS) studies. Evaluation of the solid state conversion to Cu_{2-x}Se ($x > 0$) revealed the appearance of mixed valences of Cu^+ and Cu^{2+} upon air exposure.[82] The Se sites were determined to show multiple oxidation states ranging from the selenide to the oxide species, converted from the anion to the fully oxidized cation. Further, an increase in surface atomic ratio of Cu to Se occurred upon oxidation. This suggests that solid-state diffusion of cationic Cu from the particle core to the surface occurs, leading to an accumulation of Cu at the surface likely forming copper oxides at the NCs surface.[82] The given results suggest that the oxidation of Cu surface sites to Cu^{2+} establishes a chemical potential gradient within the particle leading to a solid-state diffusion of cationic Cu from the

particle core to the surface, making the particle core Cu deficient.[82] This process is very likely, as in Cu_{2-x}Se the copper ions are mobile and 2% of the conductivity results from ionic conductivity.[88]

II.3.2 Physical properties of vacancy doped copper chalcogenides

In agreement with degenerately doped material based on oxygen, conductivity has been found to increase when moving from the stoichiometric to the deficient structure, *i.e.*, from Cu_2S , with $x = 0$, towards CuS , with $x = 2$. [85] The selenide analogon to copper sulfide shows similar behavior. Stoichiometric Cu_2Se NCs with $x = 0$ fabricated into electronic devices demonstrate purely semiconducting behavior.[82] With exposure to oxygen a 3000-fold increase in conductivity is observed and a change to ohmic behavior with p-type conductivity. Thus, the increase in conductivity is correlated to the change in stoichiometry, *i.e.*, the copper deficiency.[82] P-type conductivity in copper chalcogenides might occur because the extraction of copper ions, *i.e.*, the creation of copper vacancies, is accompanied by the removal of electrons from the top of the valence band leading to excess holes.[40] In optical measurements, the absorption in the NIR is increasing with x (from $x = 0$ to $x = 2$) and is supposed to arise from free carriers in the structure.[85] The higher the extent of oxidation, *i.e.*, the larger x , the stronger the absorption detected from free carriers. Indeed, it has been shown that the absorption by free carriers is to a good approximation proportional to the copper deficiency and hence to the carrier concentration.[40] Copper chalcogenides are indirect bandgap semiconductors with bandgaps in the region of ~ 1.2 eV depending on the chalcogenide.[40-42] A particularly compelling characteristic of copper chalcogenides, especially Cu_{2-x}S , is the increase of the bandgap with copper deficiency x , ranging from 1.2 eV to 2 eV. The shift of the bandgap with the increasing number of copper vacancies has been explained by the Moss–Burstein effect of heavily doped semiconductors.[89] The Moss-Burstein effect is observed as a shift of the bandgap with increasing doping concentration.[90,91] Upon the increase of copper vacancies, electrons are removed from the top of the valence band, reaching a degenerate level of doping, the Fermi level moves below the valence band edge. Thus, higher photon energies are required to excite electrons from the Fermi level to the conduction band edge. With this, an apparently higher bandgap is observed.[90,91]

II.4 Copper chalcogenide nanocrystals: State of research and open questions

In recent years copper sulfide (Cu_{2-x}S) NCs have attracted an increasing attention due to their prospective application in energy related fields. Specifically the exceptionally low bandgap of ~ 1.2 eV has been highlighted, suggesting Cu_{2-x}S NCs as absorber material in photovoltaic devices. Further, the non-toxicity and earth abundance of the elements has been stressed with respect to large scale application.[92,93] Indeed, in 2008 Wu *et al.*[92] reported on a solution-processed $\text{Cu}_2\text{S}/\text{CdS}$ NC solar cell with 1.6 % power conversion efficiency.[92] Their incorporation into solar related devices clearly demands an exact understanding of their optical and structural properties. The characterization as provided within this work revealed a stoichiometric composition of the Cu_2S NCs with the absorption dominated by a semiconducting character, *i.e.*, a weak absorption onset at ~ 900 nm increasing to the blue and no absorption further in the NIR.[92] In sharp contrast to this are the findings published shortly after by Zhang *et al.*,[36] broadening the discussion to the various deficient counterparts of Cu_{2-x}S NCs ($x = 1, 0.2, 0.03$). In particular, they showed that NIR resonances dominate the absorption spectra of Cu_{2-x}S NCs with $x > 0$, which further blue-shift with the increasing value of x . [36] The high carrier density, related to the copper vacancies in the copper deficient counterparts, was suggested to be responsible for this observation and the discussion of LSPRs in this type of material was initiated.[36] Controversial interpretations of the optical spectra of copper chalcogenide NCs dominate earlier reports.[94-96] The NIR resonances of CuS NCs for example have been assigned to interband absorption from an intermediate energy state within the bandgap, occurring due to a surface oxide layer [97] or deep trap states.[98] In Cu_{2-x}Se NCs the NIR band has been interpreted as an indirect interband transition.[99] Furthermore, the mixed valences in the copper deficient copper chalcogenides might account for intervalence charge transfer from Cu(I) to Cu(II) , as observed in many Cu -complexes with mixed Cu valences, leading to optical transitions that might be located in the NIR.[100-102]

These considerations highlight the need for a precise evaluation of the optical characteristics of this type of material, in particular if plasmonic as such. An exact synthetical control over shape and phase, so far limited to Cu_{2-x}S [36,37,45,92,98,103-107] and to a minor extent Cu_{2-x}Se [82,99] NCs is a prerequisite for such an investigation. Considering the characteristics of bulk copper chalcogenides, as discussed in the previous chapters, the stoichiometric phase

is expected to exhibit purely semiconducting properties. At the nanoscale this would result in excitonic properties, while the deficient phase with an increased carrier density is expected to exhibit LSPRs in the NIR, as observed in Ref. [36]. So far this interpretation is missing a specific experimental evaluation. Its plasmonic nature, however, can be identified by probing typical plasmonic characteristics such as refractive index sensitivity, size dependence, plasmon coupling or dynamics of the NIR resonance. Those characteristics would unambiguously identify a plasmonic nature of the NIR resonances in copper chalcogenide NCs. A noticeable peculiarity of such a finding lies in the structural characteristics of copper chalcogenides, which are ionic semiconductor crystals, as such. The synthesis protocols for this material class, to date, provide a versatility of anisotropic shapes with exceptionally monodisperse size distributions, highlighting this material system over common plasmonic nanoparticles. Further, the combination of semiconducting properties, with relatively low bandgaps in the region of ~ 1.2 eV [40-42] and LSPRs in one material is a key feature characterizing this material. As the lowest interband transition is close in energy to the plasmon resonance, it is of interest to investigate a possible influence of the latter on the excitonic transitions. In copper chalcogenides the increased carrier density is a result of the copper vacancies in the structure. Those are chemically accessible via oxidation, as discussed above. This specific tailoring of the copper vacancies, and with this the carrier density, is a unique property of vacancy doped copper chalcogenides. This remarkable feature might be beneficially introduced also at the nanoscale. To be more precise, a chemical control over the copper vacancy density could allow for a tailoring of the carrier density in the NCs. This would result in the tunability of the NIR plasmon resonance in copper chalcogenide NCs over a wide range of frequencies, further highlighting this new type of plasmonic material over conventional ones. However, for a complete understanding of the plasmonic nature of the NIR resonances in copper chalcogenide NCs a theoretical description of its plasmonic properties is required. Is a theoretical treatment of the plasmon resonances in this type of material possible through the implementation of similar models as used to describe the plasmonic properties of noble metal nanoparticles or is a deviation from the free carrier-like behavior expected? In this work, the open questions as summarized above are addressed. The results presented within this work are based on the synthesis of copper chalcogenide NCs with precise sizes and shapes and exact crystallographic structures. A unique combination of optical and structural characterization supported by theoretical modeling presents an elaborate evaluation of the structure dependent optical properties of copper chalcogenide NCs.

III. Experimental methods and sample preparation

III.1 Characterization of nanocrystals: structure, shape and composition

III.1.1 Structural characterization with X-ray diffraction

The NCs synthesized within this work are in size ranges of a few nanometers only. However, similar to bulk semiconductors, these nanoscale crystals exhibit an exact crystallographic structure with a defined unit cell and certain lattice parameters. A technique to visualize the crystal structure is X-ray diffraction analysis (XRD). It is based on the diffraction of X-rays from the periodic lattice of a crystal whose interatomic spacing lies in the region of the wavelength of the X-ray beams.[52] The diffraction of X-rays at periodic crystals has been discovered by Max von Laue who was simultaneously proving the wave-like nature of X-rays. In 1914 he was awarded the Noble Prize in Physics for this discovery.[108] William Henry Bragg and William Lawrence Bragg, proposed an equation for which they were awarded the Nobel Prize in Physics in 1915 when they connected the wavelength of the X-rays to the distance between the planes d and the angle θ at which the X-rays are reflected.[109] At certain angles of incidence θ , such that the Bragg equation is satisfied, constructive interference will occur:[52]

$$n \cdot \lambda = 2 \cdot d \cdot \sin\theta \quad (\text{III-1})$$

Only where $2d\sin\theta$ is an integer multiple n of the incoming light wavelength λ , constructive interference takes place.[53] This is illustrated in Figure III-1.

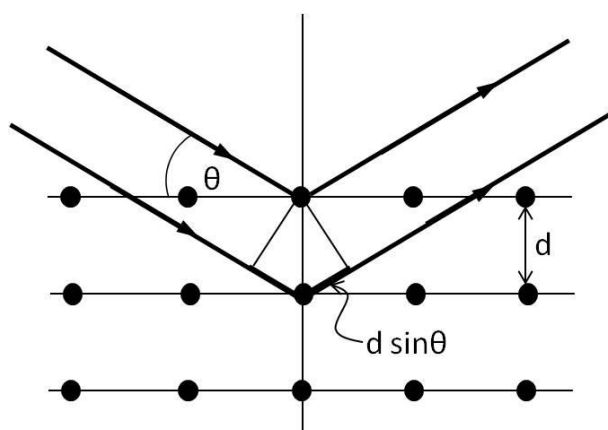


Figure III-1 Illustration of Bragg diffraction at a 2D crystal lattice. Constructive interference takes place where $2d\sin\theta$ is an integer multiple of the incoming light wavelength.

These discoveries had a huge impact in the field of crystallography, as now it was possible to determine the position of atoms in crystals, which is feasible through single crystal X-ray analysis.[109] A powder of crystals, however, contains a statistic distribution of all possible crystallographic orientations. When changing the angle of incidence each lattice spacing d will be detected once in average. A typical pattern relates the incoming angle θ to the intensity of the detected X-ray beam. The angles can be converted back into d -spacings via the Bragg equation. In the structural analysis of the NCs one takes advantage of bulk X-ray diffraction analysis and their reference patterns collected in databases.[110,111] Although NCs are single crystalline, powder XRD is the method of choice to determine their crystal structure. In practice, a highly concentrated NC solution is dropped onto a glass waver. The solvent evaporates and leaves a powder-like NC film behind containing NCs in random orientation. The patterns obtained are then compared to the database. With this a certain crystal structure can be identified. The small crystalline domains of NCs in the range of a few nanometer result in a broadening of the diffraction peaks.[110,111]

III.1.2 Electron microscopy for the investigation of the nanocrystal shape and composition

In 1933 the wavelike character of electrons was used for the first time to image small objects when Ernst Ruska built the first working electron microscope.[112] Since then much progress has been made to improve this instrument to explore materials at the nanoscale. Nowadays, all possible signals arising from the interaction of the electron beam with the sample are used to gain information about the materials structure, morphology or composition. In the following

paragraph some of the basic methods of electron microscopy that have been used to acquire information on the material system of interest will be presented. These methods are based on transmission electron microscopy (TEM). When used in imaging mode only, the operating principle of the TEM is comparable to that of the light microscope with the main difference being the use of electrons to image the structure rather than light. Electrons provide a much smaller wavelength than light. Together with proper lenses it is, thus, possible to get a much better resolution with the electron microscope than with the common light microscope.[113] In 1925, de Broglie discovered the wave-particle duality for the electron by relating the particle momentum p to its wavelength λ through the Planck's constant h and was awarded the Noble Price in Physics for his discovery:[114]

$$\lambda = \frac{h}{p} \quad \text{(III-2)}$$

Momentum p is transferred to the electron via acceleration through a potential V . The kinetic energy of an electron can thus be calculated by:[113]

$$eV = \frac{m_0 v^2}{2} \quad \text{(III-3)}$$

Where e is the electron charge, m_0 is the rest mass of the electron and v its velocity. With

$$p = m_0 \cdot v \quad \text{(III-4)}$$

this leads to the relationship between the wavelength λ of the electron and the acceleration voltage V :

$$\lambda = \frac{h}{(2m_0 eV)^{\frac{1}{2}}} \quad \text{(III-5)}$$

Equation (III-5) shows us an important concept: By increasing the acceleration voltage the wavelength of the electrons is decreased. At acceleration voltages of 100 kV the velocity of the electrons reach half the speed of light. In this range relativistic effects have to be taken into account and equation (III-5) changes to:[113]

$$\lambda = \frac{h}{[2m_0 eV(1 + \frac{eV}{m_0 c^2})]^{\frac{1}{2}}} \quad \text{(III-6)}$$

In Table III-1 this effect is listed for two different acceleration voltages. The first column gives the acceleration voltage, while the second and third columns depict the non-relativistic and the relativistic wavelength of the electrons in pm .

Acceleration voltage (kV)	Non-relativistic wavelength (pm)	Relativistic wavelength (pm)
100	3.86	3.7
300	2.23	1.97

Table III-1 Difference in wavelength of the accelerated electrons when taking relativistic effects into account.[113]

The electron source in a TEM can be either a field emission gun or a thermoionic gun. The latter, as the name suggests, produces electrons when heated. Acceleration of the electrons is achieved by connecting an anode to the electron source and applying the acceleration voltage. The anode acts as an electrostatic lens and produces the gun crossover of the electron pathway. In the further geometric arrangement of the electron microscope the strongest difference to the conventional light microscope is the use of electromagnetic lenses instead of glass lenses. In the light microscope the lenses are typically moved to change the focus, intensity of illumination or magnification of the image. The focal length is fixed. In the TEM the position of the electromagnetic lenses is fixed, while a change in the magnetic field is used to change their strength, *i.e.*, magnification or focus.[113]

Going through the TEM from top to bottom is illustrated in Figure III-2. The electron beam is directed to the condenser lens system first. Here, a demagnified image of the gun crossover is created. With the condenser aperture the minimum spot size and the beam intensity is controlled. In the imaging system the objective aperture improves contrast by removing high angle scattered beams. The objective lens forms the first image of the sample, while the projector lens further magnifies the image. The detection system usually consists of a phosphorus screen to allow direct observation of the electrons and it helps for the first adjustment of the microscope. Images are acquired with a CCD (Charge-coupled device) camera.[113]

The transmittance of a sample for electrons depends on the average atomic number of the elements and the thickness of the sample. Elements with higher atomic number appear to be darker, as electrons are scattered more strongly, similar for the thickness. When electrons hit the sample they interact with the outer sphere electrons or nuclei and induce several different signals from the sample, which can give information on the morphology, structure or composition of the sample. Electrons are elastically and inelastically scattered inducing a

number of different processes while the greatest amount of energy will be dissipated into heat. The elastically scattered electrons are used to create images. The inelastically scattered electrons may be detected to give element specific information. Further, the interaction of electrons with the material might result in the emission of X-rays from the sample characteristic of the elements in the sample.[113]

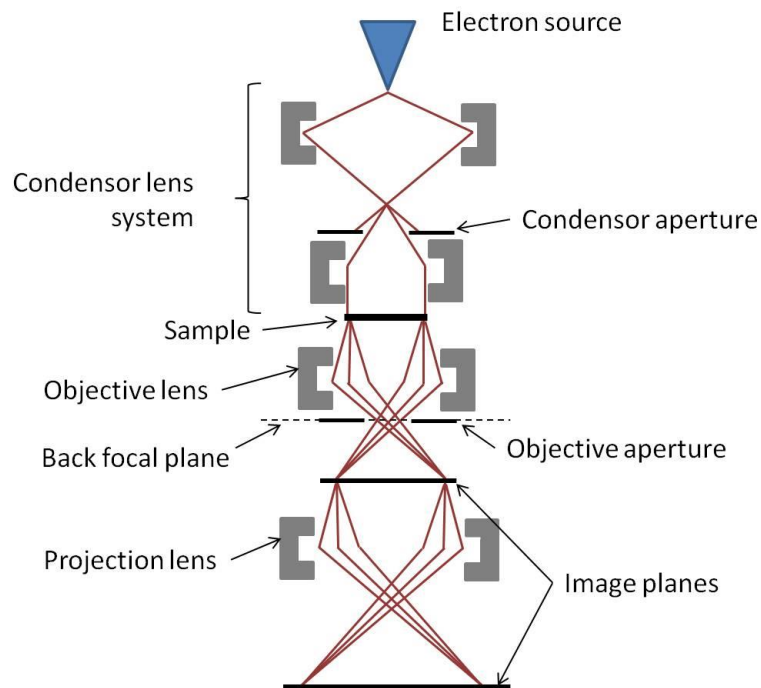


Figure III-2: Schematic of a transmission electron microscope (TEM).

Due to the nature of electrons showing wave-like characteristics, diffraction effects can be observed and nowadays electron diffraction (ED) within TEM is an indispensable part and a very useful aspect of TEM for material scientists. In a crystalline sample the electrons are diffracted causing a diffraction pattern in the back focal plane of the objective lens that can be imaged. An advantage over conventional diffraction experiments is the possibility to combine imaging in the TEM with diffraction.[113] In high-resolution TEM (HRTEM) the electrons are accelerated with voltages as high as 300 kV or higher. This imaging mode allows resolution of the sample at an atomic scale, making it a valuable tool to investigate crystalline material at the nanoscale. The imaging of the HRTEM is based on phase contrast.[113] Another tool in TEM is the detection of X-rays arising from the interaction of the electron beam with the sample. An incoming electron might interact with an inner shell electron such as to cause ionization of the sample. This leaves a hole behind at the lower lying energy levels. When the hole is filled by an outer shell electron, the energy difference will be emitted in form of an X-ray with a characteristic element specific energy. Detection of this X-ray

radiation allows the determination of the composition of the sample, such as in energy dispersive X-ray analysis (EDX).[113]

III.1.3 FTIR-spectroscopy: a tool to identify surface ligands

The basic principle of infrared (IR) spectroscopy is comparable to extinction spectroscopy (as explained in chapter III.2.1) with IR radiation used as a light source.[115] The absorption of radiation in the IR region typically leads to the excitation of vibrational states in a molecule. Thus, the absorption peaks in an IR spectrum represent the frequencies of the vibrational modes of two binding atoms in a molecule.[115] Certain molecular groups, such as amines, carboxyls, alcohols or C-H bonds absorb in a typical energy range. The spectrum represents a fingerprint of the investigated molecule, as no spectrum of two different molecules offers the same spectrum. This makes IR spectroscopy useful for several types of analysis, such as the identification of the surface ligands on a NC.[115] Fourier Transform Infrared (FTIR) spectroscopy is preferred over the simple transmission measurements, mainly because of the slow scanning process in conventional spectrometers.[41] With FTIR it is possible to measure all frequencies simultaneously, rather than individually. In an interferometer a beam splitter divides the incoming polychromatic beam into two beams. One beam is guided to a fixed mirror, while the other one is directed onto an adjustable mirror. After reflection, both meet again at the back of the beam splitter. Depending on the path difference between both beams a phase difference may occur that leads to interference when the beams combine.[41] After passing the sample the intensity is detected versus the displacement of the mirror in an interferogram (Figure III-3).[41]

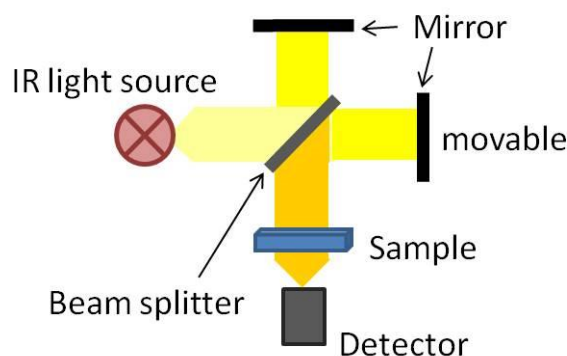


Figure III-3 Interferometer: From the IR light source a beam is guided to a beam splitter that splits the beam into two. One beam is directed to a fixed mirror, the other to a movable mirror. Both beams combine again at the back of the beam splitter. The movable mirror is typically moved a few millimeters, depending on the wavelength and the distance both beams travel.

The spectrum, typically given in wavenumbers, is then calculated via fourier transformation. The frequency range, in which signatures are expected, is in the region of 500-7500 cm^{-1} . Some functional groups of organic molecules are listed in the following table. Within this work, the technique described above has been used for the identification of surface ligands on the NC's surface.[115]

Functional Group		Characteristic Absorption (cm^{-1})
Alcohols –C-OH	<i>O-H</i>	3200-3700
	<i>C-O</i>	1050-1150
Alkane	<i>C-H stretch</i>	2850-3000
	<i>bending</i>	1350-1480
Amine –C-NH	<i>N-H stretch</i>	3300-3500
	<i>bending</i>	1600
	<i>C-N</i>	1080-1360
Carbonyl	<i>C=O</i>	1670-1820

Table III-2 Typical functional groups of organic molecules together with its characteristic absorption (cm^{-1})[115]

III.2 Optical spectroscopy

III.2.1 Absorption and scattering

Absorbance or extinction combines the optical processes of absorption and scattering. For very small nanoparticles the scattering contribution can be neglected and absorbance is equivalent to absorption. However, when investigating nanoparticles or clusters in a size range close to the wavelength of the incoming light, scattering might significantly contribute to the spectra. In the following paragraph, extinction spectroscopy will be introduced followed by the introduction of the measurement in an integrating sphere. This tool makes it possible to address the absorption without any contribution of scattering.

The extinction cross section C_{ext} (as already discussed in chapter II.2) is composed of both, absorption and scattering:[44]

$$C_{ext} = C_{abs} + C_{sca}. \quad (\text{II-12})$$

To measure the extinction cross section typically a light beam of a certain wavelength is passed through a solution containing the nanocrystals and the intensity before (I_0) and after passing the cuvette (I) is compared. The intensity I_0 of the incoming beam will be attenuated when passing the solution with N particles per unit volume, over a path length d (cm):[44]

$$I = I_0 \cdot e^{-C_{ext} \cdot d \cdot N} \quad (\text{III-7})$$

The Lambert-Beer law can be rewritten to address the extinction or absorbance A : [44]

$$A = \log_{10} \frac{I_0}{I} = C_{ext} \cdot d \cdot N \quad (\text{III-8})$$

Thus, a linear relation between the absorbance A and the concentration of particles in solution is given. In this work absorbance spectra were measured with a *Varian Cary 5000* UV-vis-NIR spectrophotometer. In Figure III-4 a sketch of such a spectrometer is given. The spectrometer is equipped with a Deuterium (185 - 350 nm) and halogen lamp (350 - 3300 nm) to cover the wavelength range from the ultraviolet (UV) to the near infrared (NIR). The wavelength of choice is selected through a double-grating monochromator and a variable slit. The equipment in principle and best case scenario allows a resolution down to 0.01 nm. The mirror switch then selectively guides the beam through the sample or through a reference sample. The intensity of both beams is measured with a detector and compared to give the final signal.[116]

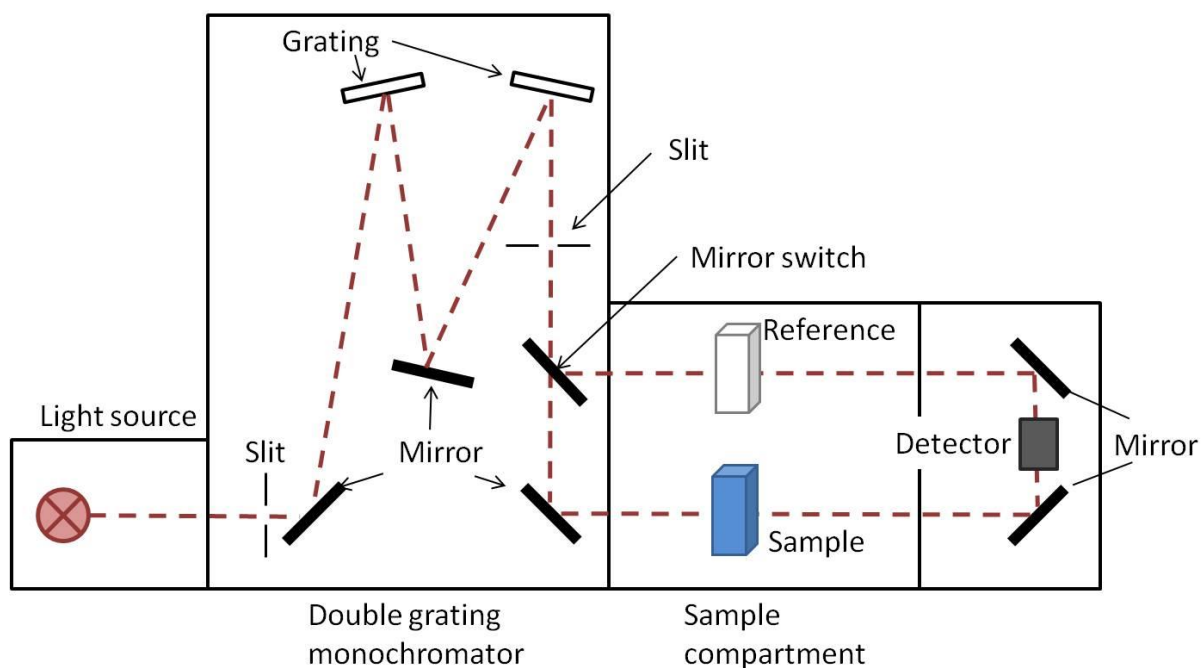


Figure III-4 Absorption spectrometer with double-grating monochromator. A mirror switch is responsible to guide the beam alternately through the sample and the reference. The beams are collected at the detector and its intensities are compared. [116]

Typically in this work spectra were measured up to the 3300 nm. In this region the vibrational states of the solvent molecules are excited. Thus, a strong contribution from solvent molecules in the spectrum is expected. To circumvent this we measured with the reference beam passing through a NIR transmitting quartz glass cuvette containing the pure solvent. In this way the vibrational fingerprint from the solvent is cancelled out to a good extent in the final spectrum. However, in regions of strong absorption artifacts will still be present. Solvents, such as tetrachlorethylene are therefore suggested for use in the NIR, since they do not exhibit strong vibrational contributions up to 3300nm.

When the light beam is attenuated by passing a sample several processes, such as absorption and scattering, may occur. In samples containing particles of sizes in the range of the incoming light wavelength, the scattering processes start to contribute to the absorbance spectra in such a way that it is important to separate the processes as to understand the contribution of each. This can be done by using an integrating sphere to measure the spectrum. An integrating sphere is a hollow sphere whose inner surface is coated with a diffusely reflecting material, typically barium oxide.[117]

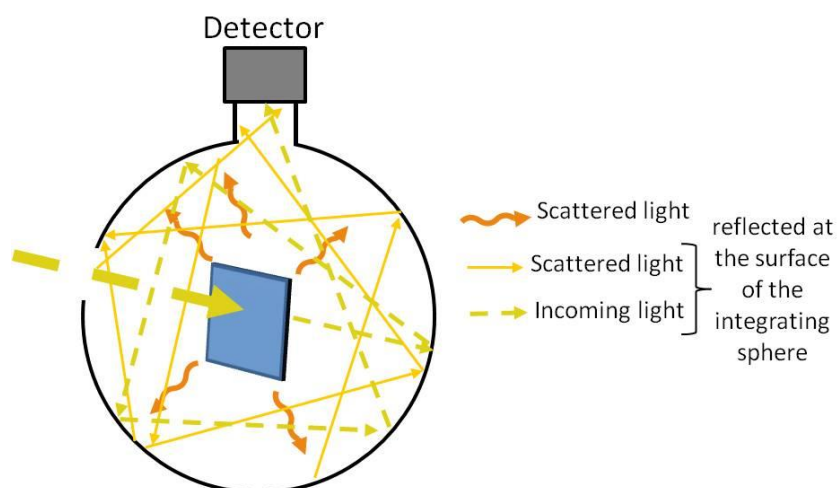


Figure III-5 Illustration of an integrating sphere: All light except of the absorbed light will eventually hit the detector. Thus, the only loss mechanism is the absorption of the sample.

When the light beam enters an integrating sphere it will hit the sample. The scattered light as well as the transmitted light beam will be scattered at the reflecting surface until it hits the detector. Thus, the attenuation of the incoming intensity is due to absorption only.[117]

III.2.2 Photoluminescence

When NCs absorb light of energy higher than the bandgap, the created charge carriers initially relax to the band edges by energy dissipation into heat. This process occurs on a picosecond time scale. The electron-hole pairs might result in Coulomb bound excitons that, when recombining radiatively, emit light. This process is termed photoluminescence (PL). Due to the Stokes shift the emission wavelength is red-shifted with respect to the absorption.[118]

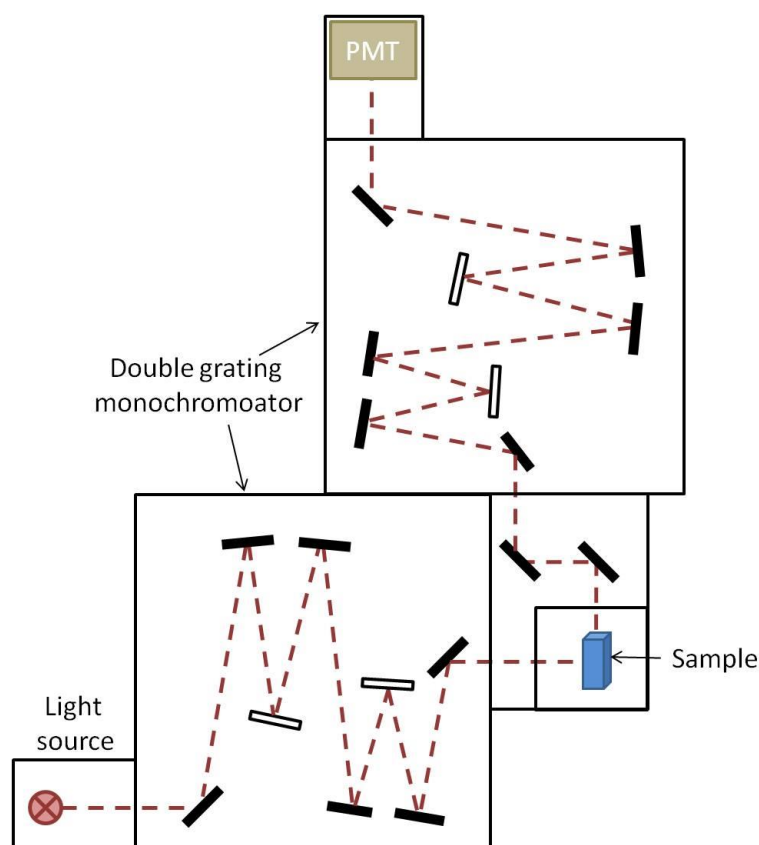


Figure III-6: Schematic representation of a double monochromator fluorometer with water cooled photomultiplier (PMT).[119]

In this work PL spectra were obtained with a double monochromator fluorometer (Fluorolog[®]-3 Model FL3-22 Horiba Jobin-Yvon).[119] A schematic depiction of the spectrometer is given in Figure III-6. The detector is a water cooled photomultiplier tube (PMT) sensitive in the visible range between 400 and 1000 nm.[119] The light source is a 450 Watt Xenon lamp. The beam of light is dispersed by a double-grating monochromator and the excitation beam (λ_{ex}) is directed to the sample compartment, as depicted in Figure III-6. The emission monochromator is installed perpendicular to the excitation beam to minimize the detection of scattered light from the excitation beam.[119] The emitted light is dispersed by a double-grating monochromator and detected with a water cooled PMT.[119] Typically, a PL spectrum is recorded by scanning the emission spectrometer and measuring

the intensity for each selected wavelength. The PL from high-quality NC samples with high quantum yields has a radiative lifetime of up to microseconds at low temperatures with respect to nanoseconds in bulk.[3] However, the lifetime can be strongly altered due to surface effects or non-radiative decay channels such as Auger type recombination.[120] Time-resolved PL measurements in this work were performed with a streak camera from Hamamatsu (C5680) combined with a spectrometer (Cromex, 40 g/mm grating). The frequency doubled output of a mode-locked Ti:sapphire laser (150 fs, 76 MHz) was used as excitation source at 400 nm.[121]

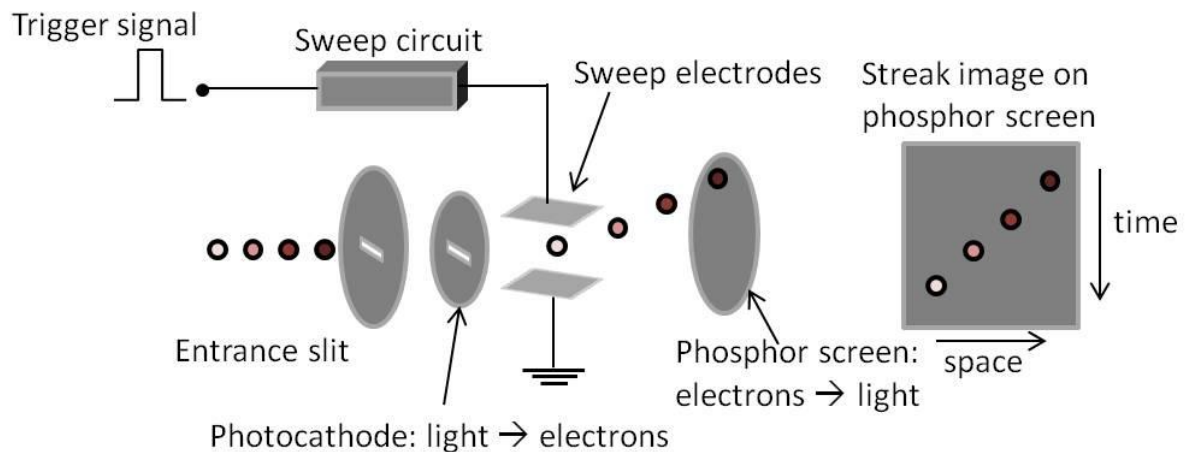


Figure III-7 Schematic illustration of the working principle of a streak camera. The incident light is directed onto a photocathode, where the photons are converted into electrons. Those are accelerated by the sweep electrodes and are linearly deflected in vertical direction according to their arrival time. Thus, the vertical direction on the phosphorous screen is representing the time axis. [121]

In Figure III-7 the operating principle of the streak camera is depicted. The measured photoluminescence is passed through a slit and is directed as a slit image onto the photocathode in the streak tube.[121] Here the photons are converted into electrons proportional to the intensity of the incoming light.[121] Thereafter the electrons are accelerated through a pair of accelerating electrodes (sweep electrodes) and bombarded against a phosphor screen.[121] A high voltage is applied to the sweep electrodes, synchronized in time with the incident light. This leads to a sweep of the electrons from the top to the bottom, as electrons that arrive at slightly different times are deflected in slightly different angles in the vertical direction. Thus, the vertical direction on the phosphorous screen serves as the time axis. The brightness of the phosphorous screen is proportional to the intensity of the incident light.[121]

III.2.3 Pump-probe spectroscopy

Pump-probe spectroscopy is a powerful tool to address carrier dynamics in NCs or to study the interaction between electrons and lattice vibrations (phonons) in metallic nanoparticles.[13] With this technique it is possible to measure those interactions in real time although occurring on time scales of picoseconds. Nowadays, femtosecond laser systems and nonlinear optical techniques, allow measuring with a resolution as short as 20 fs.[122]. The basic idea of pump probe spectroscopy is depicted in Figure III-8. The energetic pump pulse (green in Figure III-8) excites the system and by this perturbs its absorption. Thereafter the evolution of the system followed the excitation is monitored by measuring a change in transmission of a delayed, weak probe pulse.[122]

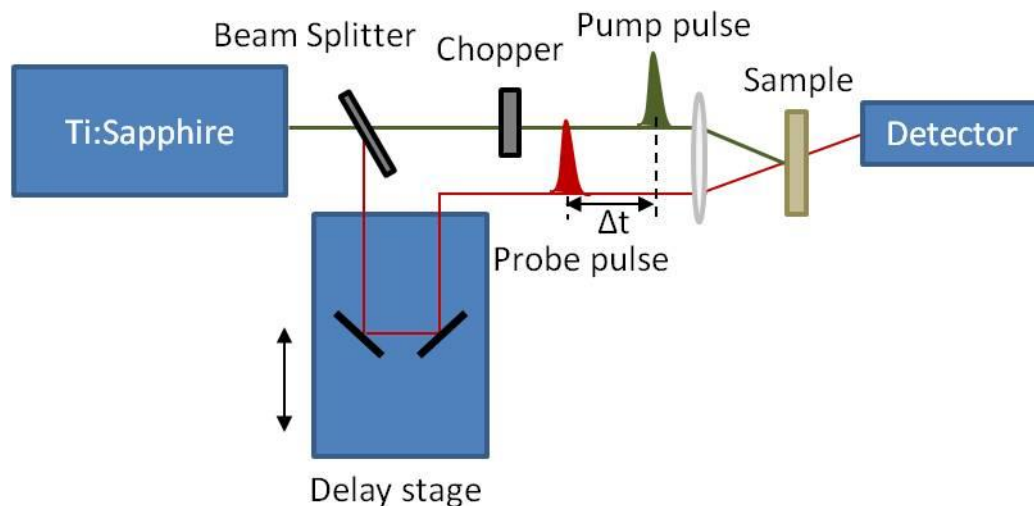


Figure III-8 In transient absorption spectroscopy uses two laser pulses are used, a strong pump and a weak probe focused and overlapped on the sample. The absorption of the sample is recorded while the probe is delayed in time relative to pump with a mechanical delay stage.[122]

By mechanically changing the optical path length of the pulses a delay between pump and probe is achieved.[122] This is controlled in a mechanical delay stage where the beam is delayed by changing the optical pathway the probe pulse has to travel. Two spectra will be recorded, one after excitation with the pump pulse and another without. A 3D-spectrum will be recorded, plotting the resulting differential transmission spectra versus time.[122] Ultrashort laser pulses, in this work were obtained by a 2 kHz Ti:sapphire amplified laser using the second harmonic at 400 nm for the pump beam and a white light continuum as probe.[34]

III.3 Sample preparation

For the synthesis of NCs the following chemicals were purchased:

Copper(II) chloride, copper(I) chloride, copper(II) acetylacetonate, ammonium diethyldithiocarbamate, tellurium (Te), selenium (Se), sulfur (S) trioctylphosphine (TOP), tributylphosphine (TBP), oleic acid (OA), octadecene (ODE), cadmium oxide (CdO), n-tetradecylphosphonic acid (TDPA), trioctylphosphine oxide (TOPO), oleic acid (OA), poly(methylmethacrylate) (PMMA, Mw 120 000 g/mol), and diisobutylaluminium hydride (DIBAH) were purchased from Aldrich and sodium oleate from TCI Europe. Oleylamine (OAm) and dodecanethiol (DDT) were acquired from Acros Organics. All solvents were anhydrous solvents of high purity purchased from Sigma-Aldrich. Syntheses were performed using standard air-free Schlenk line techniques. All chemicals were used as received.

III.3.1 Synthesis of Cu_{2-x}S superlattices

The experimental details for the synthesis of the Cu_{2-x}S superlattices as discussed in chapter IV.1.2 will be described in the following. Copper sulfide nanocrystals were synthesized as described in Ref. [123] from the thermolysis of a Cu-oleate complex in a mixture of OAm and DDT. The Cu-oleate complex was prepared by reacting 5.45 g of copper(II) chloride with 24.35 g sodium oleate in a solvent mixture of 80 mL ethanol, 60 mL water, and 140 mL hexane for four hours at ~ 60 °C. The green organic Cu-oleate complex is dissolved in the hexane phase. It is separated from the aqueous phase with the help of a separatory funnel and washed with 100 mL of distilled water for three times. The solid Cu-oleate complex is contained after the evaporation of hexane. For the synthesis of copper sulfide superlattices composed of 12 nm NCs, 0.318 g of the Cu-oleate complex was dissolved in a mixture containing 5 mL of OAm and 5 mL of DDT at room temperature. The addition of DDT leads to a color change from dark green to turbid white, which indicates the reduction of Cu(II) to Cu(I) by the sulfur compound. The reaction mixture was heated to 230 °C under nitrogen flow and kept at this temperature for 6 min while a gradual change from yellow to dark red, deep-brown turbid was observed. The NCs were precipitated by the addition of 10 mL of toluene and 10 mL of ethanol, and centrifuged for 10 min at 2500 rpm. The precipitate was redispersed in 10 mL of toluene. Sample washing was performed at ambient conditions to allow the plasmon resonance to develop.

III.3.2 Synthesis of stoichiometric and copper deficient copper chalcogenide nanocrystals

III.3.2.1 Synthesis of copper chalcogenide nanocrystals

The synthesis of copper based NCs was performed with standard, air-free Schlenk line techniques. The as-synthesized sample was transferred to a sealed and nitrogen filled vial via syringe or needle transfer before being transferred to the nitrogen filled glovebox for further treatment. To prevent any uncontrolled oxidation induced changes of the optical or structural properties, the NCs were precipitated under nitrogen atmosphere. For this the centrifugation tubes were sealed in the glovebox before taking out for centrifugation. After back-transfer to the nitrogen filled glovebox the supernatant was discarded and the precipitated NCs redispersed in anhydrous solvents in nitrogen atmosphere. Only anhydrous solvents were used. Via precise control over the contact to oxygen, the stoichiometric compounds with $x = 0$ were obtained. The copper deficient structures were prepared by opening the system to air until no changes in the optical spectra were observed.

Cu_{2-x}S nanocrystals

Copper sulfide NCs were synthesized following Ref. [92]. The sulfur precursor solution was prepared by dissolving 1.25 mmol of ammonium diethyldithiocarbamate in 10 mL of DDT and 17 mL of OA in a three neck flask and heating to 110 °C under Ar protection. Thereafter the copper precursor, prepared by dissolving 1 mmol of copper(II) acetylacetonate in 3 mL of OA was injected. The mixture was quickly heated to 180 °C and kept for 10 min. After reaction the solution was allowed to cool down naturally to 120 °C before being transferred to a nitrogen filled glovebox. The crude solution was centrifuged at 4600 rpm for 10 min. The supernatant was discarded and the precipitate redissolved in 5 mL of toluene. The washing process was repeated twice by precipitating the NCs by the addition of 10 mL *iso*-propanol and centrifugation at 4600 rpm for 10 min. After redispersion in anhydrous toluene the solution was stored in the nitrogen filled glovebox.

Cu_{2-x}Se nanocrystals

For synthesis of Cu_{2-x}Se NCs a mixture of 1.2 mmol of Se powder, 9 mL of ODE and 6 mL of OAm was heated in a three-neck flask to 120 °C and kept for 30 min under vacuum. The mixture was heated to 310 °C under nitrogen, when the solution turned orange. In a second three-neck flask the copper precursor was prepared by dissolving 2.0 mmol of copper(I)

chloride, 3 mL of ODE, and 2 mL of OAm, evacuating at 120 °C for 30 min, and subsequent stirring at 120 °C under nitrogen until the solution turned clear. The injection of the copper precursor into the Se precursor solution leads to an immediate color change to black and a temperature drop to ca. 285 °C. Thereafter the temperature was increased to 300 °C and kept for 20 min before cooling to room temperature, when the reaction mixture was transferred into the nitrogen filled glovebox. Separation of the NCs from the reaction solution occurred by the addition of either ethanol or *iso*-propanol, followed by centrifugation at 6000 rpm for 5 min. The NCs have been redispersed in anhydrous solvents such as toluene or TCE, and kept in the nitrogen filled glovebox for further use.[34]

Cu_{2-x}Te nanocrystals

To synthesize Cu_{2-x}Te NCs 0.6 mmol of copper(II) acetylacetonate were dissolved in 6 mL of OA and 3 mL of DDT. After heating to 160 °C a clear solution formed. 0.2 mL of a 1 M TOP-Te solution, prepared in the nitrogen filled glovebox by dissolving Te in TOP, was quickly injected, leading to an immediate color change to black. After reaction for 30 min the reaction mixture was transferred to the nitrogen filled glovebox. Precipitation occurred by adding 8 mL of anhydrous ethanol and centrifugation at 6000 rpm for 3 min. The supernatant was discarded and the brown precipitate redispersed in anhydrous solvents, such as toluene or TCE. The sample was kept in the glovebox for further use.

III.3.2.2 Oxidation and reduction experiments

To investigate the effect of oxidation on the crystal structure of copper deficient copper chalcogenides, a colloidal solution of the initially stoichiometric Cu₂Se NCs was dropped onto a glass substrate. The XRD pattern of the sample was measured in a nitrogen atmosphere sealed in an X-ray transparent dome. Thereafter the system was opened to air and measurements were recorded in certain time intervals. The optical properties were investigated by diluting Cu₂Se NCs of the same batch to the proper concentration. Extinction spectra were measured before exposure to air. After allowing oxygen diffusion into the previously sealed sample time dependent measurements were taken. For reduction experiments, a previously oxidized sample (12 h) was mixed with ca. 20 µL of a 0.02 M toluene solution of diisobutylaluminium hydride (DIBAH) under nitrogen atmosphere in a sealed cuvette. Importantly, remaining oxygen was removed from the sample prior to the addition of DIBAH by drying the NCs' solution under vacuum and redispersion into anhydrous solvents. Thereafter, extinction spectra were recorded every 10 min. To achieve a

complete suppression of the localized surface plasmon resonance, the addition of DIBAH was repeated several times until a total volume of 55 μL of DIBAH were added to 3 mL of the NC dispersion. A trace amount of OAm was added to preserve the colloidal stability. For a typical XRD experiment of the reduced Cu_{2-x}Se NCs, 5 μL of a 1 M solution of DIBAH to a dispersion of Cu_{2-x}Se ($x > 0$) NCs with a well-defined LSPR at 1290 nm in toluene were mixed in a nitrogen filled glovebox. The addition of ethanol quenched excess DIBAH and precipitated the NCs out. Finally, an XRD pattern of the reduced Cu_{2-x}Se NCs were recorded in a similar air-free way as described above. In a typical extinction and PL experiment, the Cu_{2-x}S NCs were oxidized by opening the samples to air and measuring extinction and PL spectra over a period of 10 h. For reduction experiments, the extinction and PL spectra of a diluted dispersion of Cu_{2-x}S ($x > 0$) NCs in anhydrous toluene were recorded in a sealed cuvette. After the back-transfer to the glovebox (any oxygen contact was avoided) 30 μL of a 0.1 M solution of DIBAH was added, thereafter the extinction and PL spectra were recorded over a time period of 5 h. For re-oxidation experiments, the same cuvette was opened to air for 1 h.

III.3.3 Ion exchange for the synthesis of Cu_{2-x}Te nanocrystals of various shapes

III.3.3.1 Synthesis of Cd based nanocrystals of various shapes

The synthesis and optical characterization of Cd based NCs as templates for the ion exchange reaction will be given in the following (discussion in chapter VI).

CdS nanorods

For the synthesis of CdS nanorods [124] a cadmium precursor solution (prepared by mixing 0.23 g of CdO (1.8 mmol), 0.83 g of TDPA (3.0 mmol), and 7 g of TOPO followed by degassing for 1 h at 80 $^{\circ}\text{C}$) was heated to 340 $^{\circ}\text{C}$ under nitrogen flow. A color change from dark red to clear indicates the formation of the Cd–TDPA complex. The sulfur precursor solution is separately prepared by dissolving 0.18 g of sulfur powder in 20 mL of TOP, and injected into the 300 $^{\circ}\text{C}$ reaction solution in steps of 0.4 mL each, every 2 min. The NCs were flocculated by the addition of a non-solvent such as ethanol. After centrifugation, the NCs were separated from the reaction mixture, redispersed in toluene and kept for further use.

CdSe nanorods

Following Ref. [125] the cadmium precursor was prepared by a mixture 1.6 mmol of CdO (0.205 g), 3.2 mmol of TDPA (0.89 g) and 3.11 g of TOPO in a three-neck flask. After heating to 120 °C for about 10 min under vacuum the temperature was increased to 310 °C under nitrogen flow until the solution turned clear. This temperature was kept for 10 min before cooling to room temperature and aging for about 24 h in nitrogen atmosphere. The Se injection solution was separately prepared by mixing 0.8 mmol of Se powder (63 mg) with 190 mg of TBP (0.463 mL), 1.447 g of TOP (0.483 mL) and 0.3 g toluene (0.347 mL) in a nitrogen filled glovebox and injected into the re-heated Cd-precursor solution (320 °C) resulting in a temperature drop to 300 °C. The reaction mixture was kept at this temperature for 8 min. A gradual color change from light orange to dark red and black was observed during reaction, thereafter the flask was allowed to cool down by removing the heating mantle. At 70 °C, 5 mL of anhydrous toluene was injected into the flask. After transfer into the nitrogen filled glovebox, the NCs were precipitated through the addition of 15 mL of anhydrous toluene and methanol followed by centrifugation (6000 rpm, 5 min) and decantation, repeated five times. The CdSe nanorods were dispersed in 2 mL of toluene and stored in the nitrogen filled glovebox for further use.

CdTe nanorods

0.120 g of Te powder was dissolved in 1320 μ L of TBP in the nitrogen filled glovebox and then diluted with 9 mL ODE. The Cd precursor solution was prepared by mixing CdO (0.08 g), OA (820 μ L), and ODE (5mL) in a three-neck flask and heating to 120 °C for 1h under vacuum. Thereafter the Cd precursor solution was heated to 300 °C obtaining a clear solution. At 300 °C, the Te precursor solution was swiftly injected and the reaction mixture allowed to cool to 260 °C where it was kept for 7 min for the growth of the CdTe nanorods. After reaction the solution was allowed to cool down to room temperature. The reaction mixture was diluted with 7 mL hexane and the NCs were precipitated with 14 mL methanol at 4000 rpm for 5 min. In the second washing cycle 20 mL of acetone were added to 15 mL of NCs in toluene. After centrifugation the supernatant was discarded and the NCs redispersed in 15 mL toluene. For transfer to the nitrogen filled glovebox the NCs solution was dried under vacuum, where they were redispersed in anhydrous toluene and kept under nitrogen for further experiments.[126]

CdTe dots

For synthesis of CdTe dots a modified synthesis protocol was used.[15] The Te injection solution was prepared by dissolving 0.501 g Te in 10.8 mL TOP. After 30 minutes of stirring at 275 °C the solution turned yellow indicating that Te dissolved in TOP. To remove undissolved parts the reaction solution was centrifuged at 4000 rpm for 1 min. Preparation of the Cd precursor solution was performed by mixing 102 mg CdO, 3.204 g TOPO, and 0.796 g ODPa in a 50 mL three neck flask. Thereafter the solution was degassed at 120 °C for 30 min and heated to 300 °C under nitrogen flow until CdO was dissolved and the solution turned clear. 1.8 mL of TOP were injected at 300 °C before the temperature was further increased to 320 °C. Then 0.54 mL of the Te-TOP precursor was injected into the hot solution leading to a temperature drop to 315 °C at which the reaction solution was allowed to react 7 min. The reaction mixture was allowed to cool down naturally to 70 °C, when 10 mL of anhydrous toluene were added to the flask. The reaction mixture was transferred to the nitrogen filled glovebox and the NCs were precipitated twice by the addition of anhydrous methanol and redispersion with anhydrous toluene. The sample was stored in the nitrogen filled glovebox for further use.

CdTe Rods

CdTe rods were synthesized following Ref. [127]. A mixture of 0.114 g CdO, 0.43 g TDPA and 7 g of TOPO was degassed at 120 °C for one hour, before the mixture was heated to 350 °C in nitrogen atmosphere until the solution turned clear. The Te injection solution was prepared by dissolving 0.255 g Te in 10 mL TOP to a concentration of 0.2 M under vigorous stirring for about 1h at 150°C in the nitrogen filled glovebox. At a temperature of 290 °C (Cd precursor solution) 0.5 mL of the Te-TOP precursor were injected followed by a temperature drop to 280 °C. The temperature was increased to 300 °C and 0.5 mL of the Te-TOP solution were added every 2 min until a total of 4 mL were injected. Thereafter the temperature of the reaction solution was cooled down to 70 °C for injection of 15 mL of anhydrous toluene via syringe. The resulting reaction solution was transferred to the glovebox, followed by precipitation with double the volume of anhydrous ethanol, centrifugation (6000 rpm, 5min), and finally redispersion in 10 mL toluene. This process was repeated twice.

CdTe Tetrapods

A typical synthesis of CdTe nanocrystal tetrapods was performed by following a modified protocol of Yu *et al.*[126] A 25 mL three necked flask was loaded with a mixture of 0.6 mmol

of CdO, 2.4 mmol of OA in 8 mL of ODE and heated to 100 °C under vacuum for 30 min. This mixture was further heated to 300 °C under inert (Ar) atmosphere, until the solution turned clear and colorless. After the reaction mixture cooled to 280 °C a mixture of 0.6 mmol Te in 0.6 mL of TOP and 1.4 mL of ODE was swiftly injected. For reaction, the solution was kept at 250 °C for 5 minutes, followed by cooling with a water bath until room temperature was reached and injecting 6 mL of toluene. The reaction mixture was purified by precipitation with an *iso*-propanol/methanol mixture and redissolved in toluene. The NCs' solution was dried and transferred into the nitrogen filled glovebox, where the NCs were redispersed in anhydrous toluene, and stored for further use.

III.3.3.2 Cation exchange reactions to synthesize Cu_{2-x}Te nanocrystals of various shapes

In the following, a detailed description of the ion exchange process will be given to synthesize Cu_{2-x}Te NCs of various shapes from preformed CdTe NCs. For the selenium and sulfur counterparts similar protocols were used. The CdTe NCs act as a precursor for the Cu_{2-x}Te synthesis. Therefore the NCs concentration was determined by following a standard procedure given in literature.[128] It is calculated by measuring the extinction coefficient of the NCs solution at the first excitonic peak of the CdTe absorbance spectrum. The absorbance A , the molar concentration c and the extinction coefficient C_{ext} are given in the linear relationship described in Lambert-Beer's Law:

$$A = \log_{10} \frac{I_0}{I} = C_{ext} \cdot c \cdot d. \quad (\text{III-9})$$

with d describing the path length of the cuvette, fixed to 1 cm. The empirical fitting functions as given in Ref. [128] for the extinction coefficient ($L/mol \cdot cm$) are given as follows.

$$C_{ext}(CdTe) = 3450 \cdot \Delta E \cdot D^{2.4} \quad (\text{III-10})$$

ΔE is the transition energy of the first excitonic absorption peak in eV and D is the diameter of the NC (nm). D can be calculated from the first excitonic peak by:

$$D(CdTe) = (9.8127 \times 10^{-7})\lambda^3 - (1.7147 \times 10^{-3})\lambda^2 + (1.0064)\lambda - (194.84) \quad (\text{III-11})$$

The concentration of the NC stock solution was determined by diluting an exact amount of the stock solution in 2 mL of toluene and the absorbance was recorded. With the density, the molar mass, the volume of the NC and the Avogadro constant N_A the number of Cd atoms in the solution has been calculated.[128] The Cu^+ stock solution was chosen to be a 10x stoichiometric excess and was prepared by dissolving of tetrakis(acetonitrile)copper(I) hexafluorophosphate in anhydrous methanol to 4 mg/mL in a nitrogen filled glovebox. Typically, 6 mL of anhydrous methanol, 1.5 mL toluene, 200 μL OAm, and 2 mL of the Cu^+ stock solution were mixed and 30 μL of the CdTe stock solution was added under vigorous stirring and kept there for 2 min. The ion exchanged NCs were precipitated by centrifugation at 6000 rpm for 5 min. The separated NCs were redispersed in 1 mL TCE. The supernatant was discarded. Note, for extinction measurements in the near-infrared the precipitated NCs have been dried using the nitrogen gun before redispersion in anhydrous solvents. This prevents any additional solvent peaks from remaining methanol in the spectrum. Without further treatment the NCs tend to aggregate after ion exchange. However, for optical analysis colloidal stability of the NCs is essential. For this 200 μL of OAm were added to the ion exchange reaction to allow for their stabilization in solution. After precipitation the excess ligands remain in the supernatant and are discarded. Note that the addition of DDT prevented the ion exchange, probably because DDT strongly binds to the Cu^+ ions in solution preventing the ion exchange reaction.

IV. Identifying the plasmonic nature of the near-infrared resonances in copper chalcogenide nanocrystals

Vacancy-doping is a key attribute of the entire family of copper chalcogenide nanocrystals (NCs), namely copper sulfide (Cu_{2-x}S), copper selenide (Cu_{2-x}Se), and copper telluride (Cu_{2-x}Te). The level of doping is expressed by $(2-x)$ in the chemical formula and accounts for a copper deficiency in the NC's lattice.[26,40,129] This is in turn responsible for an increased charge carrier density of $\sim 10^{21}/\text{cm}^3$ obviously evoking physical properties dominated by a metallic character.[48] In nanoscale structures, such a high level of doping ultimately leads to localized surface plasmon resonances (LSPRs) in the near-infrared (NIR), and indeed, strong resonances in the NIR dominate the extinction spectra of copper deficient copper chalcogenide NCs.[21,26,27,32,34,36-38] In the following chapter, evidence will be given for the plasmonic nature of this NIR band. In particular, it will be shown that the NIR resonance in copper chalcogenide NCs represents typical plasmonic characteristics, such as refractive index sensitivity or size dependence. Furthermore, copper chalcogenide NCs also benefit from their semiconducting nature in terms of chemical synthesis, which allows the production of highly monodisperse NCs that self-assemble into ordered superlattice arrays.[6] This opens an efficient route to investigate interparticle plasmon coupling, highlighting an advantage of copper chalcogenide NCs over conventional plasmonic nanomaterials.

IV.1 Localized surface plasmon resonances in copper chalcogenide nanocrystals

To investigate the nature of the NIR resonance in copper deficient copper chalcogenide NCs, Cu_{2-x}S , Cu_{2-x}Se , and Cu_{2-x}Te NCs with $x > 0$ were synthesized by precisely controlling their copper vacancy density (details described in chapter III.3.2).

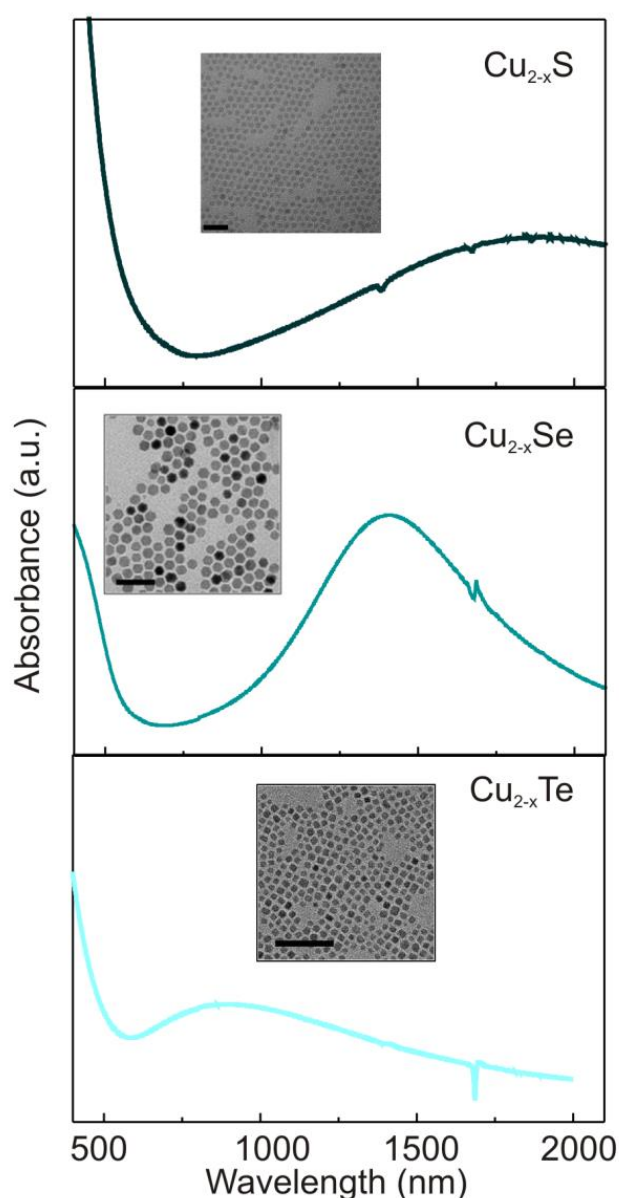


Figure IV-1 Absorption spectra for (a) Cu_{2-x}S NCs ($d = 5$ nm), (b) Cu_{2-x}Se NCs ($d = 12$ nm), and (c) Cu_{2-x}Te NCs ($a = 5$ nm). The insets show representative TEM images (scalebar 50 nm).[34]

Their extinction spectra together with representative TEM images are given in Figure IV-1 (Cu_{2-x}S, dark green curve, 5 nm in diameter, Cu_{2-x}Se, green curve, 12 nm in diameter, and Cu_{2-x}Te, turquoise curve, 5 nm edge length). All spectra are characterized by a steep rise in the blue wavelength region, which is attributed to the interband absorption, and a dominant resonance in the NIR. Copper deficient copper chalcogenides are characterized by an increased carrier density, which confined to small dimensions lead to localized surface plasmon resonances (LSPRs). As discussed in chapter II.2, a resonance is found when

$$\varepsilon'(\omega) = -2\varepsilon_m \quad (\text{II-27})$$

is satisfied. $\varepsilon'(\omega)$ is the real part of the dielectric function and ε_m the dielectric constant of the medium. From (II-27) and (II-20) we get the frequency ω_{sp} at which the resonance condition (II-27) is satisfied:

$$\omega_{sp} = \sqrt{\frac{\omega_p^2}{1 + 2\varepsilon_m} - \gamma^2} \quad (\text{IV-1})$$

ω_{sp} denotes the frequency at which the LSPR is found. γ depicts the damping constant, which for free carriers is equal to the plasmon linewidth. The bulk plasmon resonance ω_p is given as:

$$\omega_p^2 = \frac{ne^2}{\varepsilon_0 m_e} \quad (\text{II-19})$$

with the carrier density n , the electron mass m_e and charge e . Taking formula (IV-1) with ω_{sp} as the maximum of the NIR resonance, and γ the linewidth, the charge carrier density n is calculated to give values of $1,4 \cdot 10^{21} \text{ cm}^{-3}$, $1,6 \cdot 10^{21} \text{ cm}^{-3}$, and $5 \cdot 10^{21} \text{ cm}^{-3}$ for Cu_{2-x}S, Cu_{2-x}Se, and Cu_{2-x}Te NCs, respectively. This number is in agreement with previous findings for copper chalcogenides [26,88] and an increased carrier density correlates with the blue-shift of the plasmon resonance going from Cu_{2-x}S to Cu_{2-x}Se, and Cu_{2-x}Te.

As discussed earlier in this chapter, it is the copper vacancy density expressed as x that is responsible for the increased carrier density in the deficient copper chalcogenides ($x > 0$). It is further expected to be proportional to the carrier density, as with each Cu-ion an electron from the top of the valence band is removed, leaving behind an excess of holes.[26] Thus, the stoichiometry factor x represents a measure of the vacancy, and with this the carrier density of

the material. Structurally, x can be approximated from XRD analysis and assignment of the NCs to an exact crystallographic structure. Such an analysis revealed that the Cu_{2-x}S NCs can be assigned to $\text{Cu}_{1.97}\text{S}$ with $x = 0.03$, the Cu_{2-x}Se NCs to $\text{Cu}_{1.8}\text{Se}$ with $x = 0.2$ and finally Cu_{2-x}Te NCs to $\text{Cu}_{1.4}\text{Te}$ with $x = 0.6$. Please see appendix A.1 for further details. Taking into account, the volume V of the particle, the density ρ , and the molar mass M , the copper vacancies are calculated to give values of around $\sim 10^{21} \text{ cm}^{-3}$. This number clearly correlates with the carrier density that has been determined from the LSPR, and, thus, shows consistency with the assumption that each excess hole comes along with one copper vacancy. The discussion above emphasizes the interpretation of the pronounced NIR resonance as an LSPR, with the copper vacancies being responsible for the increased carrier density. Additional evidence for the plasmonic nature of the NIR resonance in the copper deficient ($x > 0$) NCs will be demonstrated in the following paragraphs. In particular, the sensitivity of the LSPR in copper chalcogenide NCs to the solvent refractive index ϵ_m will be demonstrated, its size dependence will be discussed, and the plasmon dynamics as determined via femtosecond pump-probe spectroscopy presented.

IV.1.1 Refractive index sensing with copper chalcogenide nanocrystals

To assign the studied NIR absorption bands in copper chalcogenide NCs to LSPRs the refractive index sensitivity of the NIR absorption band has been studied. According to equation (II-27) and (IV-1) the LSPR is sensitive to the embedding medium refractive index ϵ_m . [25] The sensitivity to ϵ_m is a characteristic typical for plasmon resonances. [25,66,130]

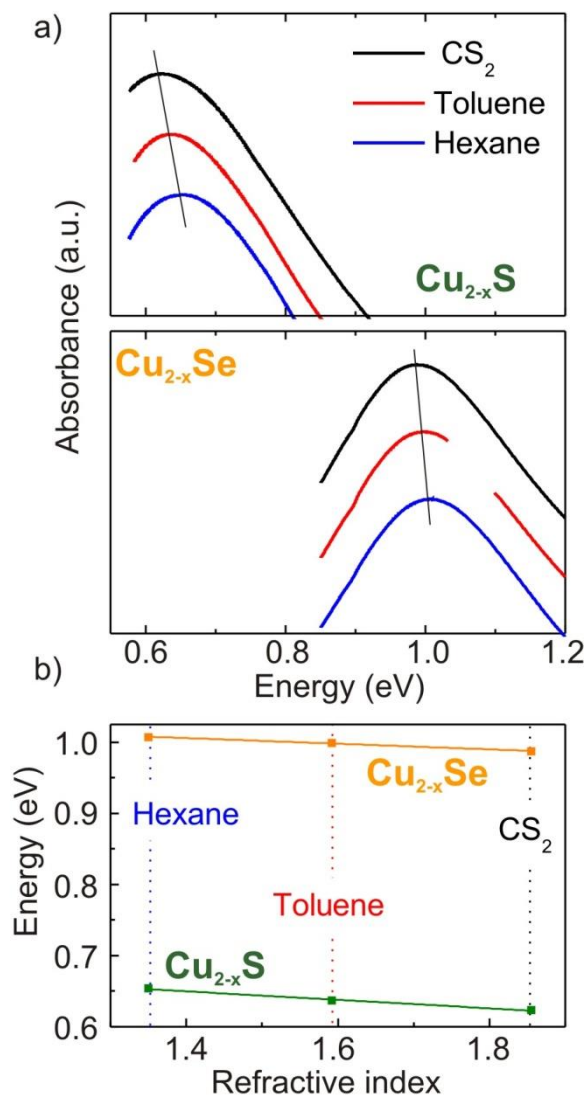


Figure IV-2 Plasmon resonances of (a) Cu_{2-x}S and Cu_{2-x}Se NCs in solvents of different refractive indices, CS_2 (black curve), toluene (red curve) and hexane (blue curve), spectra shifted for clarity. (b) Refractive index versus plasmon resonance in eV: Cu_{2-x}S (green line) and Cu_{2-x}Se (orange line). [34]

The LSPR of Cu_{2-x}S and Cu_{2-x}Se NCs with $x > 0$ in solvents with different refractive indices, namely hexane (1.38), toluene (1.50) and CS_2 (1.63) (Figure IV-2) were compared.

To prepare the samples, 20 μL of a 5 mg/mL NC dispersion was dried in a nitrogen filled glovebox and subsequently redispersed in 2 mL of the respective anhydrous solvent. An oxygen induced influence on the plasmon resonances was prevented by transferring the NCs into the different solvents in well controlled air-free conditions and with anhydrous solvents. The optical extinction measurements were performed in screwcap- and septum-sealed cuvettes to prevent any contact with air. In Figure IV-2a the extinction spectra for Cu_{2-x}S and Cu_{2-x}Se NCs in hexane (blue curve), toluene (red curve), and CS_2 (black curve) are shown. For reasons of clarity and comprehensibility the plot is given in energy scale and displayed in the region of the NIR band only. For both materials, Cu_{2-x}S and Cu_{2-x}Se NCs, a shift of the extinction maximum, *i.e.*, LSPR is observed. The shifts are summarized in Figure IV-2c where the LSPR peak position of the same Cu_{2-x}S and Cu_{2-x}Se ($x > 0$) NCs is plotted versus the refractive index of the solvent. A red-shift in the maximum of the NIR plasmon band with increasing refractive index of the solvent is observed. This behavior is expected for a plasmon resonance,[25,66] however so far mainly shown for noble metal nanoparticles.[26] In this work the sensitivity of the NIR band in vacancy doped copper chalcogenide NCs to the medium refractive index has been demonstrated. This highlights their plasmonic character and opens the route for plasmon sensing with copper chalcogenide NCs.[26,34]

IV.1.2 Intrinsic size effect of the localized surface plasmon resonance in Cu_{2-x}S nanocrystals

The size dependence of the LSPR in copper chalcogenide NCs has been investigated by synthesizing Cu_{2-x}S NCs of various sizes, namely 4.5 nm (red curve, Figure IV-3), 3 nm (brown curve, Figure IV-3), and 2.5 nm (black curve, Figure IV-3) in diameter. In Figure IV-3 extinction spectra of Cu_{2-x}S NCs together with representative TEM images are given. A broadening and progressive red-shift of the LSPR is observed with decreasing NC size. The LSPR is pronounced for the largest particles (4.5 nm) and weakened and broadened for smaller sizes. For sub 2.5 nm particles the plasmon resonance is completely damped.[34]

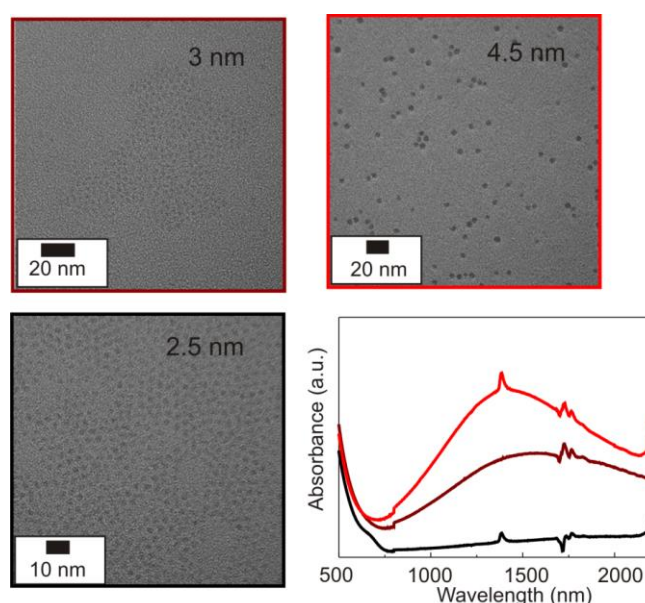


Figure IV-3 Extinction spectra of Cu_{2-x}S NCs of varying sizes with respective TEM images ranging from 4.5 nm (red curve), 3 nm (brown curve) to 2.5 nm (black curve) in diameter. Below 2.5 nm diameter the plasmon resonance is completely damped.[34]

Plasmon resonances are known to be intrinsically size dependent below a certain diameter (compare chapter II.2 for details).[66,131] This effect becomes important when the mean free path of the free carriers exceeds the nanoparticle diameter. The carriers scatter with the nanoparticle surface elastically and by this lose coherence more quickly, resulting in a broadening and red-shift of the plasmon resonance with decreasing nanoparticle size.[62,63] The discussion above demonstrates the intrinsic size effect of the plasmon resonance in Cu_{2-x}S NCs,[26,34] which can be attributed to the effect of surface scattering of free carriers.[62,63]

IV.1.3 Near-infrared plasmon dynamics in copper chalcogenide nanocrystals

Femtosecond pump-probe spectroscopy is a unique tool for the study of carrier dynamics and allows the time dependent identification of typical dynamical characteristics.[122] Thus, the nature of the NIR band in the same copper chalcogenide NCs as presented in the first paragraph of chapter IV, namely Cu_{2-x}S ($x > 0$, $d = 5$ nm), Cu_{2-x}Se ($x > 0$, $d = 12$ nm), and Cu_{2-x}Te ($x > 0$, $a = 5$ nm) has been investigated with femtosecond pump-probe spectroscopy.

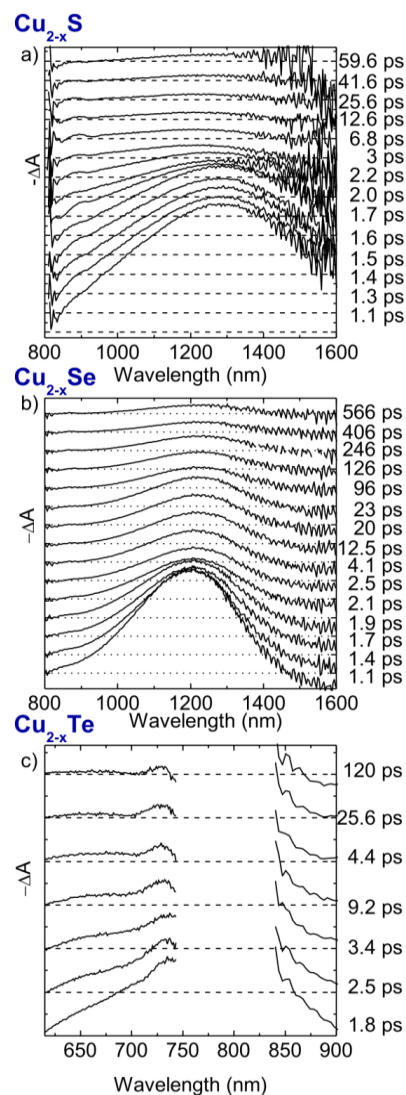


Figure IV-4 Transient absorption spectra of a) Cu_{2-x}S NCs ($x > 0$, $d = 5$ nm), b) Cu_{2-x}Se NCs ($x > 0$, $d = 12$ nm), and c) Cu_{2-x}Te ($x > 0$, $a = 5$ nm) NCs at different time delays after excitation at 400 nm with a femtosecond pulsed laser.[34]

Figure IV-4 displays transient absorption spectra of Cu_{2-x}S , Cu_{2-x}Se , and Cu_{2-x}Te NCs at different delay times after excitation after excitation with a femtosecond laser pulse in the

interband absorption regime at 400 nm. An optical non-linearity is observed in the spectral range of the LSPR. The observed feature suggests a broadening of the LSPR with respect to the steady state absorption (not shown here).[34] Note, for Cu_{2-x}Te NCs (Figure IV-4c) a gap in the transient spectra is observed, as here the plasmon resonance covers the region where the supercontinuum white light pulse does not allow measuring (spectral region from 750-850 nm), due to the high intensity and a non-continuous phase at the fundamental laser wavelength around 800 nm.[34]

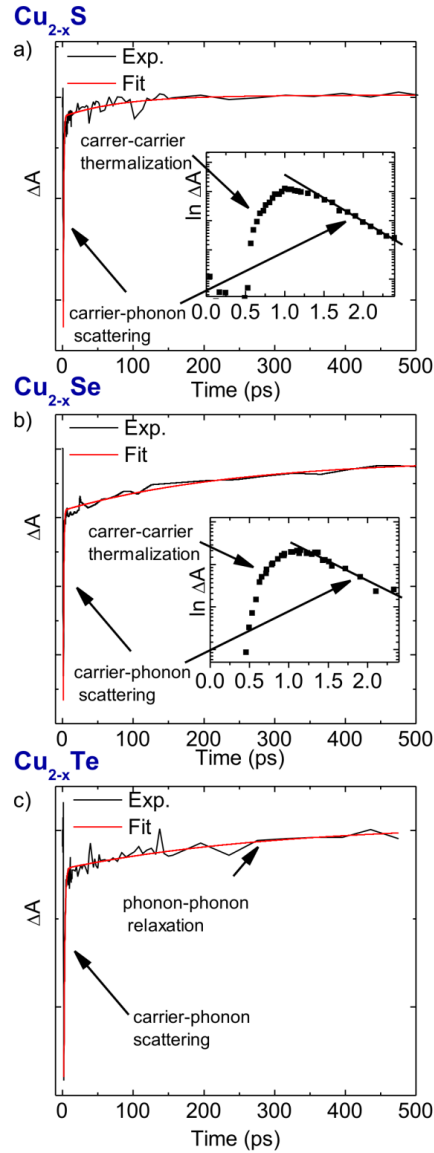


Figure IV-5 Recovery of the transient absorption signal for a) Cu_{2-x}S NCs ($x > 0$, $d = 5$ nm), b) Cu_{2-x}Se NCs ($x > 0$, $d = 12$ nm), and c) Cu_{2-x}Te NCs ($x > 0$, $a = 5$ nm) monitored at the bleach maximum at 1250 nm, 1200 nm, and 730 nm (not corresponding to the maximum), respectively, together with a bi-exponential fit. Inset: initial rise at short time scales plotted in logarithmic scale.[34]

The time evolution of the maximum non-linearity for Cu_{2-x}S , and Cu_{2-x}Se NCs at 1250 nm, and 1200 nm is given in Figure IV-5a and b and can be described by a bi-exponential decay. In both cases the initial decay occurs within the first 3 ps with time-constants of less than 1 ps. The second, longer decay for Cu_{2-x}S and Cu_{2-x}Se NCs takes place on a time scale with time constants of 85 and 250 ps. An initial rise is observed in the transient signal on shorter time scales (inset to Figure IV-5a and b, logarithmic scale). Please note that the time trace for the Cu_{2-x}Te NCs sample (730 nm) does not correspond to the maximum non-linearity due to the gap in the transient spectra. Nevertheless, the overall kinetics are represented here as well, with a two-step decay composed of a fast component decaying within the first picoseconds (time constant 1.5 ps) and second longer decay with a time constant of around 300 ps.[34]

A comparison of the carrier dynamics of copper chalcogenide NCs in the NIR with those of noble metal nanoparticles in the region of the LSPR revealed a very similar behavior.[73] The observed non-linearities in noble metal nanoparticles, caused by a laser induced heating of the carrier gas, results in a broadening of the LSPR with respect to the steady state absorption.[73] The kinetics of the transient spectra typically show a two step decay,[13] correlated to elevated temperatures of the carrier gas (initial decay) and the lattice (second decay) induced by the pump-pulse.[5] The first decay is understood as the carrier relaxation due to carrier-phonon scattering, leaving the lattice at elevated temperatures. The second decay is related to lattice cooling via phonon-phonon scattering with the surrounding medium. Similar to our results, the first decay is expected to occur within the first picoseconds, while the second longer decay occurs within ~ 100 ps.[5] After the initial excitation with the pump pulse carrier-carrier scattering, also termed carrier thermalization,[5] leads to a new Fermi electron distribution of the carrier gas corresponding to a higher carrier temperature.[74] This is the time the transient spectra need to be fully developed, and detected by an initial rise in the transient absorption spectra. It typically occurs within the first hundred femtoseconds.[5] In copper deficient ($x > 0$) copper chalcogenide NCs a similar response is found and the overall observations are consistent with the plasmon dynamics observed in noble metal nanoparticles.

The observed non-linearities of the plasmonic features can be explained by changes in the dielectric function induced by elevated carrier and lattice temperatures, T_C and T_L , respectively. To investigate the time evolution of the temperatures the two temperature model (TTM) has been introduced, which is represented by two coupled differential equations:[132]

$$C_C(T_C) \frac{dT_C}{dt} = -G(T_C - T_L) + P_A(t) \quad (\text{IV-2})$$

$$C_L(T_L) \frac{dT_L}{dt} = G(T_C - T_L) \quad (\text{IV-3})$$

where $C_C(T_C)$ is the carrier specific heat capacity and $C_L(T_L)$ the specific heat capacity of the lattice. G is the electron-phonon coupling constant. By fitting the differential spectra, the time dependence of the temperature T_C and T_L was identified, which reach values up to 10^4 K depending on the pump fluence. This is in agreement with a recently reported work on Cu_{2-x}Se NCs.[42] Because of the much lower carrier density in the copper chalcogenide NCs with respect to noble metals, a smaller carrier heat capacity results, which in turn leads to a much higher effective carrier temperature at comparable fluences.[42] Nevertheless, these results further support on the interpretation of the NIR resonance in copper chalcogenide NCs as plasmonic in nature.

IV.2 Interparticle plasmon coupling of Cu_{2-x}S nanocrystals in close packed superlattice arrays

The self-assembled organization of NCs into ordered arrays such as superlattice structures is a growing field in NC research.[6,133-139] To date superlattice structures of sub-millimeter dimensions have been produced.[6] The self-assembly process is based on the monodispersity of the sample. Provoked by slow evaporation of the solvent and triggered by natural forces such as entropy, electrostatics, and van der Waals interactions the NCs are caused to order into close packed superlattice arrays.[6,133] One of the major advantages of NC self-assembly is that the NCs in the superstructures are allowed to couple with each other to create a multifunctional response, while retaining the exceptional, physical properties of their NC building blocks.[6] This process is so far mainly observed for semiconductor NCs and rarely observed in noble metal nanoparticles due to their lack in monodispersity.[60,140] Interparticle plasmon coupling of plasmonic nanoparticles is of great interest for various applications including biolabeling or surface enhanced Raman spectroscopy,[60,140] but has so far only been observed for noble metal nanoparticles. In this chapter interparticle plasmon coupling in Cu_{2-x}S NCs is demonstrated for the first time while taking advantage of the self-assembly properties of monodisperse NCs into close packed superlattice arrays.

IV.2.1 Cu_{2-x}S nanocrystal superlattice arrays

To monitor the behavior of the plasmon resonance upon close packing, copper deficient plasmonic Cu_{2-x}S ($x > 0$) NCs of 12 nm size, have been synthesized, as described in the experimental section (chapter III.3.1).[123] Due to the very high monodispersity of the as-synthesized NCs the resulting dispersion typically consisted of 12 nm Cu_{2-x}S NCs arranged into close packed superlattice arrays of sizes ranging between 500 and 1000 nm. A typical TEM image illustrating these superstructures is given in Figure IV-6a. The hexagonal arrangement of the reflections in the small angle electron diffraction (SAED) micrograph (inset to Figure IV-6a) shows reflections at small angles characteristic of ordered NC arrays. This illustrates that the NCs pack into close packed layers further stacking into multilayer superlattices.[38] An estimated 4×10^4 Cu_{2-x}S NCs form a 600 nm diameter superlattice. Figure IV-6b depicts an ED micrograph of a NC superlattice, illustrating reflections rather

than rings. Those reflect an arrangement of the NC building blocks with a preferred crystallographic orientation.[38]

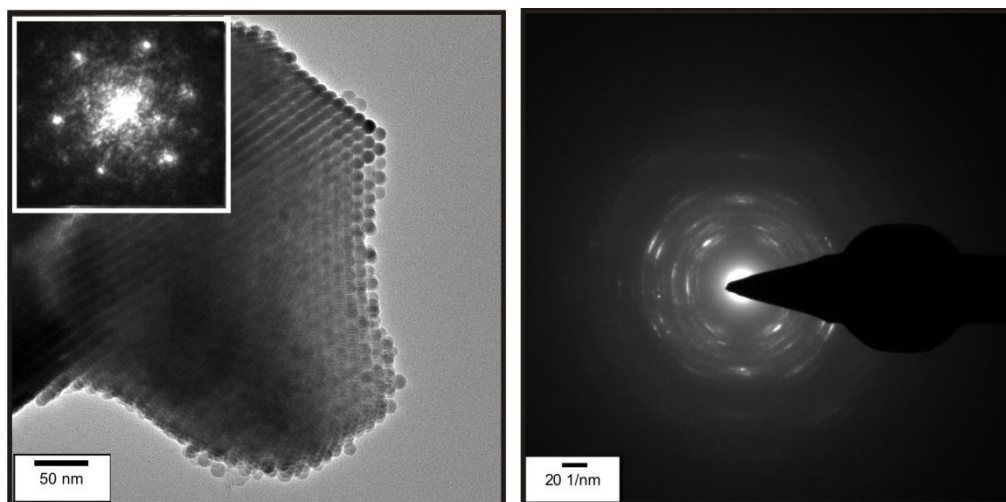


Figure IV-6 a) TEM image of Cu_{2-x}S NC superlattices, inset: SAED micrograph illustrating the high order in the superlattice. b) ED micrograph of a Cu_{2-x}S NC superlattice. The reflections indicate that all NCs order in the same crystallographic direction.[38]

IV.2.2 Blue-shift of the plasmon resonance upon ligand induced disassembly

To investigate the changes in the optical properties upon interparticle coupling, the careful disassembly of the NC superlattices was triggered by the addition of ligands (oleylamine, OAm) in excess, resulting in an exchange of the surface ligands. For details the reader is referred to the appendix A.2. The ligand induced disassembly of the NCs was confirmed by measuring the hydrodynamic radius of the NC dispersion before (1000 nm, size of the superlattices) and after the addition of OAm in excess (~17 nm, the hydrodynamic radius of the constituent NCs) (not shown here).[38] The optical properties were monitored upon the disassembly process. The extinction spectra are given in Figure IV-7 together with the respective TEM images of the close packed (red frame) and dispersed NCs (blue frame). Prior to each measurement, the sample was gently shaken to prevent sedimentation of the superlattices during measurement. The initial sample, containing the close packed superlattice arrays (red curve) shows a maximum of the plasmon resonance at ~1540 nm. After the addition of ligands in excess the spectrum gradually shifts until the plasmon resonance reaches a value of 1370 nm (blue curve), which corresponds to a blue-shift of approximately 170 nm and the plasmon resonance of the non-coupling NC. Interparticle coupling may occur when plasmonic nanoparticles are close enough to interact with each other, resulting in a red-

shifted plasmon resonance with respect to the non-coupling particles. While interparticle plasmon coupling is a well studied phenomenon in noble metal nanoparticles, it has not been demonstrated for plasmonic copper chalcogenide NCs, yet. These results demonstrate the plasmonic character of Cu_{2-x}S NCs and present an effective route to investigate interparticle plasmon coupling in copper chalcogenide NCs upon NC self-assembly into close packed superlattice arrays.

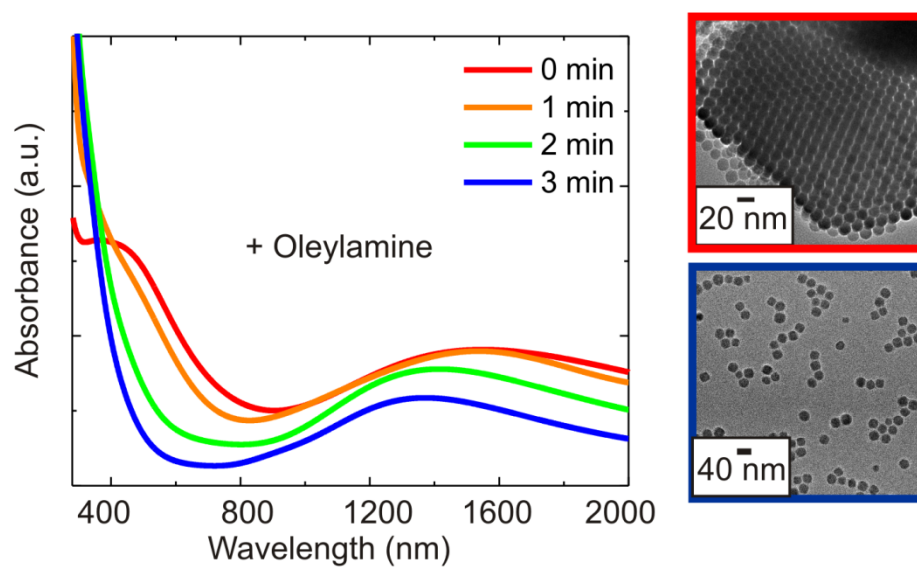


Figure IV-7 Changes of the absorbance spectra tracked with time after the addition of oleylamine together with representative TEM images of the close packed (red frame) and dispersed NCs (blue frame). The effect of NC close packing on the plasmon resonance is tracked with time. The absorbance spectrum of close packed NCs (red curve) shows a red-shifted plasmon resonance with respect to the dispersed NCs (blue curve). The disassembly process also leads to a blue-shift of the absorbance in the visible part of the spectrum.[38]

Another finding upon disassembly of the particles is observed in the visible part of the spectrum. Here, the spectrum of the superlattices appears to show a pronounced shoulder extending to the red part of the spectrum (red curve). Upon disassembly it gradually weakens (orange and green curves) until the resulting spectral profile after complete disassembly (blue curve) resembles the one of isolated Cu_{2-x}S NCs.[26,34,38] After disassembly an increased absorption in the blue part of the spectrum at ~ 400 nm is observed that gradually gains importance the more the disassembly process is promoted. During the disassembly process the concentration of NCs is constant, thus, the changes in the absorbance are not due to variations in the material's concentration. To exclude any influence of changes in the crystal

structure upon the addition of ligands in excess on the optical properties, the crystal structure of the NC superlattices and the dispersed NCs has been measured. However, no changes before and after their addition were found (not shown here).[38] These results suggest that the tunability of the optical properties toward the visible is due to NC close packing only.

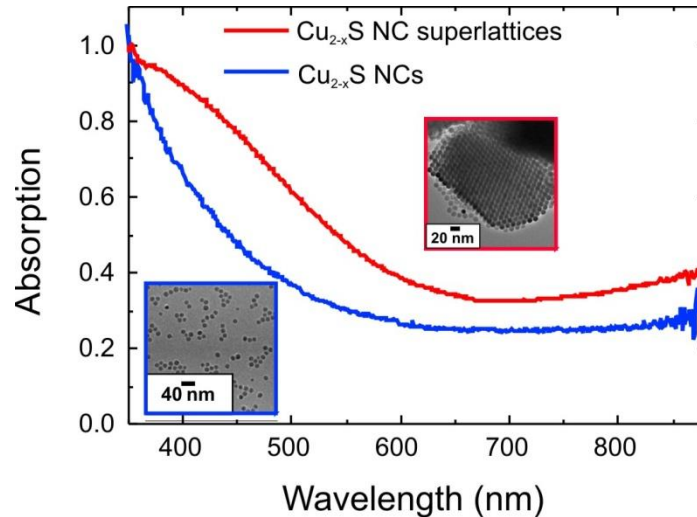


Figure IV-8 Normalized absorption spectra of Cu_{2-x}S NCs ($x > 0$) and NC superlattices dispersed in a PMMA matrix. Samples measured in an integrating sphere, excluding a scattering contribution to the absorption spectra.[38]

The measurements, as shown in Figure IV-7, have been performed in solution. A contribution due to scattering, especially from the NC superlattices, cannot be excluded. Therefore the same measurements were performed in an integrating sphere. This allows measurements of the pure absorption excluding any contribution of scattering. The scattered light is collected and the absorption can be directly accessed, as the sample absorption (A) is expressed by the $A = I - (T + S)$, with T being the transmitted and S the scattered light from the sample.[117] The measurements were performed by mounting films of NCs and NC superlattices dispersed in a PMMA matrix inside an integrating sphere. The red curve in Figure IV-8 corresponds to the absorption spectrum of a NC dispersion of Cu_{2-x}S NCs in a PMMA film. The absorption shows a profile typical for Cu_{2-x}S NCs in solution.[26,34,36,38] A steep decrease of absorption in the UV region toward the blue is attributed to the interband transitions, while the absorption in the rest of the visible is weak and overlapped by a broad background that increases towards the near-infrared. This absorption in the red is due to plasmonic absorption as discussed earlier in this chapter.[26,34,36,42] The weak absorption of the dispersed Cu_{2-x}S NCs observed in the visible is significantly enhanced toward the red in the spectrum of the NC superlattices (red curve). It is dominated by a pronounced shoulder at 400 nm extending in the red up to 700 nm. The residual absorption increasing toward the NIR is due to the

plasmon resonance. The observed red-shifts might be explained by electric field effects that occur due to the close packing of Cu_{2-x}S NC into superlattices. The presence of a dipole moment across the [100] direction in single Cu_2S NCs has been highlighted in a recent publication.[103] Beside the promotion of superlattice formation, an influence of appearing dipole moments on the optical transitions cannot be fully excluded. Here, the quantum confined Stark-effect could lead to a shift of the direct optical transition.[141,142] To get a better understanding of the effects responsible for the changes in the optical spectra, additional spectroscopic measurements such as transient absorption spectroscopy are required. These results clearly indicate that the absorption profile of Cu_{2-x}S NCs can be tuned toward the red part of the visible spectrum upon arrangement into close packed superlattice structures. This absorption in the visible is of great importance for the improvement of the light harvesting properties of Cu_{2-x}S NCs in solar energy conversion applications. Furthermore, these results demonstrate the excellent suitability of self-assembled monodisperse copper chalcogenide NCs for the investigation of plasmon coupling in this type of plasmonic material.

IV.3 Chapter Summary

In this chapter, the NIR resonances in copper chalcogenide NCs have unambiguously been identified to be of plasmonic nature. The plasmon resonance results from the high level of vacancy doping in the NCs, with the carrier density being proportional to the number of copper vacancies in the structure.[21,26,27,34,36,38] Indeed, the high efficiency of self-doping results in LSPRs located in the NIR. The plasmonic nature of the NIR band has further been confirmed by demonstrating refractive index sensitivity, the intrinsic size effect of the plasmon resonance below a size of 4.5 nm, and the plasmon dynamics. A key characteristic of this type of plasmonic material is related to its chemical synthesis that facilitates the production of highly monodisperse NCs that further self-assemble into ordered superlattices. This excellent self-ordering behavior of copper chalcogenide NCs allowed for the first time the investigation of interparticle plasmon coupling in this new type of plasmonic material.

V. Tuning the excitonic and plasmonic properties of copper chalcogenide nanocrystals

An appealing characteristic of vacancy doped copper chalcogenide NCs is their ability to exhibit localized surface plasmon resonances (LSPRs) in the NIR, as demonstrated in the previous chapter.[34,38] The high carrier density, responsible for LSPR formation, results from heavy vacancy doping, which dominates the structure of the copper deficient copper chalcogenide NCs ($x > 0$).[21,26,27,34,36,38] However, vacancy doped semiconductors further offer the opportunity to chemically control the number of vacancies in the structure, which in turn allows the exact tailoring of the carrier density. This results in the tunability of the LSPR over a wide range of frequencies and highlights an additional characteristic of plasmonic copper chalcogenide NCs. [20,27-35] A complete suppression of the LSPR is achieved by chemically filling the copper vacancies in the structure, which ultimately uncovers of the excitonic features present only in the stoichiometric NCs. Thus, the control over the structural characteristics facilitates to selectively address excitons and plasmons within one material. In this chapter, the tunability of the excitonic and plasmonic properties in copper chalcogenide NCs under oxidative and reductive conditions is presented. A special focus lies on the influence of the developing plasmon resonance on the excitonic transitions, as those come close in energy.[26,34]

V.1 Excitonic and plasmonic properties of Cu_{2-x}S nanocrystals

So far, an exact understanding of the structure dependent optical properties in copper chalcogenide NCs remained fairly uncovered.[32,36,82] The major cause is the uncontrolled synthesis of Cu_{2-x}S , Cu_{2-x}Se , and Cu_{2-x}Te NCs with exact crystallographic phases. In this work, stoichiometric ($x = 0$) and copper deficient ($x > 0$) copper chalcogenide NCs, as described in detail in chapter III.3.2, were synthesized demonstrating a careful control over their stoichiometry, *i.e.*, copper vacancy density.[34]

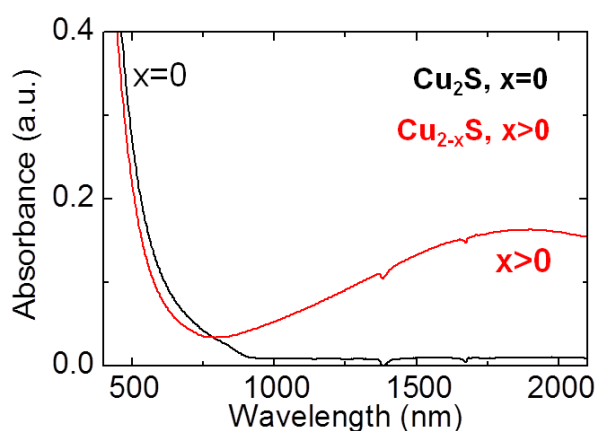


Figure V-1 Extinction spectra of stoichiometric ($x = 0$, black curve) and copper deficient ($x > 0$, red curve) Cu_{2-x}S NCs. The extinction below ~ 1000 nm is ascribed to interband transitions in both materials. In the stoichiometric NCs a weak excitonic feature is observed at the absorption onset ($x = 0$, black curve). In contrast, a pronounced band in the NIR dominates the spectrum of the copper deficient ($x > 0$) structure, which is attributed to a plasmon resonance due to the high carrier density of $\sim 10^{21}/\text{cm}^3$. [34]

In Figure V-1 the extinction spectra of Cu_{2-x}S NCs with $x = 0$ and $x > 0$ are given. The red curve corresponds to the extinction spectrum of the copper deficient Cu_{2-x}S NCs ($x > 0$) showing a pronounced absorption band in the NIR. This is ascribed to the LSPR as demonstrated in the previous chapter. On the contrary, the extinction spectrum of the stoichiometric compound ($x = 0$, black curve in Figure V-1) is characterized by a steep rise in the blue wavelength region, a low absorption onset at around 900 nm and no extinction in the NIR.[34] The absence of copper vacancies in stoichiometric copper chalcogenide NCs with $x = 0$ obviously alters the optical properties such as to be dominated by purely semiconducting properties. In semiconductor NCs of confined dimensions size dependent optical properties are expected when reaching sizes in the region of the exciton Bohr

radius.[3] In the optical spectra this effect is observed by a shift of the absorption onset with NC size and excitonic features in the spectra.[8] Those effects have been thoroughly investigated in the past for Cd-based chalcogenide NCs,[3] while in the Cu-based chalcogenides this discussion only recently started.[26,34,92] In the following, the optical response of Cu_{2-x}S NCs with $x = 0$ of varying size will be presented. Without a loss of generality this discussion is restricted to Cu_2S NCs while its findings are expected to hold for the entire family of copper chalcogenide NCs.

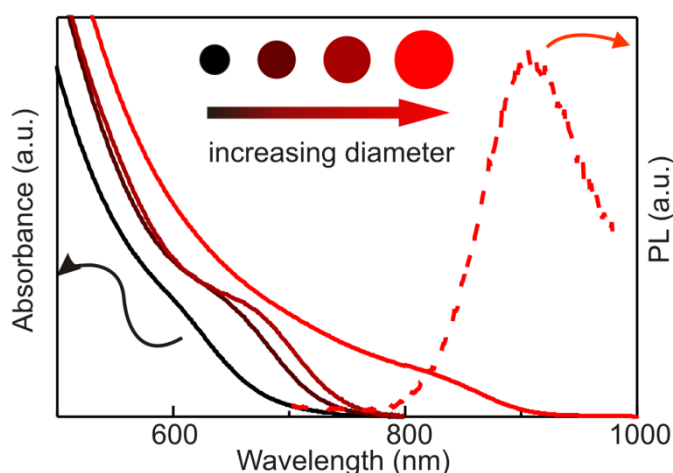


Figure V-2 Absorption spectra for Cu_2S ($x = 0$) NCs of varying size ranging from 2 to 5 nm (black to red curves) with the corresponding PL spectrum of the 5 nm NCs (dashed red curve).[34]

In Figure V-2 the absorption spectra of Cu_2S ($x = 0$) NCs of varying size ranging from 2 to 5 nm are given, where the black curve corresponds to the smallest particles and red to the 5 nm particles. A blue-shift of the absorption onset is found with decreasing NC size. Staying with the 5 nm particles (red curve), the absorption spectrum shows a shoulder at the absorption onset at around 900 nm. This absorption edge is blue-shifted with respect to the bulk bandgap (1.2 eV) [40] suggesting that the exciton Bohr radius has dimensions of at least 5 nm, a finding that experimentally confirms the estimated values from a recently published work.[36] Further, a size dependent blue-shift of the absorption onset with decreasing NC size proves that the NC dimensions have fallen below the exciton Bohr radius. A broad shoulder at the absorption onset is indicative for excitonic transitions. Only weak excitonic features are observed in the NC spectra in opposition to findings from Cd-based chalcogenide NCs, where strong peaks represent the excitonic transition.[13] Given in Figure V-2 (dashed red curve) is the corresponding PL spectrum of the 5 nm Cu_2S NCs, peaking at around 900 nm. A very low

fluorescence quantum yield Φ_f of $4E-4$ is found, which has been determined by optical measurements relative to a standard reference (details in the appendix A.2). The observed very low fluorescence quantum yield and broad excitonic features may be due to the band structure of the material that is characterized by an indirect lowest energy transition.[34] Nevertheless, the results presented in this chapter demonstrate the excitonic properties of stoichiometric Cu_2S NCs ($x = 0$), findings expected for the entire family of copper chalcogenide NCs.

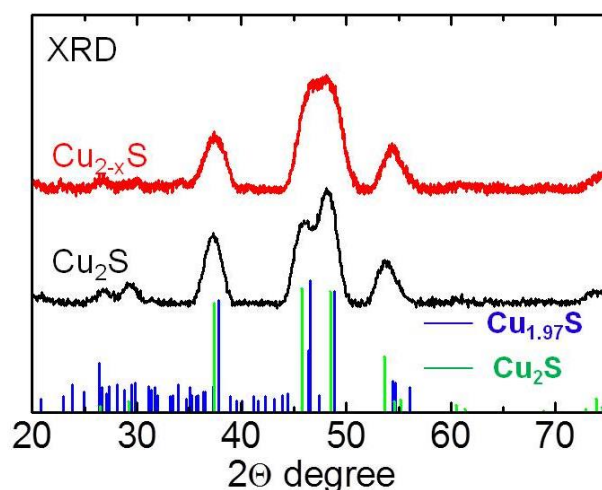


Figure V-3 XRD patterns of the Cu_{2-x}S NCs with $x > 0$, red curve, and Cu_2S NCs with $x = 0$, black curve; bulk reference stick powder patterns: green curves represent Cu_2S ($x = 0$) with chalcocite crystal structure and blue curves $\text{Cu}_{1.97}\text{S}$ ($x = 0.03$), with djurleite crystal structure.[34]

The crystallographic phases of copper chalcogenide NCs with $x = 0$, showing excitonic behavior, can be differentiated from the copper deficient, plasmonic phases ($x > 0$) via X-ray diffraction (XRD) analysis, as to each of them an exact crystallographic structure can be ascribed. In Figure V-3 the XRD patterns for the stoichiometric ($x = 0$, black curve) and copper deficient ($x > 0$, red curve) copper sulfide NCs of 5 nm in diameter, together with the respective powder reference stick patterns (green, Cu_2S , chalcocite and blue curve, $\text{Cu}_{1.97}\text{S}$, djurleite) are given. The small NC dimensions with crystalline domains of only around 5 nm are responsible for a significant broadening of the peaks. Both materials consist of large unit cells with complex crystal structures.[80] Although both structures are very similar, the NCs may be differentiated by the two main reflections at $\sim 47^\circ$ and 49° 2θ in both structures. In the copper deficient phase ($x > 0$, red curve) those strongly overlap, while those can be well distinguished in the stoichiometric phase ($x = 0$, black curve).[34] Taken together, an exact assignment of the excitonic ($x = 0$) and plasmonic ($x > 0$) Cu_{2-x}S NCs to a certain

crystallographic structure has been demonstrated, fulfilling the requirement for an investigation of their structure dependent optical properties. Further, these results demonstrate that by controlling the structural characteristics of copper chalcogenide NCs their excitonic or plasmonic properties can be addressed on demand.

V.2 Tuning the plasmonic properties upon controlled oxidation

For evaluation of the tunable optical properties, stoichiometric Cu_{2-x}S and Cu_{2-x}Se NCs with $x = 0$ have been prepared under air-free conditions as described in chapter III.3.2.

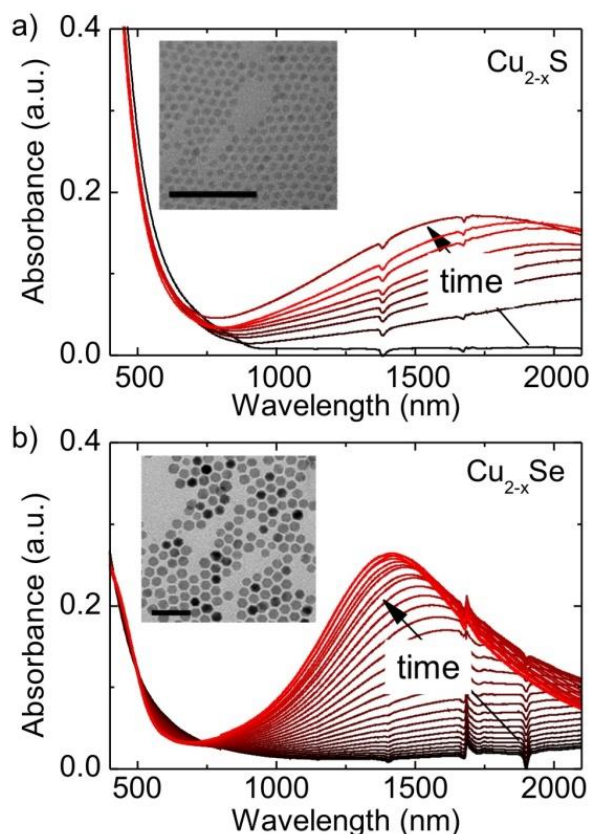


Figure V-4 Time evolution of the extinction spectra of stoichiometric (a) Cu_{2-x}S ($x = 0$, black curve) and (b) Cu_{2-x}Se ($x = 0$, black curve) NCs during oxidation for 6 days and 10 h (respectively). With exposure to oxygen the plasmon resonance gradually increases in intensity and blue-shifts with reaction time, indicated from black to red. The insets show representative TEM micrographs of the (a) Cu_{2-x}S and (b) Cu_{2-x}Se NCs (the scale bar is 50 nm).[34]

TEM micrographs of the as-synthesized NCs are shown in the insets in Figure V-4a (Cu_{2-x}S , ~ 5 nm) and b (Cu_{2-x}Se , ~ 12 nm). The extinction spectra of the stoichiometric NCs, with $x = 0$, are given as black curves in Figure V-4a and b. The spectra in both cases are characterized by a steep extinction at short wavelengths with a low intensity onset ~ 900 nm, and negligible extinction in the NIR. Such an absorption spectrum has been attributed to the purely semiconducting or excitonic properties of the stoichiometric compounds (refer to chapter V.1 for details). The effect of oxygen on the optical and structural properties has been examined. For this, the initially stoichiometric NC dispersion ($x = 0$, black curves in Figure V-4) has been opened to air to allow oxygen diffusion into the initially sealed samples. Upon exposure to oxygen the development of an NIR band in the NC spectrum is observed that gradually gains intensity and blue-shifts with increasing oxidation time (black to red curves, Figure V-4a and b). After *ca.* 10 h under oxidative conditions for Cu_{2-x}Se and *ca.* 6 days for Cu_{2-x}S NCs, no further spectral changes were observed and the NIR band is fully developed. These observations are in good agreement with recent studies of Cu_{2-x}S [26] and Cu_{2-x}Se NCs.[32] Focusing on the region of interband transitions at ~ 900 nm, it is observed that upon evolution of the NIR band also the lowest interband transitions are affected. This indicates an influence of the appearance of the plasmon resonance on the excitonic transitions in the NCs.[34]

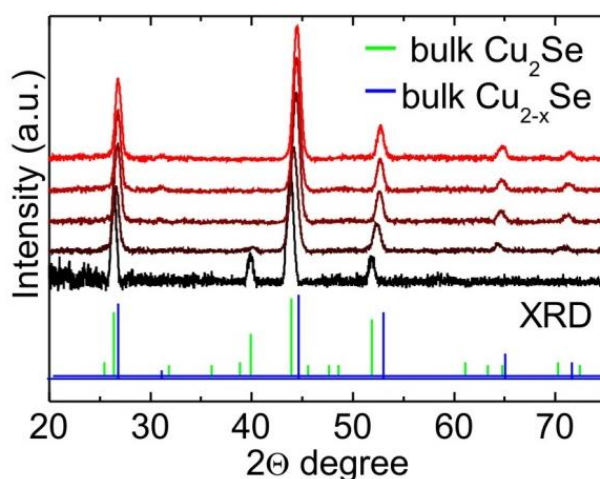


Figure V-5 Time evolution of the XRD patterns of the Cu_{2-x}Se NCs during oxidation, from the black to the red curve after 0 ($x = 0$, black curve), 15, 120, 220, and 320 min ($x = 0.2$, red curve) of air exposure. The vertical bars are the corresponding, color-coded, bulk reference patterns.[34]

A detailed analysis of the structural changes during the oxidation process has been performed on Cu_{2-x}Se NCs. The results are displayed in Figure V-5, with the time evolution indicated by a color change from black to red. The XRD pattern of the stoichiometric tetragonal Cu_{2-x}Se

NCs ($x = 0$) before exposure to air is given in black. A gradual transformation from the stoichiometric tetragonal phase Cu_{2-x}Se NCs ($x = 0$) into the non-stoichiometric, cubic phase Cu_{2-x}Se ($x = 0.2$) NCs is observed upon the exposure to oxygen, in agreement with previous reports.[82] In particular, after 15 min of oxygen exposure the main peaks at 26.2 , 43.8 and 51.8° shift to slightly higher 2θ angles, indicating a decrease in the lattice parameters. Simultaneously two peaks at 38.9 and 39.7° present in the stoichiometric, tetragonal Cu_{2-x}Se ($x = 0$) phase disappear and two peaks corresponding to the copper deficient, Cu_{2-x}Se ($x = 0.2$) appear at $\sim 65^\circ$ and 72° . After 320 min the pattern is fully developed and corresponds to the cubic Cu_{2-x}Se with $x = 0.2$. The results suggest a gradual transformation from the tetragonal, stoichiometric to the cubic, copper deficient phase upon air exposure. While TEM imaging confirms the preservation of the NCs original morphology (not shown here), the XRD measurements show that their stoichiometry and crystal structure are altered upon oxidation. This suggests a correlation between the evolution of the plasmon resonance and the transformation from stoichiometric (Cu_{2-x}Se , $x = 0$) to the copper deficient (Cu_{2-x}Se , $x > 0$) phase upon exposure to oxygen. As discussed in chapter II.3 the oxidation process leads to the creation of copper vacancies responsible for the formation of free carriers (holes) in the copper deficient NCs.[32,82] The more the oxidation process proceeds, the larger the stoichiometry factor x becomes. This is correlated to an increasing number of free carriers in the NC's valence band.[32] Free carriers localized to a confined volume give rise to plasmon resonances. Upon oxidation a blue-shift and increase in intensity of the plasmon resonance is observed, in accordance with a gradual increase in carrier concentration and copper vacancy density upon the oxidation. [26,36]

V.3 Suppressing the plasmon resonance via chemical reduction

In the previous section, the conducted experiments clearly demonstrated the oxygen induced formation of the NIR plasmon resonance in Cu_{2-x}S and Cu_{2-x}Se NCs. In the following chapter the back tuning of the plasmon resonance will be demonstrated. It is the addition of a reducing agent that leads to an opposite behavior, namely the suppression of the plasmon resonance and.

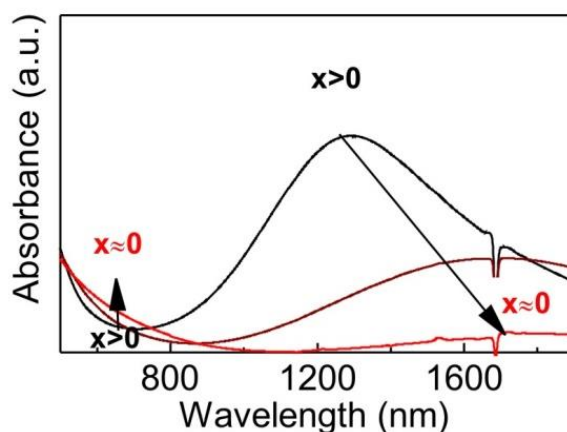


Figure V-6 Evolution of the extinction spectra upon the addition of DIBAH to a Cu_{2-x}Se ($x > 0$) NCs dispersion. The initial copper deficient ($x > 0$) sample shows a pronounced plasmon resonance (black curve), while after some time of reaction the plasmon resonance is suppressed, indicating a decrease in carrier density and copper deficiencies.[34]

Experimentally this is performed by the addition of a strong reducing agent, diisobutylaluminium hydride (DIBAH), to a dispersion of copper deficient Cu_{2-x}Se NCs ($x > 0$), as shown in Figure V-6 (black curve). The presence of DIBAH leads to a significant red-shift of the plasmon resonance and decrease in intensity, until its nearly complete suppression (red curve in Figure V-6). Further as indicated in Figure V-6 by the arrows, the addition of DIBAH and the suppression of the plasmon resonance results in a red-shift and increase of intensity in the region where the interband transitions are expected (~ 900 nm). This again indicates the influence of the plasmon resonance on the interband transitions.

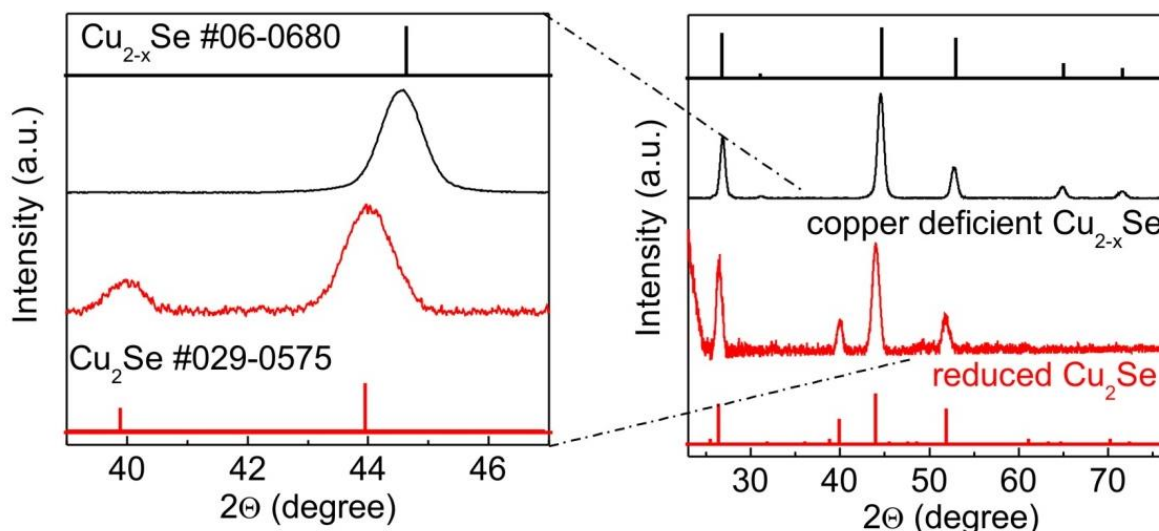


Figure V-7 Diffraction patterns of copper deficient Cu_{2-x}Se ($x > 0$) NCs (black curves), and the reduced Cu_{2-x}Se NCs (red curves) together with the respective reference patterns. Left is an enlarged region of the diffraction patterns illustrating the most significant changes in the patterns.[34]

The suppression of the plasmon resonance comes along with a decrease in carrier density and indicates a decreased number of copper vacancies. Structural analysis with XRD reveals that the plasmonic Cu_{2-x}Se NCs ($x > 0$, black curve, Figure V-6) are copper deficient cubic Cu_{2-x}Se with $x = 0.2$ before the addition of DIBAH (black pattern, Figure V-7). After the addition of DIBAH the XRD pattern indicates a recovery of the non-deficient, stoichiometric, tetragonal crystal structure of Cu_2Se ($x = 0$, red pattern in Figure V-7). This finding is in agreement with the observed suppression of the plasmon resonance for stoichiometric Cu_{2-x}Se NCs with $x = 0$ as seen in Figure V-6. Taken together, the addition of the strong reducing agent DIBAH leads to an injection of electrons to the NCs that drives the reduction of Cu^{2+} to Cu^+ . This entails a decrease of the copper vacancy density and with this a reduced number of free charge carriers in the structure, in accordance to a gradual red-shift and decrease in the intensity of the plasmon resonance. Moreover, a concomitant change in the crystal structure under the reductive conditions along with a change in stoichiometry, from the copper deficient ($x > 0$) to the stoichiometric ($x = 0$) is observed.

These results distinctly demonstrate the option to reversibly tune the copper vacancy density in copper chalcogenide NCs upon oxidation and reduction, in turn responsible the development and suppression of the LSPR. Upon the exposure to oxygen the plasmon resonance is formed, while upon the addition of a strong reducing agent the plasmon resonance is suppressed. Further, the crystal structure changes between the stoichiometric

($x = 0$) and the copper deficient ($x > 0$) structures under oxidative and reductive conditions along with the optical properties.[34]

V.4 Probing the causes of copper vacancy formation

Elemental analysis was performed to answer the question of the mechanism of copper removal from the NCs, *i.e.*, the formation of copper vacancies and its insertion into the lattice upon oxidation and reduction. In particular, ICP-OES (Inductively Coupled Plasma - Optical Emission Spectrometry) of digested NCs and SEM-EDS (Scanning Electron Microscopy-Energy Dispersive Spectroscopy) was carried out on the copper deficient Cu_{2-x}Te NCs exhibiting a plasmon resonance at around 900 nm (compare Figure IV-1c).[34] A Cu:Te atomic ratio of the NCs very close to 2:1 was found. This number suggests a stoichiometric composition, which is in contradiction to the observed plasmon resonance that indicates a copper deficiency. This might be explained by the fact that Cu(II) species under oxidative conditions do not leave the NCs but remain bound to the NC surface and contribute to the overall Cu:Te ratio.[34] To confirm that Cu(II) does not leave the copper chalcogenide NCs during the oxidation/reduction cycle, non-oxidized, stoichiometric and oxidized, copper deficient copper selenide NCs were precipitated and the remaining supernatants were inspected by ICP-OES. In both supernatants the concentrations of copper ions was very low, 3.4 mg/L and 1.9 mg/L, respectively. However, a significant increase of copper concentration is expected in the supernatant of oxidized, copper deficient Cu_{2-x}Se NCs if removed copper entered the solution in form of molecular species. A diffusion of 10% of copper ions present in the Cu_2Se NCs into the solution would lead to an increased concentration of copper of about 50 mg/L, which was not observed.[34] Both experiments lead to the assumption that Cu species form a thin layer at the NC surface, most probably forming a layer of CuO or as a monolayer of Cu(II) atoms bound to surface ligands. A similar mechanism has been suggested by Riha *et al.*[82] and is discussed in chapter II.3.1. Further, the addition of DIBAH to the solution leads to a suppression of the LSPR and filling of the copper vacancies. This occurs without the addition of an external Cu(I) source and indicates that Cu-ions can be reinserted into the lattices from these surface layers.[34]

V.5 Plasmon induced quenching of the excitonic transitions

The evolution of the plasmon resonance appears to significantly affect the region of the interband transitions of copper chalcogenide NCs upon both, the oxidation and reduction experiments, as already demonstrated in Figure V-4 and Figure V-6, respectively.

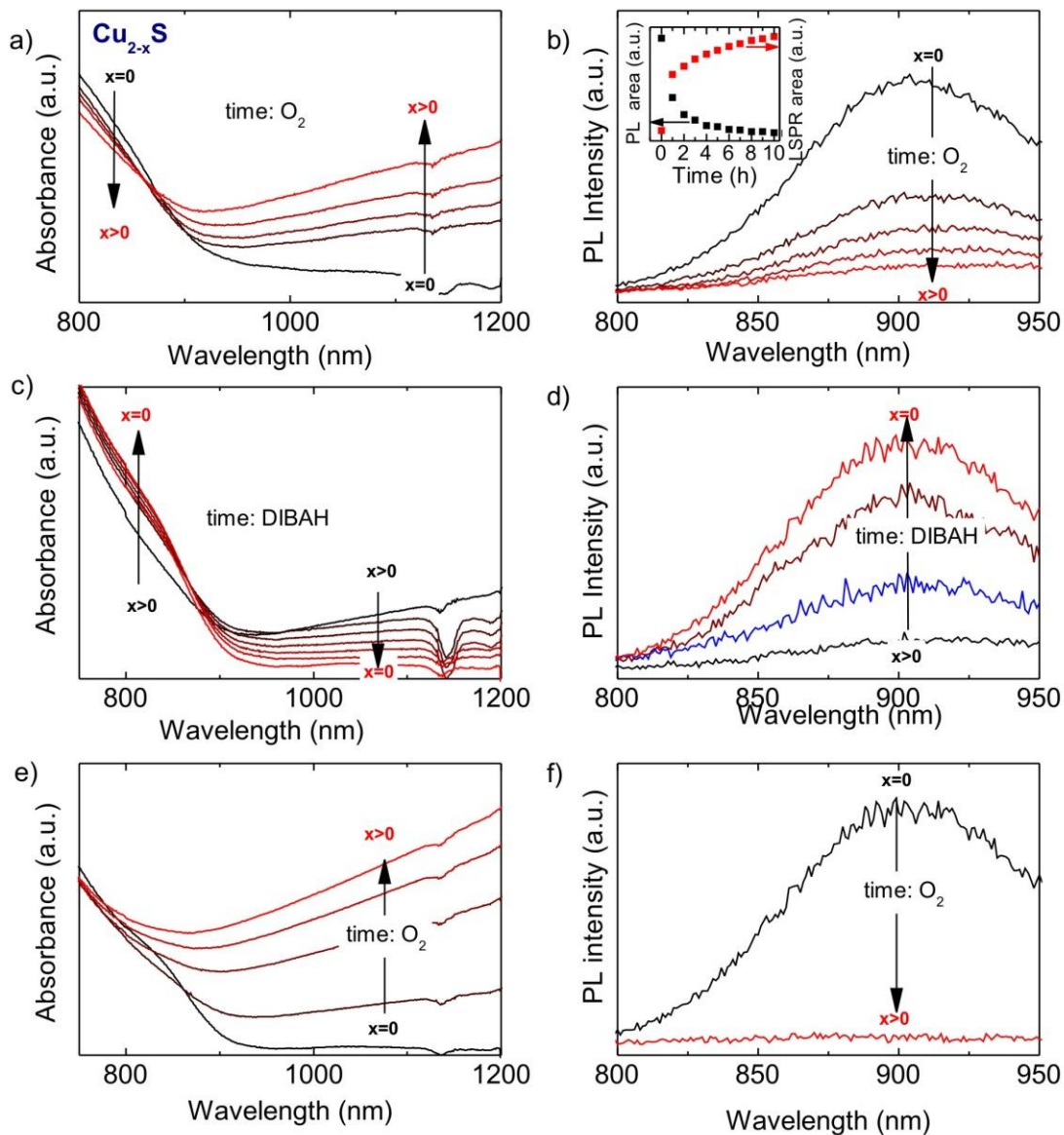


Figure V-8 (a) Extinction spectrum of Cu_{2-x}S NCs upon oxidation (black to red curves), (c) its reduction after the addition of DIBAH (black to red curves), and (e) its re-oxidation (black to red curves) together with the corresponding PL spectra (b) oxidation, (d) reduction, and (f) re-oxidation (always black to red curves). Blue curve in (d) shows the PL intensity before oxidation as reference (as given in (b), black curve).

The following discussion focuses on Cu_{2-x}S NCs as to evaluate the role of plasmon formation on the interband transitions. In stoichiometric Cu_{2-x}S NCs ($x = 0$) the interband transition is characterized by broad excitonic features and a weak PL (compare chapter V.1). Nevertheless, PL is a measure for the radiative recombination associated with such excitonic transitions and as such PL spectroscopy is a powerful tool for its investigation.[34] The extinction and PL spectrum of Cu_{2-x}S NCs ($x = 0$) before exposure to air is displayed in Figure V-8a and b (black curves), respectively.* This sample was then opened to air for a few seconds to trigger the reaction with oxygen. Thereafter spectra were recorded after 1, 2, 4, and 10 hours of reaction time (Figure V-8a, black to red curves). Upon the evolution of the plasmon resonance, the disappearance of the excitonic feature after the first hour of reaction is observed, followed by a gradual blue-shift and decrease in intensity with reaction time (Figure V-8a, black to red curve). PL quenching is observed by a factor of ~ 2 after the first hour of reaction until it is completely quenched after 10 h of reaction (Figure V-8b, black to red curves). The inset to Figure V-8b gives the correlation of the plasmon band evolution and the quenching of PL as a function of time. It shows that the kinetics of PL quenching shows similar trends as the evolution of the plasmon resonance. [34]

In the following the reverse tuning of the LSPR and its influence on the excitonic transitions will be presented. The black curve in Figure V-8c and d shows the extinction and PL spectrum of a slightly oxidized Cu_{2-x}S ($x > 0$) NCs dispersion displaying a plasmon resonance in the NIR and a very weak PL, respectively. Upon the addition of DIBAH the plasmon resonance decreases in intensity and red-shifts until it is completely suppressed (Figure V-8c, black to red curves). Notably, the broad excitonic features characterizing the initially non-oxidized samples are recovered upon the suppression of the plasmon resonance (Figure V-8c, red curve). Simultaneously, the PL spectra display a significant increase in intensity (Figure V-8d, black to red curve), with the intensity of the final PL after the complete reaction with DIBAH exceeding the intensity of the initial, non-oxidized sample (blue curve in Figure V-8c). Taken together the reduction experiments indicate a complete recovery of the initial optical properties upon the suppression of the plasmon resonance. These findings indicate a recovery of the initial interband transitions, related to the Burstein-Moss effect of heavily doped semiconductors, as discussed in chapter II.3. It further explains the blue-shift of the absorption edge in the copper deficient structure with respect to the stoichiometric one.[89] The PL intensity after reaction with DIBAH, which exceeds the PL of the initial non-oxidized

* Note that the extinction spectra are plotted in the region of the interband transition (800 nm - 1200 nm), thus, the LSPR peaks are not shown in the graphs and LSPR evolution is observed as an increased NIR absorption, only.

Cu_{2-x}S NCs, indicates that a significant number of free charge carriers are present in the initial Cu_{2-x}S NCs ($x = 0$) that contribute to PL quenching before exposure to oxygen, although not evolving in a detectable plasmon resonance.[34]

Finally, the same samples were again opened to air to trigger the oxidation induced evolution of the NIR plasmon resonance (black to red curves, Figure V-8e), giving rise to a subsequent PL quenching (black to red curves, Figure V-8f). The oxidation kinetics occur on a much faster time scale when compared to the initial sample (Figure V-8a and b), which suggests that the reduced sample is in a more labile state and more prone to oxidation after a first reduction cycle.

These results show that with oxidation and reduction a reversible effect can be observed on the excitonic transitions. The exposure to oxygen leads to an evolution of the plasmon resonance, a loss of the excitonic feature in the extinction and a quenching of PL intensity. On the other hand, the addition of a reducing agent evokes the suppression of the plasmon resonance, inducing a complete recovery of the initial excitonic properties. This indicates that the occurrence of the plasmon resonance (coming along with an increased carrier density) promotes a higher probability of non-radiative recombination in our NCs.

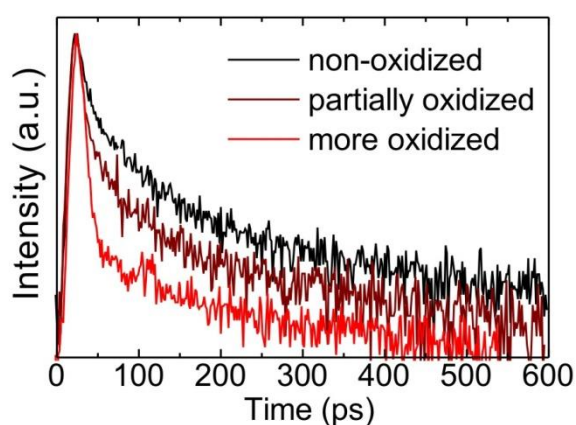


Figure V-9 Time-resolved PL spectra of stoichiometric ($x = 0$, black curve) and oxidized, copper deficient Cu_{2-x}S NCs ($x > 0$, brown and red curves), excited at 400 nm. The extent of oxidation increases from the black to the red. The corresponding extinction spectra (not shown here) show an increasing NIR plasmon resonance upon oxidation.[34]

To further evaluate this, the effect of plasmon resonance formation on the excitonic transitions has been investigated by means of time-resolved PL spectroscopy (Figure V-9). Upon the evolution of the plasmon band in the NIR (black to red curves Figure V-9, corresponding PL and extinction spectra not shown) the PL intensity is quenched concomitant with a shortening of the exciton lifetime. The three traces given in Figure V-9

(at $\lambda_{\text{max}} = 900$ nm) are characterized by a bi-exponential decay with a fast initial component of 10 ps which corresponds to the time resolution of our setup, and a second longer decay on a timescale of about 100 ps. In the course of oxidation the amplitude of the fast initial component gains in intensity. This is reminiscent of a multiparticle interaction, such as Auger recombination.[143] Auger recombination is an expected process, since upon oxidation the particles carry an increased density of holes that can interact with the exciton leading to non-radiative decay of the electron-hole pair. Carrier trapping might also play a significant role related to the number of copper vacancies created in the structure or the change in surface chemistry upon oxidation. Furthermore, it cannot be excluded that the PL quenching is partially influenced by the energy transfer from the exciton to the plasmon. Nevertheless, the observed influence of oxygen, *i.e.*, plasmon evolution on the excitonic transition has to be taken into account regarding their possible application in photovoltaics.[34]

V.6 Chapter summary

In this chapter, the unique property of copper sulfide NCs to hold excitons and LSPRs in one structure has been demonstrated. In particular, it has been shown that those characteristics can be selectively addressed by controlling the crystal structure, *i.e.*, vacancy density of the NCs. This exact tailoring of the copper vacancy density further highlights the attractive feature of reversible tunability of the plasmon resonance in copper chalcogenide NCs over a wide range of frequencies in the NIR (1000 - 2000 nm), controlled via oxidation and reduction. The tunability also reflects itself in the excitonic properties, where a quenching and recovery of the excitonic transitions is a result of the controlled plasmon tuning. The high charge carrier density in the NCs upon plasmon formation indicates an Auger type recombination, while a partial influence of the energy transfer from the exciton to the plasmon might also be envisaged. A more detailed study on the carrier dynamics of both, the exciton and the plasmon, is required to uncover the fundamental influence of the LSPR on the exciton. To summarize, the results demonstrated in this chapter deliver a better understanding of the optical characteristics of vacancy-doped copper chalcogenide NCs related to their structural properties. Furthermore, copper chalcogenide NCs offer the unique possibility to hold highly tunable LSPR and excitons on demand. As such they might hold as an appealing material system for the investigation of exciton plasmon interactions.[34]

VI. Free carriers or carrier localization? – Deviation from the usual Drude model

An outstanding property of copper chalcogenide NCs is their ability to hold tunable localized surface plasmon resonances (LSPRs) in the NIR.[26,32-35,38,42,45,144] In particular, as shown in the previous chapter, it is the manipulation of the copper vacancy density in the structure that allows the control over the LSPR.[26,31,32,36] This characteristic represents an additional means of tunability of the plasmon resonance with respect to noble metal nanoparticles.[26,32,34] To describe the plasmonic properties of copper chalcogenide NCs theoretically, mainly the Drude model has been used.[26,27,32,33,35-37,42,45,145] This is reasonable, as characteristics, such as refractive index sensitivity,[26,34] interparticle plasmon coupling,[38] or plasmon dynamics [34,42] imply a consistent behavior of the plasmon resonances in copper chalcogenide NCs and noble metal nanostructures.[32,42] Discussions mainly focused on spherical nanoparticles, assuming a free carrier metal-like behavior of copper chalcogenide NCs.[26,27,32,33,35,36,42] Only to a minor extent also anisotropic shapes such as rods or disks have been examined.[33,35,37,45,145] For a full examination of the dielectric properties, however, the treatment of various shapes with one given dielectric function is of major importance. Up to now a weak synthetical control over precise shapes with direct one-pot synthesis approaches have anticipated such an investigation. Copper sulfide (Cu_{2-x}S) and copper selenide (Cu_{2-x}Se) NCs of various shapes,[37] such as spheres,[36,82,92,98,99,103,104] nanorods,[45,105] and platelets [105-107] have been reported, while the direct synthesis of their tellurium counterparts still remains poorly controlled.[146-149] In the following chapter, the advantage of ion exchange reactions to synthesize copper telluride (Cu_{2-x}Te) NCs of precise shapes, such as spheres, rods and tetrapods will be presented, thereby specially focusing on the exact evaluation of their shape dependent optical properties. A direct comparison of the experimental results with theoretical

modeling provides insight into the character of the NIR resonances in copper chalcogenide NCs.

VI.1 Shape dependent extinction of Cu_{2-x}Te nanocrystals

In ion exchange reactions the insertion and exchange of cations in ionic NCs leads to chemical transformations. These come along with a concomitant modification of their crystal structure and composition, while the initial NC morphology is retained.[16,46-51,150] This advantage has been utilized within this work to synthesize Cu_{2-x}Te NCs of various shapes, namely spheres, nanorods, and tetrapods, by using CdTe NCs as templates for the ion exchange reaction. Those were produced through standard procedures, as described in detail in chapter III.3.1.[126,127,151] In the cation ion exchange process the initial CdTe NCs are transformed to Cu_{2-x}Te NCs upon the addition of Cu^+ to the initial CdTe NC dispersion. While Cd^{2+} is exchanged by Cu^+ the initial shape of the NC is persevered. In that way Cu_{2-x}Te spheres of 9 nm in diameter, rods of ~5 nm in width and 21 nm in length, and tetrapods with an arm length of ~12 nm and an arm width of ~5 nm, have been produced. The ion exchange process was confirmed via optical spectroscopy, X-ray diffraction (XRD) analysis, energy dispersive X-ray analysis (EDX) and electron diffraction (ED). Shape preservation of the Cu_{2-x}Te NCs after ion exchange is confirmed with TEM. The reader is referred to the appendix A.4 and A.5 for details. Respective TEM images of the as-synthesized Cu_{2-x}Te NCs are given in Figure VI-1(a-c) together with their corresponding absorption spectra. In all three cases the spectrum is characterized by a steep absorption increase for the short wavelength attributed to the interband transitions, and a pronounced band in the NIR ascribed to the LSPR (as thoroughly discussed in chapter IV and V). The LSPR for the spheres is located at ~1074 nm, with the absorption approaching zero further in the NIR (Figure VI-1a). For the rods and tetrapods the NIR band is found at ~1069 nm and 1103 nm with the absorption extending to the NIR up to 3300 nm, above which our measurement setup is not sensitive (Figure VI-1b and c). Remarkably, the absorption to the NIR does not result in a pronounced peak, but is rather broad and only slightly increasing in intensity at the red end of the spectrum. This has further been confirmed via fourier-transform IR (FTIR) spectroscopy showing a broad featureless absorption up to 500 cm^{-1} (refer to the appendix A.6).

Remarkably, the Cu_{2-x}Te NC shape does not present a strong influence on the extinction spectrum. These results appear to be in stark contrast to findings from strongly plasmonic material such as gold (compare chapter II.2). Due to strong electric fields sensitive to the nanoparticle shape and its boundary conditions a strong shape dependence of the extinction spectrum is observed. Moreover, in elongated structures, such as nanorods, two distinct features characterize the spectra, representing the excitation of the carrier oscillations along and perpendicular to the nanorod axis (compare chapter II.2).[39] This however is not observed in the rod spectrum of the Cu_{2-x}Te NCs.

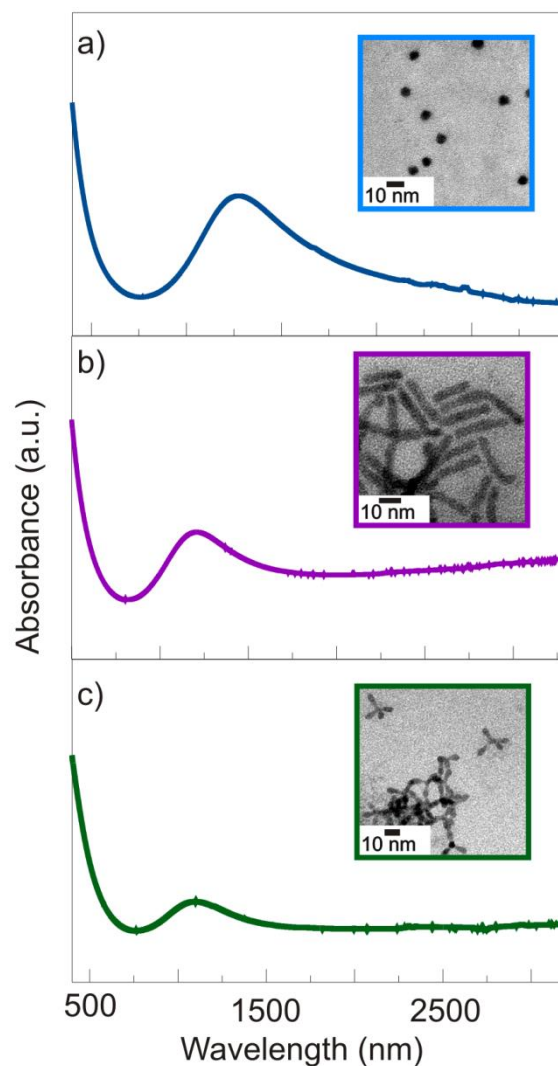


Figure VI-1 Extinction spectra of the ion exchanged Cu_{2-x}Te NCs (a) spheres ($\lambda_{\text{max}} = 1074 \text{ nm}$), (b) rods ($\lambda_{\text{max}} = 1069 \text{ nm}$), and (c) tetrapods ($\lambda_{\text{max}} = 1103 \text{ nm}$) together with representative TEM images.[39]

VI.2 Optical modeling of Cu_{2-x}Te nanocrystals of various shapes

To understand the weak shape dependence of the optical spectra, as observed for Cu_{2-x}Te NCs, a thorough investigation of the shape dependent optical properties will be presented in the following chapter. This is supported by a direct comparison with theoretical modeling based on the discrete dipole approximation (DDA).[39] Particularly, the extinction spectra of a Cu_{2-x}Te sphere, a nanorod and a tetrapod were modeled by using different dielectric functions, namely an empirical dielectric function of bulk Cu_{2-x}Te ,[152] the Drude dielectric function, and a dielectric function based on the Lorentz model. The so obtained extinction cross sections are summarized in Figure VI-2(I), (II), and (III), respectively. The input morphologies for all modeling results are displayed as insets to Figure VI-2(I) and were determined from TEM micrographs. These are a 9 nm sphere (Figure VI-2a), a rod of 5 nm in width, 21 nm in length with a tip radius set to 2 nm (Figure VI-2b), and a tetrapod of 5 nm in width and 12 nm arm length (Figure VI-2c).[39]

In the first part of the following chapter the extinction cross sections for the different shapes as calculated with the empirical dielectric function will be discussed. The results of the modeling are shown in Figure VI-2(I). A comparison of the experimental and modeled data reveals a qualitative representation of the measured spectra (as shown in Figure VI-1) in all three cases, while a mismatch of the plasmon resonances between the calculated and measured spectra of approximately 100 nm is found. In particular, the calculated spectra are blue-shifted with respect to the experimental ones, namely 943 nm vs. 1074 nm for the spheres; 983 nm vs. 1069 nm for the rods; and 1007 nm vs. 1103 nm for the tetrapods. In any way, the observed mismatch can be explained as inherent in the empirical dielectric function and does not influence the main conclusion drawn from this investigation.[39] The Cu_{2-x}Te dielectric function, as given by Farag *et al.* is an average over multiple film thicknesses, while their reflectivity and transmission measurements indicate a film thickness-dependent behavior.[152] The use of a thickness-averaged dielectric function might lead to the observed discrepancies. Further, the thin film XRD data does not allow the assignment of Cu_{2-x}Te thin films to an exact crystal structure. A deviation from the weissite structure of our NCs might come along with a discrepancy in the copper deficiency (as discussed in chapter V) and with

this to an altered dielectric function.[152] The shoulder in the modeled spectrum of the sphere on the blue side of the NIR band is assigned to an artifact from the empirical input data.

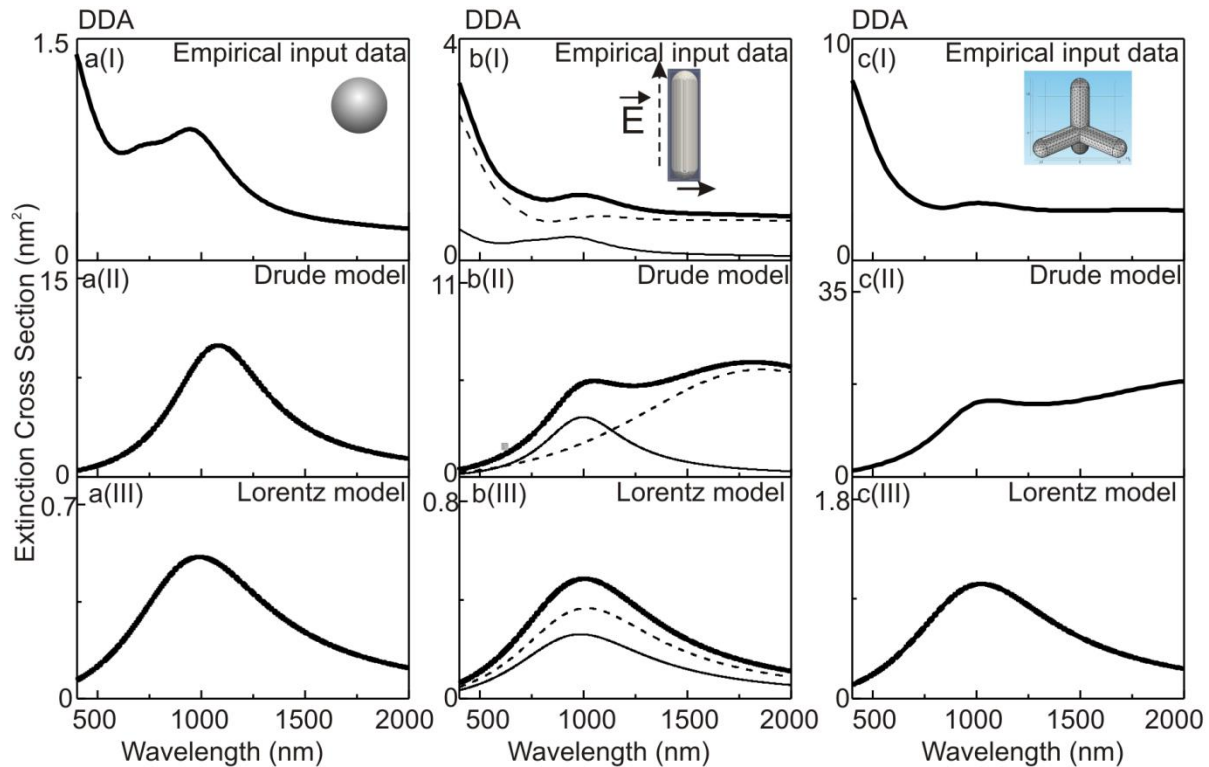


Figure VI-2 (I), (II), and (III) are DDA calculations using: (I) the empirical dielectric function of Cu_{2-x}Te [152] showing the modeling results for a Cu_{2-x}Te (a) sphere ($d = 9 \text{ nm}$, $\lambda_{\text{max}} = 943 \text{ nm}$), (b) nanorod (length \times width, $L \times W = 21 \times 5 \text{ nm}$, $\lambda_{\text{max}} = 983 \text{ nm}$), and (c) tetrapod ($L \times W = 12 \times 5 \text{ nm}$, $\lambda_{\text{max}} = 1007 \text{ nm}$); (II) the Drude model showing the modeling results for the same (a) sphere ($\lambda_{\text{max}} = 1090 \text{ nm}$), (b) nanorod ($\lambda_{\text{max}} = 1050 \text{ nm}$ and 1284 nm), and (c) tetrapod ($\lambda_{\text{max}} = 1068 \text{ nm}$); and (III) the Lorentz model showing the modeling results for the same (a) sphere ($\lambda_{\text{max}} = 990 \text{ nm}$), (b) nanorod ($\lambda_{\text{max}} = 1003 \text{ nm}$), and (c) tetrapod ($\lambda_{\text{max}} = 1022 \text{ nm}$). In b(I), b(II) and b(III) the black thin solid curves represent the T-bands; the dashed thin curves, the L-bands; and the black thick solid curves represent the averaged extinction cross section of the nanorods. All experimental spectra were measured in tetrachlorethylene as solvent, and thus, a dielectric constant of 1.505 was used for the surrounding medium in the simulations.[39]

Staying with the modeling results obtained from the empirical dielectric function, in the following the data for the rod shaped particles will be discussed (Figure VI-2b(I)). By exciting the collective oscillations along the axis of the nanorod (in the following termed as the longitudinal or L-band) and perpendicular to it (transverse or T-band) separately allows for a decomposition of the plasmon band into its contributions (Figure VI-2b(I), thin dashed line and thin solid line, respectively). The polarization of the incoming electric field is

illustrated by the arrows next to the rod sketch in Figure VI-2b(I). The T-band has its maximum at ~932 nm and approaches zero to the NIR. It resembles the spectrum of the spherical particles. The L-band peaks at ~1073 nm and has an extended absorption to the NIR. A good representation of a nanorod measurement in solution (as in Figure VI-1b) is theoretically given by averaging over all possible excitation directions. This calculation is represented as thick black curve in Figure VI-2b. Notably, the plasmon resonance in the averaged spectrum is composed of both, the T- and the L-band. Their resonances are energetically very close and can, thus, not be distinguished in the ensemble measurement. This is an unusual finding, with respect to strongly plasmonic material of noble metals such as gold, where two distinct bands characterize the extinction spectrum corresponding to the L- and the T-band (compare chapter II.2). The residual absorption in the NIR is purely constituted from the L-band.

This strong influence of the L-band on the red part of the rod shaped spectrum is further illustrated from size dependent calculations as given in Figure VI-3.[39] As a result from the variation of the AR (by increasing the length of the rod while keeping the width and tip radius constant), the T-band position remains constant, while the L-band red-shifts with increasing AR (Figure VI-3), a finding in agreement with plasmonic nanorods such as gold. However, these calculations further underline the strong contribution of the L-band to the broad NIR absorption, which is getting more pronounced with increasing nanorods length. Experimentally, a similar behavior has been found. The investigation of higher AR rods (AR = 9.6) show a more pronounced absorption in the NIR with respect to the previously investigated rods (AR = 4.1).[39] For details the reader is referred to the appendix A.7. These latter results indicate that plasmon damping gains importance the lower aspect ratio gets, *i.e.*, the more the nanorods approach the spherical case.

Taken together the modeling results obtained with the empirical dielectric function [152] demonstrate that the T- and L-band are very close in energy in the Cu_{2-x}Te nanorods and contribute both to the plasmon resonance in the averaged spectrum. This finding stands in stark contradiction to strongly plasmonic material such as gold, where two distinct bands due to the excitation along (L-band) and perpendicular to the long axis of the nanorods (T-band) are found. The theoretical modeling with the empirical dielectric function further revealed that the broad absorption observed in the NIR is solely due to the excitation along the long axis of the plasmon resonance (L-band). Finally, the weak shape dependence, as observed in the

experimental spectra is represented in the modeling with the empirical dielectric function.[39,152]

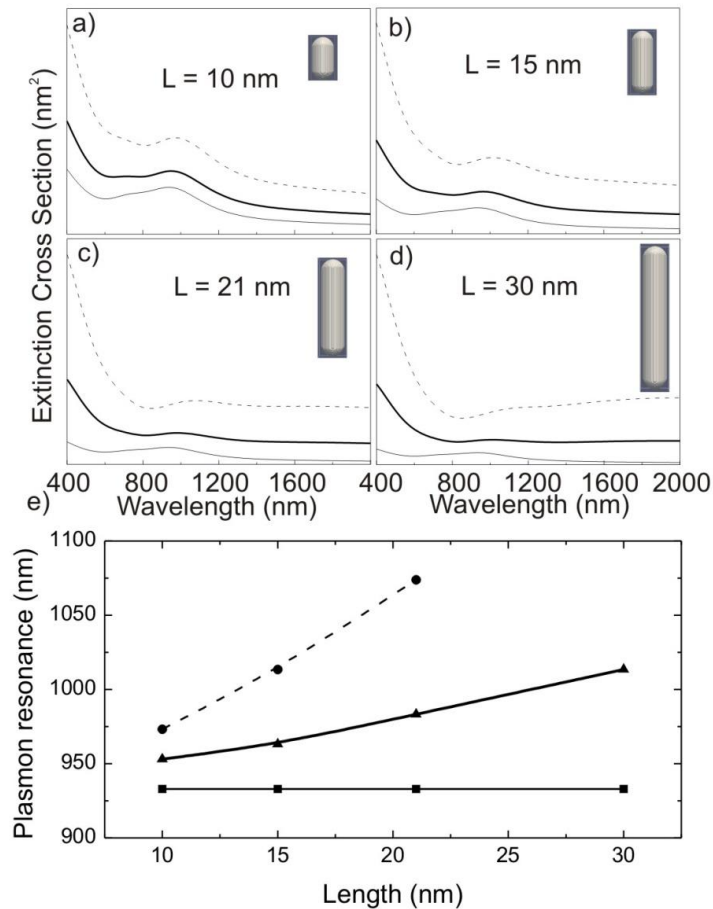


Figure VI-3 (a-d) DDA modeling results of Cu_{2-x}Te nanorods of varying size using the empirical dielectric function as input data:[152] L-band (black dashed curves) and T-band black solid curves together with the averaged extinction cross section (black thick curve) for nanorods with 10, 21, 15, and 30 nm total length, while keeping width (5 nm) and tip radius (2 nm) constant. e) Shift of the extinction maximum with nanorod length for the L-band (black dashed curves), T-band (black solid curves) and the averaged extinction cross section (black thick curve).

Plasmonic nanostructures can be modeled using the Mie theory and the Drude model to describe the optical properties. Thus, to understand the findings given in the previous paragraph and to gain further insight on the nature of the NIR optical resonances in Cu_{2-x}Te NCs, the extinction spectra for all three NC shapes were modeled with the Drude dielectric function (compare formula (II-20)). This has been determined by fitting the Mie resonance, according to equation (II-26) to the experimentally observed optical spectra of a sphere of 9 nm diameter. The best fitting Drude function is obtained with the fitting parameters

$\gamma = 0.6 \text{ eV}$, $\epsilon_{\text{Cu}_{2-x}\text{Te},\infty} = 8.4$, and $\omega_p = 4.1 \text{ eV}$. The same parameters have been used to simulate the Cu_{2-x}Te nanorods and tetrapods.

In the following paragraphs the results obtained with the Drude dielectric function will be discussed and are displayed in Figure VI-2(II). The fit of the Mie resonance to the experimental extinction spectrum of the 9 nm Cu_{2-x}Te sphere is shown in Figure VI-2a(II). It demonstrates a similar asymmetry as observed in the experimental spectrum with a maximum peak position at 1090 nm with respect to 1074 nm for the experiment. While the plasmon resonance is accurately represented, the interband transitions are not included in the Drude theory (compare chapter II.2). The calculated average extinction spectrum of the nanorod is shown as thick black curve in Figure VI-2b(II). The contribution of the transverse and longitudinal absorption (T- and L- band) is given as thin solid and dashed curves, respectively. In the averaged extinction spectrum two broad but distinct bands are observed, with the low energy band being more intense. While the high energy plasmon resonance (T-band) calculated with the Drude model qualitatively fits the empirical data, the L-band is strongly overstated. Similar results are also found for Cu_{2-x}Te tetrapods, where the Drude approach overestimates the NIR region (Figure VI-2c(II)).[39]

Notably, a better representation of the experimental results and the modeling with the empirical dielectric function is obtained when modifying artificially the Drude model. Hereby an additional damping term that only acts on the long wavelength region ($> 1000 \text{ nm}$) is included into the Drude model. This is given as follows:

$$\epsilon_{\text{Cu}_{2-x}\text{Te},\text{Drude-Damped}} = \epsilon_{\text{Cu}_{2-x}\text{Te},\infty} - \frac{\omega_p^2}{\omega(\omega + i\gamma_{pl}(\omega))} \quad (\text{VI-1})$$

with

$$\gamma_{pl}(\omega) = 0.6 \text{ eV} + 1.2 \text{ eV} \frac{\lambda^4}{\lambda^4 + \lambda_0^4} \quad (\text{VI-2})$$

and $\lambda_0 = 1000 \text{ nm}$. The outcome of this approach is given in Figure VI-4a. The green curve indicates the averaged extinction, while dark and light grey show the contribution of the T- and the L-band, respectively. As a result of the additional damping, both bands come close in energy resulting in a contribution of both to the plasmon resonance in the averaged spectrum. Further, upon the additional damping the L-band broadens, resulting in a broad residual absorption in the NIR (green curve).

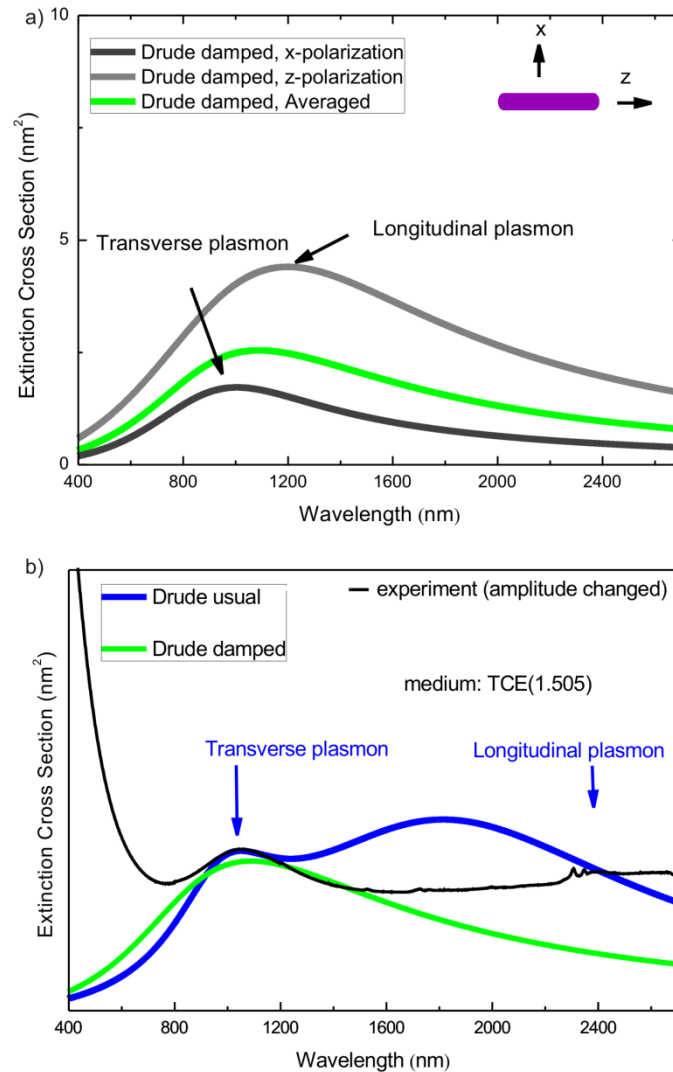


Figure VI-4 (a) Calculated (DDA) extinction spectrum of a Cu_{2-x}Te nanorod (21×5 nm, 2 nm tip radius) in TCE after using an artificially-damped Drude-like dielectric function. The longitudinal and transverse plasmon bands are given in grey and black curves, respectively; and the averaged extinction spectrum in light green. (b) In order to facilitate comparison, the experimental spectrum (black curve) together with the damped (light green curve) and usual Drude model (blue curve) is included.[39]

The findings obtained from the modified Drude approach are consistent with the results obtained when using the empirical dielectric function (as discussed above, Figure VI-2b(II)) and suggest that the Drude model with additional damping better describes the experimental results. While the usual Drude overstates the NIR absorption and results in two pronounced bands (Figure VI-4b, blue curve), the Drude model with the additional damping (Figure VI-4b, green curve) demonstrates a qualitatively better agreement with the experimental results (Figure VI-4b, black curve). This suggests that the nanorods experience a significant damping for oscillations above 1000 nm.[39]

As a third approach the extinction spectra of the three different shapes have been simulated by using the Lorentz model, which treats the carriers as localized oscillators with a frequency Ω_L . The Lorentz dielectric function is described as follows:

$$\varepsilon_{\text{Cu}_{2-x}\text{Te,Lorentz}} = \varepsilon_{\text{Cu}_{2-x}\text{Te},\infty} - \frac{\Delta\varepsilon \cdot \Omega_L^2}{(\omega^2 - \Omega_L^2) + i\omega\Gamma_L} \quad (\text{VI-3})$$

Similar to the Drude model, also the Lorentz dielectric function has been fitted to the experimental spectrum of the 9 nm Cu_{2-x}Te spheres. The best fitting parameters are $\varepsilon_{\text{Cu}_{2-x}\text{Te},\infty} = 8.4$, $\Delta\varepsilon = 1$, $\Gamma_L = 1$ eV, and $\Omega_L = 1.2$ eV. These were also used to model the extinction spectra of the rods and tetrapods. In Figure VI-2 (panel III) the extinction spectra as obtained with the Lorentz dielectric function for all three shapes are given. The three spectra are dominated by a broad band at ~ 990 nm for the sphere, 1003 nm for the rod and 1020 nm for the tetrapod and have a very similar shape. T- and L- band in the rod shaped spectrum (Figure VI-2b(III), thin solid and thin dashed line, respectively) are very close in energy (T-band: 985 nm, L-band: 1015 nm), and both contribute to the resonance band in the averaged spectrum (Figure VI-2b(III), thick solid line). These findings are consistent with the results from the empirical dielectric function. Further, the results from the Lorentz modeling represent the weak shape dependence as observed in the experiment. Nevertheless, the region of the broad extinction above 1200 nm, as seen in the experimental spectra of the elongated structures is not represented with the Lorentz model.[39]

The results obtained with the Drude, the Drude damped, and the Lorentz model are interpreted in the following way: With the standard Drude model the set of data for all three NC shapes cannot be described properly. Mainly, for the elongated structures, the region above 1200 nm is overstated by the Drude model, resulting in a broad peak ascribed to the L-band. This in contrast is not observed in the experimental spectrum. Nevertheless, a strong L-band is indicative and very characteristic for Drude-like free carriers, as they are present for instance in gold (compare chapter II.2). The introduction of an artificial damping term into the Drude model at longer wavelength allows the suppression of the L-band in the calculated spectra, leading to an overall better agreement with the experiment. This suggests a strong damping of the holes in the elongated structures. Further, the weak shape dependence of the experimental extinction spectra is better described by the Lorentz model of localized quantum oscillators, which is understood by the fact that the Lorentz model assumes localized carriers.

The electric fields induced by such carriers are not strong, thus, the extinction depends only weakly on the NC's shape. This indicates an essential degree of localization of the holes in those NCs. Nevertheless, this model does not sufficiently describe the increased extinction above ~ 1200 nm.[39]

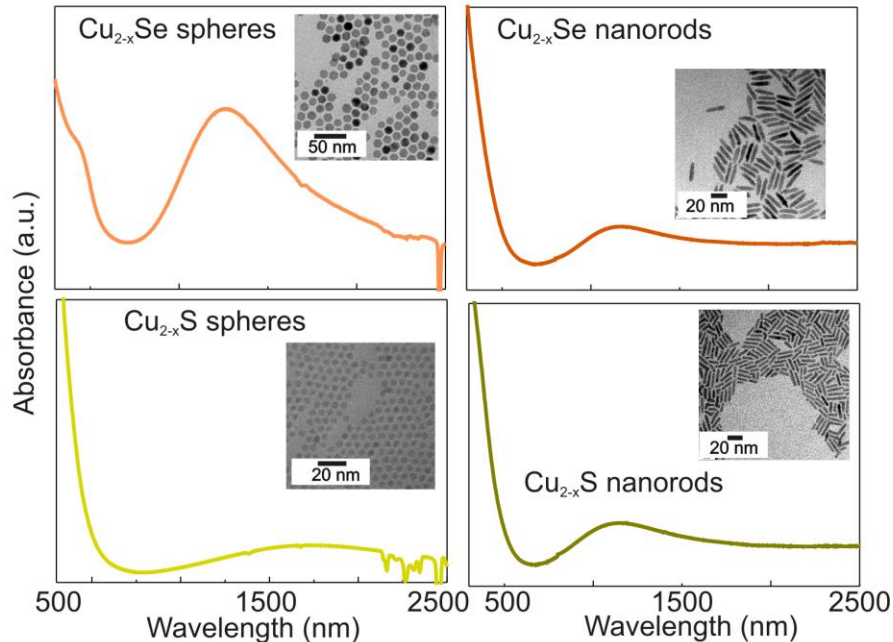


Figure VI-5 Extinction spectra of Cu_{2-x}Se spheres and nanorods (orange curves); and Cu_{2-x}S spheres and nanorods (dark yellow curves). The spectra of the nanorods in both cases show similar extinction spectra as the Cu_{2-x}Te nanorods with a plasmon resonance at 1182 nm (Cu_{2-x}Se) and 1128 nm (Cu_{2-x}S nanorods) and a broad residual extinction to the NIR, interpreted as a result from a significant damping of the L-band. Further, a very weak shape dependence is observed. Note that both spheres, Cu_{2-x}Se and Cu_{2-x}S , were prepared via one-pot synthesis, while Cu_{2-x}Se and Cu_{2-x}S nanorods were obtained by $\text{Cd}^{2+}/\text{Cu}^+$ from pre-formed CdSe/S nanorods, in analogy to the Cu_{2-x}Te NCs presented throughout the manuscript.[39]

The conclusions drawn so far are based on results obtained from Cu_{2-x}Te NCs. Nevertheless, similar properties are expected for the entire family of copper chalcogenides. In Figure VI-5 the experimental extinction spectra of Cu_{2-x}S and Cu_{2-x}Se nanospheres and nanorods are shown. All spectra are dominated by an increasing absorption to the blue, due to the interband transitions, and plasmon resonances further in the NIR. The elongated nanorods show a broad extinction farther in the red, very similar to the extinction spectra of the rod shaped Cu_{2-x}Te NCs and interpreted as a result from significant damping. Further, a similar weak shape dependence as demonstrated for Cu_{2-x}Te NCs is observed. This suggests again an essential

degree of localization of the holes in those NCs and, thus, that the Lorentz-type behavior of holes is a general property of copper chalcogenide NCs.[39]

Localization of carriers in bulk semiconductors with disorder has undergone an intensive study in the past. It has been shown that disordered bulk semiconductors can exhibit a so-called mobility edge.[153] Electron states below the mobility-edge energy in the conduction band of n-type semiconductors are localized, *i.e.*, all hole states above the mobility edge in the valence band of a p-type semiconductor. With the Fermi energy close to the mobility edge an essential part of the carriers in a semiconductor is expected to be localized.[153] The measured plasmonic responses of copper chalcogenide NCs, demonstrating weak shape dependence, are believed to show an essential degree of localization, too. Thus, the concepts of bulk disordered semiconductors might also be applicable to nanostructures provided that the localization length of the carrier is shorter than the size of the nanostructure. The given results suggest that the Drude-like picture does not describe the experimental observations adequately and is not sufficient to understand the optical response of Cu_{2-x}Te and similar NCs. Further investigations in this direction are needed.[39]

VI.3 Shape dependent near-field properties of Cu_{2-x}Te nanocrystals

For the investigation of the near-field properties of Cu_{2-x}Te NCs of the three different shapes we come back to the empirical dielectric function, as discussed at the beginning of this chapter. In Figure VI-6 the near-field enhancement (NFE) maps for all three shapes investigated are given.

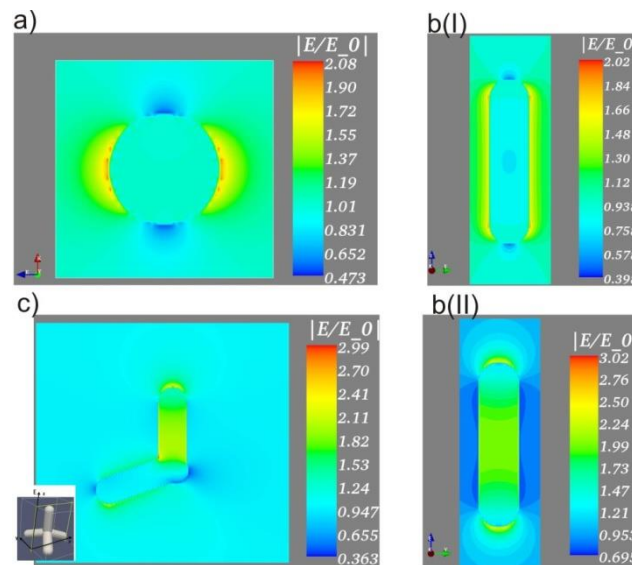


Figure VI-6 Near-field enhancement maps for (a) a Cu_{2-x}Te sphere ($d = 9 \text{ nm}$) excited at $\lambda_{\text{max}} = 943 \text{ nm}$, (b) a nanorod (length \times width, $L \times W = 21 \times 5 \text{ nm}$) excited at $\lambda_{\text{max}} = 933 \text{ nm}$ for the T-band (I), and $\lambda_{\text{max}} = 1074 \text{ nm}$ for the L-band (II), and (c) a tetrapod ($L \times W = 12 \times 5 \text{ nm}$) excited at $\lambda_{\text{max}} = 1007 \text{ nm}$. The excitation wavelengths are chosen according to their respective resonance frequencies as determined from Figure VI-2(I).[39]

The Cu_{2-x}Te sphere (Figure VI-6a) has been excited at its resonance wavelength (943 nm) and confirms the dipolar character that has been assumed when fitting the Mie resonance in the dipolar approximation. The NFE maps of the nanorods show a dipolar pattern across the nanorod axis when excited at 933 nm, corresponding to the maximum of the T-band, and a dipolar near field pattern along the nanorod axis when excited at 1074 nm (L-band, Figure VI-6b(I) and (II), respectively). The NFE map of the $12 \times 5 \text{ nm}$ tetrapod (excitation at 1007 nm), shows a dipole in the plane of excitation mainly located at the tip of the excited arm with part of it scattered into another arm (Figure VI-6c). In all three morphologies the NFE factors for Cu_{2-x}Te NCs are very low with enhancements for the sphere and T-band in the rod of around 2, and the L-band and tetrapod of ~ 3 . The L-band in the nanorods shows a

30 times lower NFE with respect to plasmonic nanorods of the same dimensions (refer to chapter II.2). This can be explained by a ca. 100× lower carrier density for Cu_{2-x}Te . [26] However, carrier localization is envisaged to have an essential influence also on the near field properties and to be responsible for the low NFE factors. [39]

VI.4 Chapter summary

In this chapter, a straightforward strategy for the synthesis of Cu_{2-x}Te NCs of well-defined morphologies (spheres, rods and tetrapods) *via* cation exchange with Cu^+ from pre-formed CdTe NCs has been presented. This allowed for the first time the synthesis of plasmonic material of unusual shapes, such as tetrapods. As this process occurs along with morphology preservation any other shape is envisaged to be conceivable. In all synthesized Cu_{2-x}Te NCs pronounced plasmon bands in the NIR are found. A weak shape dependence of the plasmon resonances has been observed, which is an unusual finding for plasmonic material. [39] DDA modeling with the standard Drude model, does not appropriately describe all three morphologies investigated herein. In particular the L-band in the elongated structures is overstated. The modeling with an empirical dielectric function shows a qualitative good agreement with the experimental results and demonstrates that the transverse and longitudinal bands in the rods overlap in energy. [39] Similar results are obtained when an artificial damping term is introduced in the Drude model, suggesting that the carrier oscillations in the rods experience a significant damping above ca. 1000 nm. Further, the weak shape dependence obtained when using the Lorentz model indicates that carriers in the valence band of Cu_{2-x}Te experience partial localization. This is regarded as a common property for the entire copper chalcogenide family. [39] In conclusion, these results demonstrate a route for the preparation of Cu_{2-x}Te NCs of well-defined morphologies. Combined with thorough theoretical investigations, a deeper insight and a clearer picture of the influencing factors on the optical resonance in copper chalcogenide NCs are provided.

VII. Conclusions and outlook

Within this work extensive experimental evidence has been given to unambiguously identify the plasmonic nature of vacancy doped copper chalcogenide NCs. It has been shown that heavy vacancy doping, with carrier densities of $\sim 10^{21} \text{ cm}^{-3}$, leads to intense localized surface plasmon resonances (LSPRs) in the near infrared (NIR). The chemical control over the degree of doping allows a reversible tuning of those plasmon resonances and highlights this material system over conventional plasmonic material. While typical plasmonic characteristics of the LSPR in copper chalcogenide NCs have been confirmed within this work, a deviation from the usual Drude model was found. Further, the weak shape dependence of the plasmon resonances in vacancy doped copper chalcogenide NCs indicates an essential degree of localization of the carriers.

The decisive assignment of the NIR resonances in copper chalcogenide NCs to LSPRs has been given by probing typical plasmonic characteristics. The refractive index sensitivity of the LSPR, for example, is a characteristic of plasmonic material.[25] In copper chalcogenide NCs this sensitivity has been demonstrated by transferring Cu_{2-x}S and Cu_{2-x}Se NCs into different media.[34] The observed red-shift with increasing refractive index of the solvent is indicative for an LSPR.[25] Moreover, through shape dependent investigations, the intrinsic size effect of the LSPR in Cu_{2-x}S NCs below ~ 4.5 nm has been demonstrated.[34,44] Detected as a red-shifted and broadened resonance with decreasing NC size, the well established effect of surface scattering is represented.[62,63] LSPRs show very characteristic dynamics on an ultrashort time scale; these can be detected with femtosecond pump-probe spectroscopy.[73,74] While probing the NIR resonance in copper chalcogenide NCs, typical plasmon dynamics have been identified. The observed initial rise is indicative for the carrier thermalization after excitation with an intense laser pulse. The following two step decay is assigned to elevated temperatures of the carrier gas (first decay) and the lattice (second decay) that relax via carrier-phonon and phonon-phonon scattering, respectively. [34,73,74] At last,

interparticle plasmon coupling has been demonstrated in extremely monodisperse Cu_{2-x}S NCs. Notably, this has been observed in highly ordered, self-assembled superlattice arrays, demonstrating a red-shifted LSPR with respect to the non coupling particles.[39] While plasmon coupling is a well-studied phenomenon,[140] it has been shown for the first time in this work for plasmonic copper chalcogenide NCs. The exceptionally high degree of shape control, as given in vacancy doped semiconductor NCs, turns out to be extremely advantageous, as self-assembly delivers an effective route for the investigation of interparticle plasmon coupling. Taken together the results presented above demonstrate key attributes typical for plasmonic material and clearly identify LSPRs in copper chalcogenide NCs.

The extraordinary characteristic to hold highly tunable LSPRs and excitons in one material highlight copper chalcogenide NCs over conventional plasmonic nanostructures. It is the control over heavy vacancy doping within the chemical structure that delivers access to these attractive features.[34] As demonstrated within this study, the un-doped copper chalcogenide NCs show purely excitonic properties, while upon vacancy doping the LSPR dominates. Triggered by the controlled oxidation or reduction, the vacancy density in the structure is tailored, allowing a full recovery of the initial optical properties. This delivers the opportunity to reversibly tune the LSPR over a wide range of frequencies from 1000 up to 2000 nm and illustrates a key characteristic of copper chalcogenide NCs.[34] An influence of the LSPR formation on the excitonic properties has been uncovered. A loss in oscillator strength of the excitonic transition, a quenching of PL, and an ultrafast component dominating the PL lifetime might be explained by an Auger type recombination due to the high charge carrier density in the NCs. However, a partial influence of the energy transfer from the exciton to the plasmon is also conceivable, emphasizing copper chalcogenide NCs as a material system for the investigation of exciton plasmon interactions.[34] An exact evaluation of the observed processes would require probing both, the excitonic and plasmonic properties separately, by means of time resolved spectroscopy. Structurally the controlled tailoring of the copper vacancy density has been shown to come along with a concomitant change in the crystal phase from the copper deficient to the un-doped phases and vice versa.[34] This control over the copper vacancy formation delivers the exceptional opportunity to reversibly tune the excitonic and the plasmonic properties in vacancy doped copper chalcogenide NCs.

A detailed theoretical study on the shape dependent optical properties of copper chalcogenide NCs, in particular Cu_{2-x}Te , suggests that the carriers, responsible for the formation of the NIR resonance, cannot be treated as fully free.[39] This conclusion has been drawn by comparing experimental with theoretical results based on the DDA. In particular, the Drude model fails

to represent the entire set of shapes investigated (spheres, rods, and tetrapods) herein. To be more precise, it overstates the longitudinal plasmon resonance in the elongated structures, a feature that, indeed, is not observed in the experiment.[39] A strong L-band, however, is indicative for Drude-like free carriers.[62] Remarkably, the Drude model with an artificial damping term acting on the long wavelength region only leads to a better description of the experiment. This suggests that the carriers in the elongated structure experience additional damping.[39] Moreover, the weak shape dependence as observed in the experimental spectra is unusual for plasmonic material and is better represented by the Lorentz model. This is understood, as the Lorentz model assumes localized carriers, which induce only weak electric fields and thereby result in a weak shape dependence of the extinction band. This indicates that the carriers in copper chalcogenide NCs experience partial localization. These conclusions were drawn for the entire family of copper chalcogenide NCs, and may also be responsible for the lower near-field enhancement (NFE) factors in the anisotropic particles with respect to gold.[39] Considering that the ionic crystal lattices of copper chalcogenide NCs is governed by anisotropic effects, the need for anisotropy dependent investigations of the plasmon resonance is required to understand the observed experimental results.[40,103] Finally, the straightforward strategy for the synthesis of Cu_{2-x}Te NCs of well-defined morphologies *via* ion exchange, demonstrated the synthesis of unusual plasmonic shapes, such as tetrapods, that have not been feasible to produce so far.[39]

The unique structure dependent optical characteristics of copper chalcogenide NCs were uncovered within this work, opening the route toward their application in plasmonics related fields. One can envisage the use of copper chalcogenide NCs in photothermal therapy, benefiting from their tunable NIR plasmon resonances. The exact tailoring allows to cover the optimum window for this application, *i.e.*, in the range of frequencies, where a high transparency of tissue, blood, and water is found.[27] Further, copper chalcogenide NCs provide the optimum size to prevent excretion by the body, while still exhibiting LSPRs in the NIR.[21] Indeed, Cu_{2-x}Se NCs have already been successfully implemented for use in photothermal therapy.[21] Another particularly interesting application is the use of plasmonic copper chalcogenide NCs in surface enhanced Raman spectroscopy (SERS). Despite the comparably low NFE factors of copper chalcogenide NCs, the precise shape control as demonstrated in this study might allow the defined tailoring of hotspots, making them interesting candidates as SERS substrates.[22,59] Further, the ability of copper chalcogenide NCs to exhibit excitons and plasmons within one structure might deliver a material system that forms the basis for the investigation of exciton plasmon interaction. However, the high

tendency of oxygen induced plasmon formation and exciton quenching as presented within this study has to be taken into account for the prospective use of Cu_{2-x}S NCs as absorbers in photovoltaic applications.[92,93]

To conclude, the results presented in this work provide a clearer picture of the plasmonic properties of vacancy doped copper chalcogenide NCs, which are strongly correlated to their structural characteristics. This thorough investigation has benefited from the chemical synthesis techniques based on semiconductor nanoscience, which allows the production of precise shapes, compositions and highly monodisperse sizes, an advantage over conventional plasmonic material. The combination of optical spectroscopy and structural characterization with theoretical modeling provided a deep insight on the structure dependent plasmonic properties of vacancy doped copper chalcogenide NCs.

Appendix

A.1. Structural characterization of copper chalcogenide nanocrystals

The structural characterization of the copper deficient copper chalcogenide NCs (as discussed in chapter IV) will be given in the following. For XRD experiments typically 5 μL of a 20 mg/mL NC dispersion was drop casted onto a glass substrate which was pre-heated on a hot plate to allow the solvent to evaporate faster.

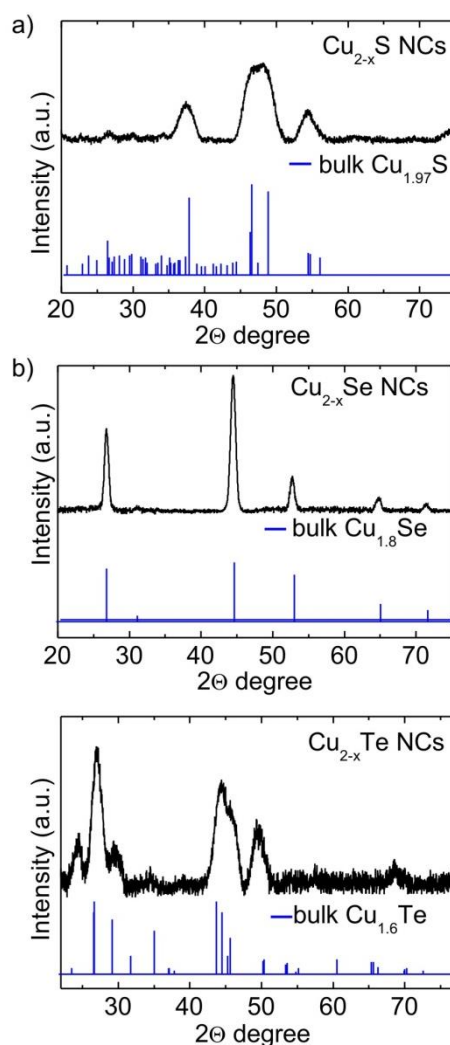


Figure A - 1 XRD data for copper deficient ($x > 0$) (a) Cu_{2-x}S NCs ($d = 5$ nm), (b) Cu_{2-x}Se NCs ($d = 12$ nm), and (c) Cu_{2-x}Te NCs ($a = 5$ nm) (black curves), together with the respective stick powder reference pattern (blue curves).

Figure A - 1 shows the XRD patterns for copper deficient ($x > 0$) (a) Cu_{2-x}S NCs ($d = 5$ nm), (b) Cu_{2-x}Se NCs ($d = 12$ nm), and (c) Cu_{2-x}Te NCs ($a = 5$ nm) (black curves) together with the

respective stick powder reference pattern (blue curves). Cu_{2-x}S NCs can be assigned to $\text{Cu}_{1.97}\text{S}$ with $x = 0.03$, Cu_{2-x}Se NCs to $\text{Cu}_{1.8}\text{Se}$ with $x = 0.2$ and Cu_{2-x}Te NCs to $\text{Cu}_{1.4}\text{Te}$ with $x = 0.6$.

A.2. Ligand induced disassembly of Cu_{2-x}S superlattices

The experimental details describing the ligand induced disassembly, as discussed in chapter IV.2, are given in the following. To induce the disassembly of the Cu_{2-x}S NCs typically 40 μL of OAm were added to a 2 mL dispersion of the superlattices in toluene. Bath sonication and mild heating (ca. 40 $^{\circ}\text{C}$) for several minutes resulted in stable colloidal dispersions of non close packed Cu_{2-x}S NCs. The addition of ligands in excess forces the disassembly of the NCs. The high concentration of ligands leads to a binding to the NCs surface and can be understood in terms of ligand exchange. This allows the stabilization of single NCs, in turn leading to their dispersion into the solution.

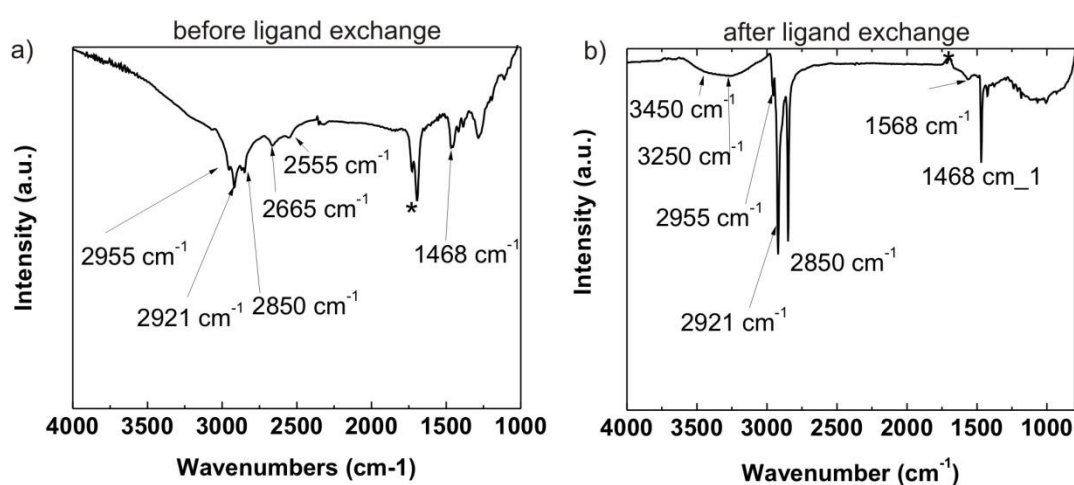


Figure A - 2 FTIR spectrum of Cu_{2-x}S NCs (a) before, and (b) after ligand exchange. (a) Typical resonances of the S-H vibration at 2555 and 2665 cm^{-1} , are replaced by (b) the vibration of NH_2 and N-H at 1568 cm^{-1} , and 3500 and 3300 cm^{-1} , respectively.[115]

The ligand exchange from DDT (after synthesis) to OAm (after redispersion) was confirmed by FTIR measurements. Figure A - 2a shows the FTIR spectrum of the as-synthesized Cu_{2-x}S NCs self-assembled into close packed superlattice arrays, with modes at 2555 and 2665 cm^{-1} characteristic of the S-H vibration.[115] This proves that DDT acts as a capping ligand during synthesis. This vibrational pattern is no longer present in the FTIR spectrum after the addition of OAm (Figure A - 2b) instead a $-\text{NH}_2$ scissoring mode at 1568 cm^{-1} and the antisymmetric and symmetric vibration modes of $-\text{N}-\text{H}$ are observed between 3500 and 3300 cm^{-1} .[115] These findings indicate a ligand exchange from DT to OAm occurs after the addition of an OAm excess. Taken together the results confirm that the addition of OAm in excess triggers NC disassembly due to ligand exchange from DDT and thereby stabilize the NCs in solution.

A.3. Fluorescence quantum yield

The fluorescence quantum yield (chapter V) was derived from equation (VII-1). The fluorescence quantum yield Φ^i of a compound i is determined relative to that of a standard s with known fluorescence quantum yield Φ^s . The fluorescence quantum yield Φ^i is given as:

$$\Phi^i = \Phi^s \frac{f_s(\lambda_{ex}) \int_{\lambda_{em}} PL_{\lambda}^i(\lambda_{em}) \frac{n_i^2}{n_s^2}}{f_i(\lambda_{ex}) \int_{\lambda_{em}} PL_{\lambda}^s(\lambda_{em}) \frac{n_i^2}{n_s^2}} \quad (\text{VII-1})$$

with $f_x(\lambda_{ex}) = 1 - 10^{-A_x(\lambda_{ex})}$ and $A_x(\lambda_{ex})$ the absorbance for $x = i, s$. The absorbance of Cu₂S NCs in toluene and the reference IR140 in ethanol was adjusted to be equal at the excitation wavelength ($\lambda_{ex} = 614$ nm, Figure A - 3). Then, fluorescence spectra of both solutions were measured. The fluorescence quantum yield has been corrected for the different solvent refractive indices (n).

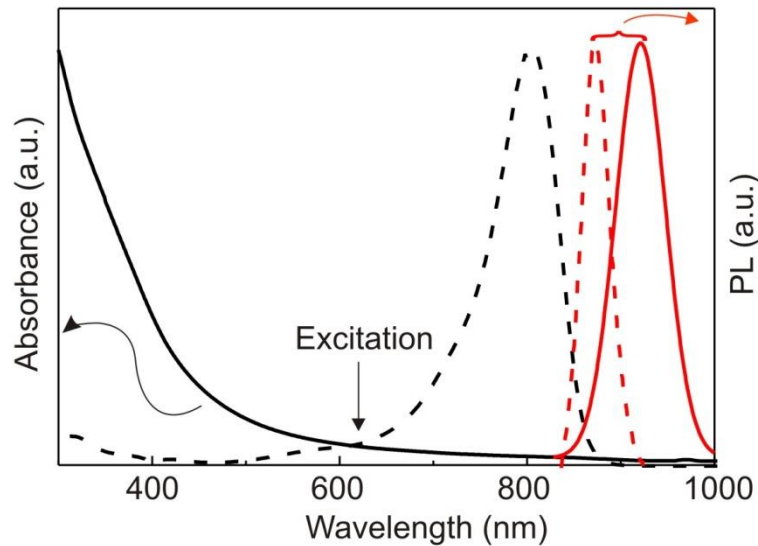


Figure A - 3 Extinction spectra of Cu₂S NCs ($x = 0$) in toluene (black solid line) together with the reference spectrum IR140 (black dashed line; not normalized) and PL spectra (red lines, respectively), normalized to the maximum.

A.4. Optical characterization of the as-prepared CdTe NCs for the use in ion exchange to Cu_{2-x}Te

The TEM images of the as-prepared CdTe NCs are depicted in the insets of Figure A - 4 (a-c) together with the corresponding absorption spectra. All absorption spectra show characteristic sharp features assigned to excitonic transitions in the quantum confined CdTe NCs.

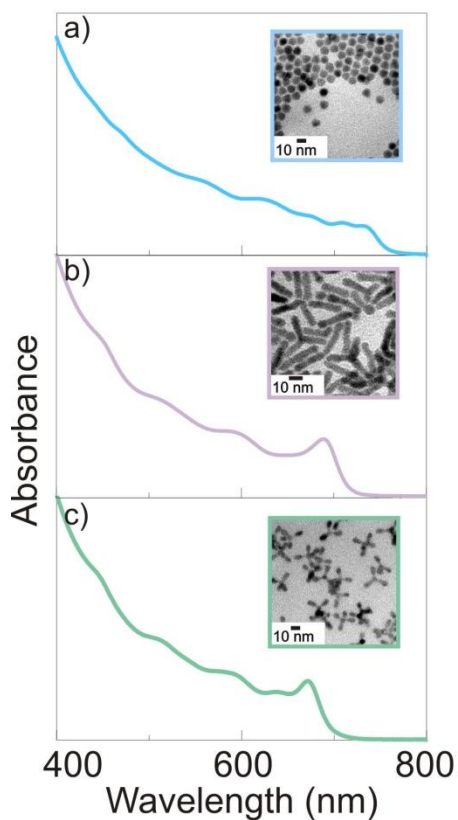


Figure A - 4 Absorption spectra of CdTe NCs (a) spheres, (b) rods, and (c) tetrapods together with representative TEM images.

A.5. Characterization of the ion exchange process

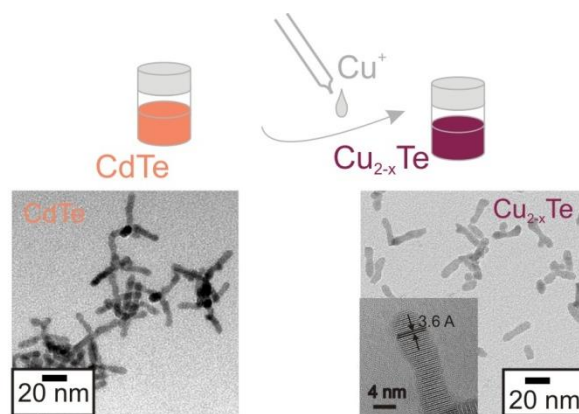


Figure A - 5 Representative TEM images of CdTe NCs before (left image) and after ion exchange (Cu_{2-x}Te , right image). The inset shows an HRTEM micrograph displaying the crystallinity of the Cu_{2-x}Te NCs after ion exchange.

The ion exchange process is sketched in Figure A - 5. TEM images of the NCs before and after ion exchange depict the shape preservation from CdTe to Cu_{2-x}Te NCs, with an HRTEM micrograph demonstrating the crystallinity of the ion exchanged Cu_{2-x}Te NCs (Figure A - 5). Figure A - 6a) and b) depict the optical characterization of the initial CdTe NCs dispersion (orange curves) and the ion exchanged Cu_{2-x}Te NCs solution (dark red curves). The absorption spectrum of a diluted solution of CdTe NCs is given in Figure A - 6a (orange curve). The inset shows a zoom into the region of the first excitonic peak. The excitonic peak at 720 nm demonstrates the quantum confinement of our NCs given by the width of the NCs, which is within the size of the exciton bohr radius of ~ 7.3 nm in bulk CdTe.[154] A typical absorption spectrum of the ion exchanged Cu_{2-x}Te NCs is given in Figure A - 6a (dark red curve). The excitonic feature, which is characterizing the spectrum of CdTe NCs is not present. The spectrum is dominated by a featureless profile in the visible with distinct NIR resonances. The photoluminescence of the CdTe NC sample as given in Figure A - 6b (orange curve) has its maximum at 740 nm ($\lambda_{\text{ex}} = 400$ nm). PL from Cu_{2-x}Te NCs is not detected after ion exchange (compare chapter V)

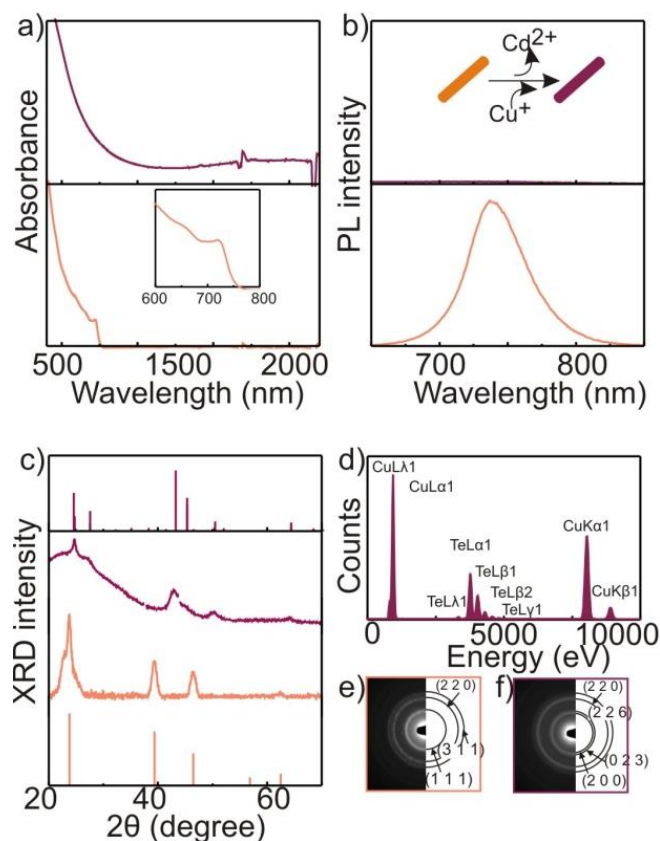


Figure A - 6 (a) Absorption, and (b) PL spectra of CdTe NCs (orange curves) and Cu_{2-x}Te NCs (dark red curves), (c) XRD, (d) EDX, (e) and (f) ED of the CdTe NCs before (orange curves) and after (dark red curves) ion exchange to Cu_{2-x}Te .

The ion exchange process was further confirmed by XRD analysis (Figure A - 6c). For the initial CdTe NCs zincblende structure has been confirmed via XRD showing the main peaks at 23.78, 39.33, 46.48, and 62.47 2θ angles corresponding to the lattice planes 111, 220, 311, and 331, respectively. The stick reference powder XRD pattern shown in Figure A - 6c, orange line, is that for bulk CdTe (JCPDS 85-237). The first three main peaks are also observed in the ED micrograph in Figure A - 6e and are indexed to the 111, 220 and 311 lattice planes. The crystal structure of the ion exchanged Cu_{2-x}Te NCs are indexed to the hexagonal weissite crystal structure (dark red line, Figure A - 6c). Dark red bars in Figure A - 6c indicate the reference powder pattern of bulk Cu_{2-x}Te with weissite crystal structure. The electron diffraction micrograph (Figure A - 6f) of the ion exchanged Cu_{2-x}Te NCs shows four distinct rings that are indexed to the 200, 023, 220, and 226 lattice planes of bulk weissite Cu_{2-x}Te . The results described above indicate a complete ion exchange from CdTe to Cu_{2-x}Te where the shape of the NCs is preserved and a complete ion exchange is expected. This has further been confirmed with EDX measurements on a single Cu_{2-x}Te NC. The results are given in Figure A - 6d and show that no Cd is present in the ion exchanged Cu_{2-x}Te NCs

suggesting a complete ion exchange from Cd^{2+} to Cu^+ . For Cu_{2-x}Te NCs of various shapes, the change from CdTe to Cu_{2-x}Te weissite crystal structure after ion exchange is demonstrated in all three shapes via XRD analysis as shown in Figure A - 7(a-c), together with the respective reference pattern.

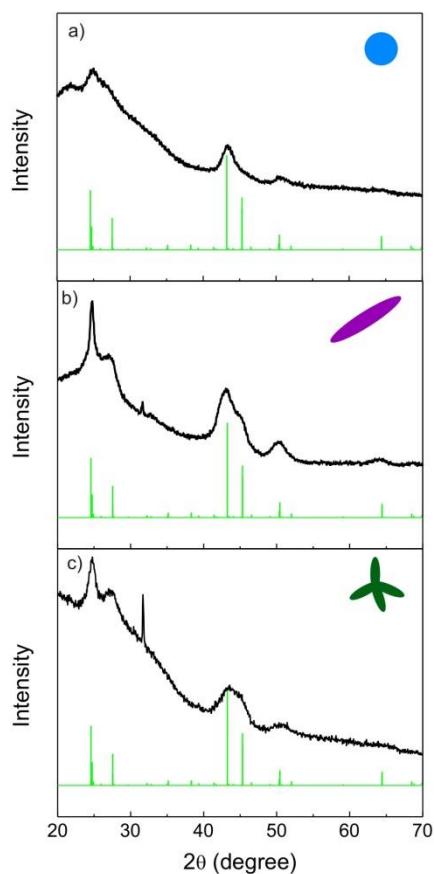


Figure A - 7 XRD pattern for (a) spheres, (b) rods, and (c) tetrapods confirming the transformation to Cu_{2-x}Te NCs with weissite crystal structure.

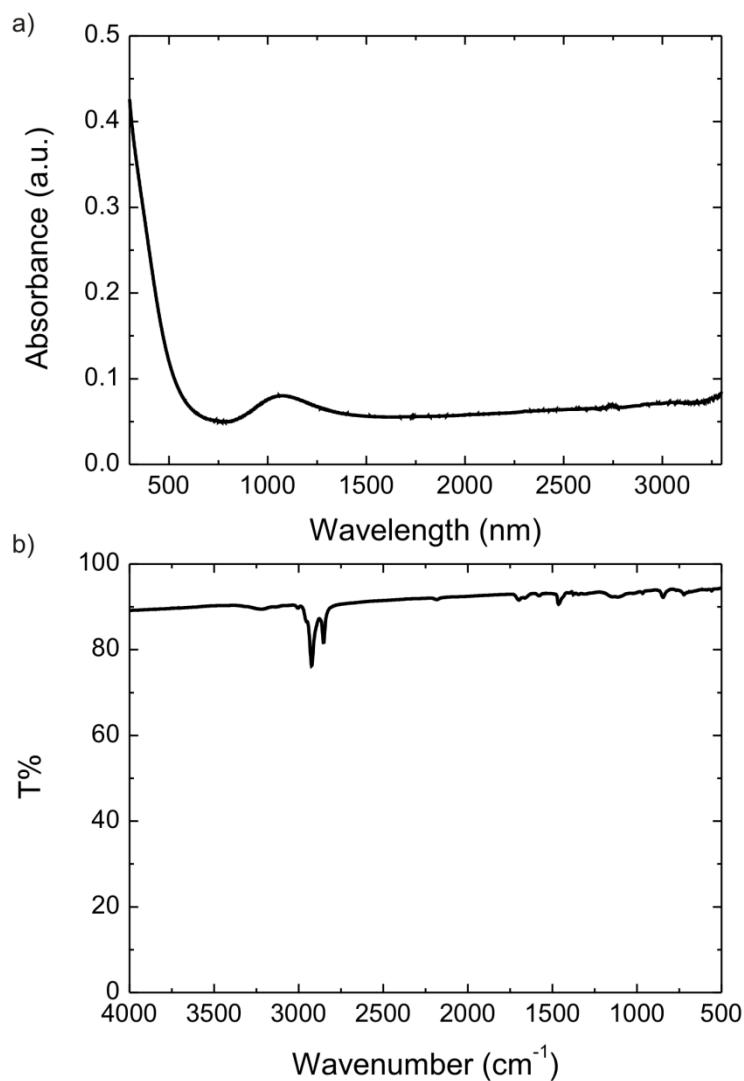
A.6. Extinction and FTIR spectra of Cu_{2-x}Te nanorods (21x5 nm).

Figure A - 8 a) Extinction and b) FTIR spectra of Cu_{2-x}Te nanorods (21x5 nm). The transmission in the infrared in the FTIR spectrum does not result in a pronounced absorption band. The broad background absorption represents the damping at longer wavelength. Sharper peaks in the FTIR spectra correspond to the organic ligands on the surface of the particles.

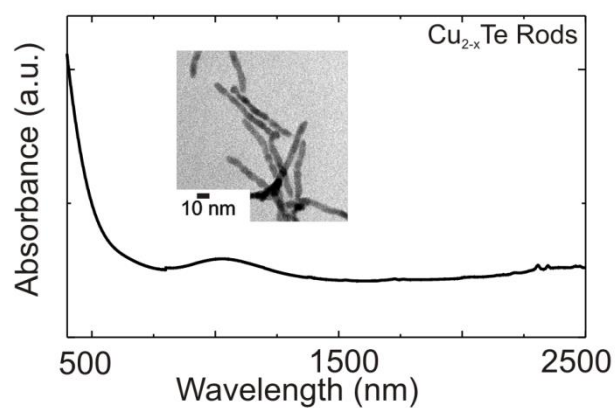
A.7. Extinction spectrum of high aspect ratio rods (9.6)

Figure A - 9 Extinction spectra of Cu_{2-x}Te NCs of 5.5x48 nm (Width x Length) with an AR of 9.6, together with a representative TEM image. Remarkably, the spectrum strongly resembles the one of lower AR (4.1) as given in the main text (Figure VI-1b in chapter VI.1).

Abbreviations

BEM	boundary element method
BZ	Brillouin zone
C_{abs}	absorption cross section
CB	conduction band
CdO	cadmium oxide
C_{ext}	extinction cross section
C_{sca}	scattering cross section
Cu_{2-x}S	copper sulfide
Cu_{2-x}Se	copper selenide
Cu_{2-x}Te	copper telluride
DDA	discrete dipole approximation
DDT	dodecanthiol
DDT	dodecanthiol
DIBAH	diisobutylaluminium hydride
ED	electron diffraction
EDX	energy dispersive X-ray analysis
E_{g}	bandgap
FTIR	fourier transform infrared spectroscopy
HRTEM	high resolution transmission electron microscopy
IR	infrared
L-band	longitudinal plasmon resonance
LSPR	localized surface plasmon resonance
NC	nanocrystal
NFE	near-field enhancement
NIR	near infrared

Abbreviation

OA	oleic acid
OAm	oleylamine
ODE	octadecene
PL	photoluminescence
PMMA	poly(methylmethacrylate)
PMT	photomultiplier tube
S	sulfur
SAED	small angle electron diffraction
Se	Selenium
SERS	surface enhanced Raman spectroscopy
T-band	transverse plasmon resonance
TBP	tributylphospine
TCE	tetrachloroethylene
TDPA	n-tetradecylphosphonic acid
Te	Tellurium
TEM	transmission electron microscopy
TOP	triocrylphosphine
TOPO	trioctylphosphine oxide
TTM	two temperature model
VB	valence band
XPS	X-ray photoelectron spectroscopy
XRD	X-ray diffraction

Bibliography

- 1 Alivisatos, A. P. Semiconductor Clusters, Nanocrystals, and Quantum Dots. *Science* **271**, 933-937, (1996).
- 2 Murray, C. B., Kagan, C. R., Bawendi, M. G. Synthesis and characterization of monodisperse nanocrystals and close-packed nanocrystal assemblies. *Annual Review of Materials Science* **30**, 545-610, (2000).
- 3 Efros, A. L., Rosen, M. The electronic structure of semiconductor nanocrystals. *Annual Review of Materials Science* **30**, 475-521, (2000).
- 4 Nozik, A. J. Quantum dot solar cells. *Physica E-Low-Dimensional Systems & Nanostructures* **14**, 115-120, (2002).
- 5 Link, S., El-Sayed, M. A. Optical properties and ultrafast dynamics of metallic nanocrystals. *Annual Review of Physical Chemistry* **54**, 331-366, (2003).
- 6 Talapin, D. V. LEGO Materials. *ACS Nano* **2**, 1097-1100, (2008).
- 7 Norris, D. J., Efros, A. L., Erwin, S. C. Doped Nanocrystals. *Science* **319**, 1776-1779, (2008).
- 8 Rogach, A. L. *Semiconductor Nanocrystal Quantum Dots*. (Springer-Verlag/Wien, 2008).
- 9 Hillhouse, H. W., Beard, M. C. Solar cells from colloidal nanocrystals: Fundamentals, materials, devices, and economics. *Current Opinion in Colloid & Interface Science* **14**, 245-259, (2009).
- 10 Rogach, A. L., Klar, T. A., Lupton, J. M., Meijerink, A., Feldmann, J. Energy transfer with semiconductor nanocrystals. *Journal of Materials Chemistry* **19**, (2009).
- 11 Zhao, Y., Burda, C. Development of plasmonic semiconductor nanomaterials with copper chalcogenides for a future with sustainable energy materials. *Energy & Environmental Science* **5**, 5564-5576, (2012).
- 12 Rivest, J. B., Jain, P. K. Cation Exchange on the Nanoscale: an Emerging Technique for New Material Synthesis, Device Fabrication, and Chemical Sensing. *Chemical Society Reviews* **42**, 89-96, (2013).
- 13 Burda, C., Chen, X., Narayanan, R., El-Sayed, M. A. Chemistry and Properties of Nanocrystals of Different Shapes. *Chemical Reviews* **105**, 1025-1102, (2005).
- 14 Peng, X., Manna, L., Yang, W., Wickham, J., Scher, E., Kadavanich, A., Alivisatos, A. P. Shape control of CdSe nanocrystals. *Nature* **404**, 59-61, (2000).

- 15 Manna, L., Milliron, D. J., Meisel, A., Scher, E. C., Alivisatos, A. P. Controlled Growth of Tetrapod-Branched Inorganic Nanocrystals. *Nature Materials* **2**, 382-385, (2003).
- 16 Deka, S., Miszta, K., Dorfs, D., Genovese, A., Bertoni, G., Manna, L. Octapod-Shaped Colloidal Nanocrystals of Cadmium Chalcogenides via "One-Pot" Cation Exchange and Seeded Growth. *Nano Letters* **10**, 3770-3776, (2010).
- 17 Pelaz, B., Jaber, S., de Aberasturi, D. J., Wulf, V., Aida, T., de la Fuente, J. M., Feldmann, J., Gaub, H. E., Josephson, L., Kagan, C. R., Kotov, N. A., Liz-Marzán, L. M., Mattoussi, H., Mulvaney, P., Murray, C. B., Rogach, A. L., Weiss, P. S., Willner, I., Parak, W. J. The State of Nanoparticle-Based Nanoscience and Biotechnology: Progress, Promises, and Challenges. *ACS Nano* **6**, 8468-8483, (2012).
- 18 Shirasaki, Y., Supran, G. J., Bawendi, M. G., Bulovic, V. Emergence of colloidal quantum-dot light-emitting technologies. *Nature Photonics* **7**, 13-23, (2013).
- 19 Kamat, P. V. Quantum Dot Solar Cells. Semiconductor Nanocrystals as Light Harvesters. *Journal of Physical Chemistry C* **112**, 18737-18753, (2008).
- 20 Li, S. Q., Guo, P., Zhang, L., Zhou, W., Odom, T. W., Seideman, T., Ketterson, J. B., Chang, R. P. H. Infrared Plasmonics with Indium–Tin-Oxide Nanorod Arrays. *ACS Nano* **5**, 9161-9170, (2011).
- 21 Hessel, C. M., P. Pattani, V., Rasch, M., Panthani, M. G., Koo, B., Tunnell, J. W., Korgel, B. A. Copper Selenide Nanocrystals for Photothermal Therapy. *Nano Letters* **11**, 2560-2566, (2011).
- 22 Dondapati, S. K., Sau, T. K., Hrelescu, C., Klar, T. A., Stefani, F. D., Feldmann, J. Label-free Biosensing Based on Single Gold Nanostars as Plasmonic Transducers. *ACS Nano* **4**, 6318-6322, (2010).
- 23 Huang, X., Jain, P., El-Sayed, I., El-Sayed, M. Plasmonic photothermal therapy (PPTT) using gold nanoparticles. *Lasers in Medical Science* **23**, 217-228, (2008).
- 24 Myroshnychenko, V., Rodriguez-Fernandez, J., Pastoriza-Santos, I., Funston, A. M., Novo, C., Mulvaney, P., Liz-Marzan, L. M., Garcia de Abajo, F. J. Modelling the optical response of gold nanoparticles. *Chemical Society Reviews* **37**, 1792-1805, (2008).
- 25 Underwood, S., Mulvaney, P. Effect of the Solution Refractive Index on the Color of Gold Colloids. *Langmuir* **10**, 3427-3430, (1994).

- 26 Luther, J. M., Jain, P. K., Ewers, T., Alivisatos, A. P. Localized Surface Plasmon Resonances Arising from Free Carriers in Doped Quantum Dots. *Nature Materials* **10**, 361-366, (2011).
- 27 Routzahn, A. L., White, S. L., Fong, L.-K., Jain, P. K. Plasmonics with Doped Quantum Dots. *Israel Journal of Chemistry* **52**, 983-991, (2012).
- 28 Rowe, D. J., Jeong, J. S., Mkhoyan, K. A., Kortshagen, U. R. Phosphorus-Doped Silicon Nanocrystals Exhibiting Mid-Infrared Localized Surface Plasmon Resonance. *Nano Letters* **13**, 1317-1322, (2013).
- 29 Garcia, G., Buonsanti, R., Runnerstrom, E. L., Mendelsberg, R. J., Llordes, A., Anders, A., Richardson, T. J., Milliron, D. J. Dynamically Modulating the Surface Plasmon Resonance of Doped Semiconductor Nanocrystals. *Nano Letters* **11**, 4415-4420, (2011).
- 30 Buonsanti, R., Llordes, A., Aloni, S., Helms, B. A., Milliron, D. J. Tunable Infrared Absorption and Visible Transparency of Colloidal Aluminum-Doped Zinc Oxide Nanocrystals. *Nano Letters* **11**, 4706-4710, (2011).
- 31 Manthiram, K., Alivisatos, A. P. Tunable Localized Surface Plasmon Resonances in Tungsten Oxide Nanocrystals. *Journal of the American Chemical Society* **134**, 3995-3998, (2012).
- 32 Dorfs, D., Härtling, T., Miszta, K., Bigall, N. C., Kim, M. R., Genovese, A., Falqui, A., Povia, M., Manna, L. Reversible Tunability of the Near-Infrared Valence Band Plasmon Resonance in Cu_{2-x}Se Nanocrystals. *Journal of the American Chemical Society* **133**, 11175-11180, (2011).
- 33 Hsu, S.-W., On, K., Tao, A. R. Localized Surface Plasmon Resonances of Anisotropic Semiconductor Nanocrystals. *Journal of the American Chemical Society* **133**, 19072-19075, (2011).
- 34 Kriegel, I., Jiang, C., Rodríguez-Fernández, J., Schaller, R. D., Talapin, D. V., da Como, E., Feldmann, J. Tuning the Excitonic and Plasmonic Properties of Copper Chalcogenide Nanocrystals. *Journal of the American Chemical Society* **134**, 1583-1590, (2012).
- 35 Hsu, S.-W., Bryks, W., Tao, A. R. Effects of Carrier Density and Shape on the Localized Surface Plasmon Resonances of Cu_{2-x}S Nanodisks. *Chemistry of Materials* **24**, 3765-3771, (2012).

- 36 Zhao, Y., Pan, H., Lou, Y., Qiu, X., Zhu, J., Burda, C. Plasmonic Cu_{2-x}S Nanocrystals: Optical and Structural Properties of Copper-Deficient Copper(I) Sulfides. *Journal of the American Chemical Society* **131**, 4253-4261, (2009).
- 37 Li, W., Shavel, A., Guzman, R., Rubio-Garcia, J., Flox, C., Fan, J., Cadavid, D., Ibanez, M., Arbiol, J., Morante, J. R., Cabot, A. Morphology Evolution of Cu_{2-x}S Nanoparticles: From Spheres to Dodecahedrons. *Chemical Communications* **47**, 10332-10334, (2011).
- 38 Kriegel, I., Rodríguez-Fernández, J., Como, E. D., Lutich, A. A., Szeifert, J. M., Feldmann, J. Tuning the Light Absorption of Cu_{1.97}S Nanocrystals in Supercrystal Structures. *Chemistry of Materials* **23**, 1830-1834, (2011).
- 39 Kriegel, I., Rodríguez-Fernández, J., Wisnet, A., Zhang, H., Waurisch, C., Eychemuller, A., Dubavik, A., Govorov, A. O., Feldmann, J. Shedding Light on Vacancy-Doped Copper Chalcogenides: Shape-Controlled Synthesis, Optical Properties, and Modeling of Copper Telluride Nanocrystals with Near-Infrared Plasmon Resonances. *ACS Nano*, Doi: 10.1021/nn400894d, (2013).
- 40 Mulder, B. J. Optical properties of crystals of cuprous sulphides (chalcosite, djurleite, Cu_{1.9}S, and digenite). *Physica Status Solidi (a)* **13**, 79-88, (1972).
- 41 Hariharan, P. *Basics of Interferometry*. (Elsevier Science, 2010).
- 42 Scotognella, F., Della Valle, G., Srimath Kandada, A. R., Dorfs, D., Zavelani-Rossi, M., Conforti, M., Miszta, K., Comin, A., Korobchevskaya, K., Lanzani, G., Manna, L., Tassone, F. Plasmon Dynamics in Colloidal Cu_{2-x}Se Nanocrystals. *Nano Letters* **11**, 4711-4717, (2011).
- 43 Alivisatos, A. P. Perspectives on the Physical Chemistry of Semiconductor Nanocrystals. *The Journal of Physical Chemistry* **100**, 13226-13239, (1996).
- 44 Kreibig, U., Vollmer, M. *Optical Properties of Metal Clusters*. (Springer, 2010).
- 45 Kruszynska, M., Borchert, H., Bachmatiuk, A., Rummeli, M. H., Büchner, B., Parisi, J., Kolny-Olesiak, J. Size and Shape Control of Colloidal Copper(I) Sulfide Nanorods. *ACS Nano* **6**, 5889-5896, (2012).
- 46 Li, H., Zanella, M., Genovese, A., Povia, M., Falqui, A., Giannini, C., Manna, L. Sequential Cation Exchange in Nanocrystals: Preservation of Crystal Phase and Formation of Metastable Phases. *Nano Letters* **11**, 4964-4970, (2011).
- 47 Miszta, K., Dorfs, D., Genovese, A., Kim, M. R., Manna, L. Cation Exchange Reactions in Colloidal Branched Nanocrystals. *ACS Nano* **5**, 7176-7183, (2011).

- 48 Luther, J. M., Zheng, H., Sadtler, B., Alivisatos, A. P. Synthesis of PbS Nanorods and Other Ionic Nanocrystals of Complex Morphology by Sequential Cation Exchange Reactions. *Journal of the American Chemical Society* **131**, 16851-16857, (2009).
- 49 Son, D. H., Hughes, S. M., Yin, Y., Paul Alivisatos, A. Cation Exchange Reactions in Ionic Nanocrystals. *Science* **306**, 1009-1012, (2004).
- 50 Jain, P. K., Amirav, L., Aloni, S., Alivisatos, A. P. Nanoheterostructure Cation Exchange: Anionic Framework Conservation. *Journal of the American Chemical Society* **132**, 9997-9999, (2010).
- 51 Robinson, R. D., Sadtler, B., Demchenko, D. O., Erdonmez, C. K., Wang, L.-W., Alivisatos, A. P. Spontaneous Superlattice Formation in Nanorods Through Partial Cation Exchange. *Science* **317**, 355-358, (2007).
- 52 Kittel, C. *Introduction to Solid State Physics*. (John Wiley & Sons, 2004).
- 53 Ashcroft, N. W., Mermin, D. N. *Festkörperphysik*. (Oldenbourg Wissenschaftsverlag, 2007).
- 54 Hunklinger, S. *Festkörperphysik*. (Oldenbourg Wissensch. Vlg, 2009).
- 55 Johnson, P. B., Christy, R. W. Optical Constants of the Noble Metals. *Physical Review B* **6**, 4370-4379, (1972).
- 56 García de Abajo, F. J., Howie, A. Relativistic Electron Energy Loss and Electron-Induced Photon Emission in Inhomogeneous Dielectrics. *Physical Review Letters* **80**, 5180-5183, (1998).
- 57 García de Abajo, F. J., Howie, A. Retarded field calculation of electron energy loss in inhomogeneous dielectrics. *Physical Review B* **65**, 115418-115417, (2002).
- 58 Mie, G. Beiträge zur Optik trüber Medien, speziell kolloidaler Metallösungen. *Annalen der Physik* **330**, 377-445, (1908).
- 59 Rodríguez-Lorenzo, L., de la Rica, R., Álvarez-Puebla, R. A., Liz-Marzán, L. M., Stevens, M. M. Plasmonic nanosensors with inverse sensitivity by means of enzyme-guided crystal growth. *Nat Mater* **11**, 604-607, (2012).
- 60 de la Rica, R., Stevens, M. M. Plasmonic ELISA for the ultrasensitive detection of disease biomarkers with the naked eye. *Nat Nano* **7**, 821-824, (2012).
- 61 Mulvaney, P. Surface Plasmon Spectroscopy of Nanosized Metal Particles. *Langmuir* **12**, 788-800, (1996).
- 62 Link, S., El-Sayed, M. A. Spectral Properties and Relaxation Dynamics of Surface Plasmon Electronic Oscillations in Gold and Silver Nanodots and Nanorods. *The Journal of Physical Chemistry B* **103**, 8410-8426, (1999).

- 63 Kreibig, U., Fragstein, C. v. The limitation of electron mean free path in small silver particles. *Zeitschrift für Physik* **224**, 307-323, (1969).
- 64 Link, S., Mohamed, M. B., El-Sayed, M. A. Simulation of the Optical Absorption Spectra of Gold Nanorods as a Function of Their Aspect Ratio and the Effect of the Medium Dielectric Constant. *The Journal of Physical Chemistry B* **103**, 3073-3077, (1999).
- 65 Gans, R. Über die Form ultramikroskopischer Goldteilchen. *Annalen der Physik* **342**, 881-900, (1912).
- 66 Kelly, K. L., Coronado, E., Zhao, L. L., Schatz, G. C. The Optical Properties of Metal Nanoparticles: The Influence of Size, Shape, and Dielectric Environment. *The Journal of Physical Chemistry B* **107**, 668-677, (2003).
- 67 Draine, B. T., Flatau, P. J. Discrete-dipole approximation for scattering calculations. *Journal of the Optical Society of America A* **11**, 1491-1499, (1994).
- 68 Hutter, E., Fendler, J. H. Exploitation of Localized Surface Plasmon Resonance. **16**, 1685-1706, (2004).
- 69 Willets, K. A., Van Duyne, R. P. Localized Surface Plasmon Resonance Spectroscopy and Sensing. *Annual Review of Physical Chemistry* **58**, 267-297, (2007).
- 70 Pinchuk, A. O., Schatz, G. C. Nanoparticle optical properties: Far- and near-field electrodynamic coupling in a chain of silver spherical nanoparticles. *Materials Science and Engineering: B* **149**, 251-258, (2008).
- 71 Lazarides, A. A., Lance Kelly, K., Jensen, T. R., Schatz, G. C. Optical properties of metal nanoparticles and nanoparticle aggregates important in biosensors. *Journal of Molecular Structure: THEOCHEM* **529**, 59-63, (2000).
- 72 Petryayeva, E., Krull, U. J. Localized surface plasmon resonance: Nanostructures, bioassays and biosensing—A review. *Analytica Chimica Acta* **706**, 8-24, (2011).
- 73 Perner, M., Bost, P., Lemmer, U., von Plessen, G., Feldmann, J., Becker, U., Mennig, M., Schmitt, M., Schmidt, H. Optically Induced Damping of the Surface Plasmon Resonance in Gold Colloids. *Physical Review Letters* **78**, 2192-2195, (1997).
- 74 Link, S., El-Sayed, M. A. Shape and size dependence of radiative, non-radiative and photothermal properties of gold nanocrystals. *International Reviews in Physical Chemistry* **19**, 409-453, (2000).
- 75 Tang, C. W., VanSlyke, S. A. Organic electroluminescent diodes. *Applied Physics Letters* **51**, 913-915, (1987).

- 76 Kim, H., Pique, A., Horwitz, J. S., Mattoussi, H., Murata, H., Kafafi, Z. H., Chrisey, D. B. Indium tin oxide thin films for organic light-emitting devices. *Applied Physics Letters* **74**, 3444-3446, (1999).
- 77 Kim, H., Gilmore, C. M., Pique, A., Horwitz, J. S., Mattoussi, H., Murata, H., Kafafi, Z. H., Chrisey, D. B. Electrical, optical, and structural properties of indium--tin--oxide thin films for organic light-emitting devices. *Journal of Applied Physics* **86**, 6451-6461, (1999).
- 78 Brewer, S. H., Franzen, S. Indium Tin Oxide Plasma Frequency Dependence on Sheet Resistance and Surface Adlayers Determined by Reflectance FTIR Spectroscopy. *The Journal of Physical Chemistry B* **106**, 12986-12992, (2002).
- 79 Salje, E., Güttler, B. Anderson transition and intermediate polaron formation in WO_{3-x} Transport properties and optical absorption. *Philosophical Magazine Part B* **50**, 607-620, (1984).
- 80 Evans, H. T. Djurleite ($Cu_{1.94}S$) and Low Chalcocite (Cu_2S): New Crystal Structure Studies. *Science* **203**, 356-358, (1979).
- 81 Evans, H. T. Crystal Structure of Low Chalcocite. *Nature Physical Science* **232**, 69-70, (1971).
- 82 Riha, S. C., Johnson, D. C., Prieto, A. L. Cu_2Se Nanoparticles with Tunable Electronic Properties Due to a Controlled Solid-State Phase Transition Driven by Copper Oxidation and Cationic Conduction. *Journal of the American Chemical Society* **133**, 1383-1390, (2011).
- 83 Manisha, K., Tsuyoshi, H., Kazuya, T., Kazuhiro, Y., Masakazu, A. Structural studies of copper sulfide films: effect of ambient atmosphere. *Science and Technology of Advanced Materials* **9**, 035011, (2008).
- 84 Putnis, A. The transformation behaviour of cuprous sulphides and its application to the efficiency of Cu_xS -CdS solar cells. *Philosophical Magazine* **34**, 1083-1086, (1976).
- 85 Grozdanov, I., Najdoski, M. Optical and Electrical Properties of Copper Sulfide Films of Variable Composition. *Journal of Solid State Chemistry* **114**, 469-475, (1995).
- 86 Ellis, S. G. Flash Evaporation and Thin Films of Cuprous Sulfide, Selenide, and Telluride. *Journal of Applied Physics* **38**, 2906-2912, (1967).
- 87 Pfisterer, F. The wet-topotaxial process of junction formation and surface treatments of Cu_2S -CdS thin-film solar cells. *Thin Solid Films* **431-432**, 470-476, (2003).

- 88 Mansour, B. A., Demian, S. E., Zayed, H. A. Determination of the effective mass for highly degenerate copper selenide from reflectivity measurements. *Journal of Materials Science: Materials in Electronics* **3**, 249-252, (1992).
- 89 Lukashev, P., Lambrecht, W. R. L., Kotani, T., van Schilfgaarde, M. Electronic and crystal structure of Cu_{2-x}S : Full-potential electronic structure calculations. *Physical Review B* **76**, 195202-195214, (2007).
- 90 Moss, T. S. The Interpretation of the Properties of Indium Antimonide. *Proceedings of the Physical Society. Section B* **67**, 775, (1954).
- 91 Burstein, E. Anomalous Optical Absorption Limit in InSb. *Physical Review* **93**, 632-633, (1954).
- 92 Wu, Y., Wadia, C., Ma, W., Sadtler, B., Alivisatos, A. P. Synthesis and Photovoltaic Application of Copper(I) Sulfide Nanocrystals. *Nano Letters* **8**, 2551-2555, (2008).
- 93 Wadia, C., Alivisatos, A. P., Kammen, D. M. Materials Availability Expands the Opportunity for Large-Scale Photovoltaics Deployment. *Environmental Science & Technology* **43**, 2072-2077, (2009).
- 94 Klimov, V., Bolivar, P. H., Kurz, H., Karavanskii, V., Krasovskii, V., Korkishko, Y. Linear and nonlinear transmission of Cu_xS quantum dots. *Applied Physics Letters* **67**, 653-655, (1995).
- 95 Klimov, V. I., Karavanskii, V. A. Mechanisms for optical nonlinearities and ultrafast carrier dynamics in Cu_xS nanocrystals. *Physical Review B* **54**, 8087, (1996).
- 96 Lou, Y., Chen, X., Samia, A. C., Burda, C. Femtosecond Spectroscopic Investigation of the Carrier Lifetimes in Digenite Quantum Dots and Discrimination of the Electron and Hole Dynamics via Ultrafast Interfacial Electron Transfer. *The Journal of Physical Chemistry B* **107**, 12431-12437, (2003).
- 97 Yumashev, K. V., Prokoshin, P. V., Malyarevich, A. M., Mikhailov, V. P., Artemyev, M. V., Gurin, V. S. Optical transient bleaching and induced absorption of surface-modified copper sulfide nanocrystals. *Applied Physics B: Lasers & Optics* **64**, 73, (1997).
- 98 Brelle, M. C., Torres-Martinez, C. L., McNulty, J. C., Mehra, R. K., Zhang, J. Z. Synthesis and Characterization of Cu_xS Nanoparticles. Nature of the Infrared Band and Charge-Carrier Dynamics. *Pure and Applied Chemistry* **72**, 101-117, (2000).
- 99 Deka, S., Genovese, A., Zhang, Y., Miszta, K., Bertoni, G., Krahn, R., Giannini, C., Manna, L. Phosphine-Free Synthesis of p-Type Copper(I) Selenide Nanocrystals in

- Hot Coordinating Solvents. *Journal of the American Chemical Society* **132**, 8912-8914, (2010).
- 100 Gagne, R. R., Koval, C. A., Smith, T. J. Binuclear complexes of macrocyclic ligands. A mixed-valence copper(II)-copper(I) complex which exhibits unusual temperature-dependent behavior. *Journal of the American Chemical Society* **99**, 8367-8368, (1977).
- 101 Long, R. C., Hendrickson, D. N. Intramolecular electron transfer in a series of mixed-valence copper(II)-copper(I) complexes. *Journal of the American Chemical Society* **105**, 1513-1521, (1983).
- 102 Artemyev, M. V., Sviridov, D. V., Gaponik, N. P., Maljarevich, A. M. Sensitivity of Nanocrystalline Copper Sulfide/Cadmium Sulfide Heterojunction in Near-Ir Region. *MRS Online Proceedings Library* **417**, null-null, (1995).
- 103 Zhuang, Z., Peng, Q., Zhang, B., Li, Y. Controllable Synthesis of Cu₂S Nanocrystals and Their Assembly into a Superlattice. *Journal of the American Chemical Society* **130**, 10482-10483, (2008).
- 104 Haram, S. K., Mahadeshwar, A. R., Dixit, S. G. Synthesis and Characterization of Copper Sulfide Nanoparticles in Triton-X 100 Water-in-Oil Microemulsions. *The Journal of Physical Chemistry* **100**, 5868-5873, (1996).
- 105 Larsen, T. H., Sigman, M., Ghezelbash, A., Doty, R. C., Korgel, B. A. Solventless Synthesis of Copper Sulfide Nanorods by Thermolysis of a Single Source Thiolate-Derived Precursor. *Journal of the American Chemical Society* **125**, 5638-5639, (2003).
- 106 Sigman, M. B., Ghezelbash, A., Hanrath, T., Saunders, A. E., Lee, F., Korgel, B. A. Solventless Synthesis of Monodisperse Cu₂S Nanorods, Nanodisks, and Nanoplatelets. *Journal of the American Chemical Society* **125**, 16050-16057, (2003).
- 107 Saunders, A. E., Ghezelbash, A., Smilgies, D.-M., Sigman, M. B., Korgel, B. A. Columnar Self-Assembly of Colloidal Nanodisks. *Nano Letters* **6**, 2959-2963, (2006).
- 108 http://www.nobelprize.org/nobel_prizes/physics/laureates/1914/present.html (2013-04-04).
- 109 http://www.nobelprize.org/nobel_prizes/physics/laureates/1915/ (2013-04-04).
- 110 Bawendi, M. G., Kortan, A. R., Steigerwald, M. L., Brus, L. E. X-ray structural characterization of larger CdSe semiconductor clusters. *The Journal of Chemical Physics* **91**, 7282-7290, (1989).

- 111 Pinna, N. in *Scattering Methods and the Properties of Polymer Materials* Vol. 130 *Progress in Colloid and Polymer Science* Ch. 4, 29-32 (Springer Berlin Heidelberg, 2005).
- 112 http://www.nobelprize.org/nobel_prizes/physics/laureates/1986/ruska-autobio.html (2012-11-01).
- 113 Williams, D. B., Carter, C. B. *Transmission Electron Microscopy: A Textbook for Materials Science*. (Springer, 2009).
- 114 http://www.nobelprize.org/nobel_prizes/physics/laureates/1929/press.html (2013-04-04).
- 115 Günzler, H., Gremlich, H.-U. *IR Spectroscopy*. (Wiley-VCH Verlag, 2002).
- 116 <http://www.chem.agilent.com/Library/usermanuals/Public/1972.pdf> (2013-02-12).
- 117 http://www.chem.agilent.com/Library/flyers/Public/5991-1717EN_PromoFlyer_UV_DRA.pdf (2013-04-04).
- 118 Lakowicz, J. R. *Principles of Fluorescence Spectroscopy*. 3rd edn, (Springer, 2006).
- 119 www.horiba.com/fileadmin/uploads/Scientific/Documents/Fluorescence/flogcat.pdf (2013-04-04).
- 120 Klimov, V. I. Optical Nonlinearities and Ultrafast Carrier Dynamics in Semiconductor Nanocrystals. *The Journal of Physical Chemistry B* **104**, 6112-6123, (2000).
- 121 <http://learn.hamamatsu.com/tutorials/java/streakcamera/> (2013-02-12).
- 122 Cerullo, G., Manzoni, C., Luer, L., Polli, D. Time-resolved methods in biophysics. 4. Broadband pump-probe spectroscopy system with sub-20 fs temporal resolution for the study of energy transfer processes in photosynthesis. *Photochemical & Photobiological Sciences* **6**, 135-144, (2007).
- 123 Sang-Hyun Choi, Kwangjin An, Eung-Gyu Kim, Jung Ho Yu, Jeong Hyun Kim, Taeghwan Hyeon. Simple and Generalized Synthesis of Semiconducting Metal Sulfide Nanocrystals. *Advanced Functional Materials* **19**, 1645-1649, (2009).
- 124 Saunders, A. E., Ghezelbash, A., Sood, P., Korgel, B. A. Synthesis of High Aspect Ratio Quantum-Size CdS Nanorods and Their Surface-Dependent Photoluminescence. *Langmuir* **24**, 9043-9049, (2008).
- 125 Wang, W., Banerjee, S., Jia, S., Steigerwald, M. L., Herman, I. P. Ligand Control of Growth, Morphology, and Capping Structure of Colloidal CdSe Nanorods. *Chemistry of Materials* **19**, 2573-2580, (2007).

- 126 Yu, W. W., Wang, Y. A., Peng, X. Formation and Stability of Size-, Shape-, and Structure-Controlled CdTe Nanocrystals: Ligand Effects on Monomers and Nanocrystals. *Chemistry of Materials* **15**, 4300-4308, (2003).
- 127 Shieh, F., Saunders, A. E., Korgel, B. A. General Shape Control of Colloidal CdS, CdSe, CdTe Quantum Rods and Quantum Rod Heterostructures. *The Journal of Physical Chemistry B* **109**, 8538-8542, (2005).
- 128 Yu, W. W., Qu, L., Guo, W., Peng, X. Experimental Determination of the Extinction Coefficient of CdTe, CdSe, and CdS Nanocrystals. *Chemistry of Materials* **15**, 2854-2860, (2003).
- 129 Gorbachev, V. V., Putilin, I. M. Some parameters of band structure in copper selenide and telluride. *Physica Status Solidi (a)* **16**, 553-559, (1973).
- 130 Chen, H., Kou, X., Yang, Z., Ni, W., Wang, J. Shape- and Size-Dependent Refractive Index Sensitivity of Gold Nanoparticles. *Langmuir* **24**, 5233-5237, (2008).
- 131 Link, S., El-Sayed, M. A. Size and Temperature Dependence of the Plasmon Absorption of Colloidal Gold Nanoparticles. *The Journal of Physical Chemistry B* **103**, 4212-4217, (1999).
- 132 Anisimov, S. I., Kapeliovich, B. L., Perel'man, T. L. Electron emission from metal surfaces exposed to ultrashort laser pulses. *Soviet Physics - JETP* **39**, 375-377, (1974).
- 133 Rogach, A. L., Talapin, D. V., Shevchenko, E. V., Kornowski, A., Haase, M., Weller, H. Organization of Matter on Different Size Scales: Monodisperse Nanocrystals and Their Superstructures. *Advanced Functional Materials* **12**, 653-664, (2002).
- 134 Shevchenko, E. V., Talapin, D. V., Murray, C. B., O'Brien, S. Structural Characterization of Self-Assembled Multifunctional Binary Nanoparticle Superlattices. *Journal of the American Chemical Society* **128**, 3620-3637, (2006).
- 135 Shevchenko, E. V., Talapin, D. V., Kotov, N. A., O'Brien, S., Murray, C. B. Structural diversity in binary nanoparticle superlattices. *Nature* **439**, 55-59, (2006).
- 136 Shevchenko, E. V., Kortright, J., Talapin, D. V., Aloni, S., Alivisatos, A. P. Quasi-ternary Nanoparticle Superlattices Through Nanoparticle Design. *Advanced Materials* **19**, 4183-4188, (2007).
- 137 Shevchenko, E. V., Ringler, M., Schwemer, A., Talapin, D. V., Klar, T. A., Rogach, A. L., Feldmann, J., Alivisatos, A. P. Self-Assembled Binary Superlattices of CdSe and Au Nanocrystals and Their Fluorescence Properties. *Journal of the American Chemical Society* **130**, 3274-3275, (2008).

- 138 Kovalenko, M. V., Bodnarchuk, M. I., Talapin, D. V. Nanocrystal Superlattices with Thermally Degradable Hybrid Inorganic-Organic Capping Ligands. *Journal of the American Chemical Society* **132**, 15124-15126, (2010).
- 139 Murray, C. B., Kagan, C. R., Bawendi, M. G. Self-Organization of CdSe Nanocrystallites into Three-Dimensional Quantum Dot Superlattices. *Science* **270**, 1335-1338, (1995).
- 140 Jain, P. K., El-Sayed, M. A. Plasmonic coupling in noble metal nanostructures. *Chemical Physics Letters* **487**, 153-164, (2010).
- 141 Miller, D. A. B., Chemla, D. S., Damen, T. C., Gossard, A. C., Wiegmann, W., Wood, T. H., Burrus, C. A. Band-Edge Electroabsorption in Quantum Well Structures: The Quantum-Confined Stark Effect. *Physical Review Letters* **53**, 2173-2176, (1984).
- 142 Bawendi, M. G., Steigerwald, M. L., Brus, L. E. The Quantum-Mechanics of Larger Semiconductor Clusters (Quantum Dots). *Annual Review of Physical Chemistry* **41**, 477-496, (1990).
- 143 Schaller, R. D., Sykora, M., Jeong, S., Klimov, V. I. High-Efficiency Carrier Multiplication and Ultrafast Charge Separation in Semiconductor Nanocrystals Studied via Time-Resolved Photoluminescence. *The Journal of Physical Chemistry B* **110**, 25332-25338, (2006).
- 144 Li, S., Wang, H., Xu, W., Si, H., Tao, X., Lou, S., Du, Z., Li, L. S. Synthesis and Assembly of Monodisperse Spherical Cu₂S Nanocrystals. *Journal of Colloid and Interface Science* **330**, 483-487, (2009).
- 145 Li, H., Brescia, R., Krahn, R., Bertoni, G., Alcocer, M. J. P., D'Andrea, C., Scotognella, F., Tassone, F., Zanella, M., De Giorgi, M., Manna, L. Blue-UV-Emitting ZnSe(Dot)/ZnS(Rod) Core/Shell Nanocrystals Prepared from CdSe/CdS Nanocrystals by Sequential Cation Exchange. *ACS Nano* **6**, 1637-1647, (2012).
- 146 Zhang, Y., Qiao, Z.-P., Chen, X.-M. Microwave-Assisted Elemental Direct Reaction Route to Nanocrystalline Copper Chalcogenides CuSe and Cu₂Te. *Journal of Materials Chemistry* **12**, 2747-2748, (2002).
- 147 Jiang, L., Zhu, Y.-J., Cui, J.-B. Nanostructures of Metal Tellurides (PbTe, CdTe, CoTe₂, Bi₂Te₃, and Cu₇Te₄) with Various Morphologies: A General Solvothermal Synthesis and Optical Properties. *European Journal of Inorganic Chemistry* **2010**, 3005-3011, (2010).
- 148 Palchik, O., Kerner, R., Zhu, Z., Gedanken, A. Preparation of Cu_{2-x}Te and HgTe by Using Microwave Heating. *Journal of Solid State Chemistry* **154**, 530-534, (2000).

- 149 Li, B., Xie, Y., Huang, J., Liu, Y., Qian, Y. Sonochemical Synthesis of Nanocrystalline Copper Tellurides Cu_7Te_4 and Cu_4Te_3 at Room Temperature. *Chemistry of Materials* **12**, 2614-2616, (2000).
- 150 Sadtler, B., Demchenko, D. O., Zheng, H., Hughes, S. M., Merkle, M. G., Dahmen, U., Wang, L.-W., Alivisatos, A. P. Selective Facet Reactivity during Cation Exchange in Cadmium Sulfide Nanorods. *Journal of the American Chemical Society* **131**, 5285-5293, (2009).
- 151 Yu, W. W., Peng, X. Formation of High-Quality CdS and Other II-VI Semiconductor Nanocrystals in Noncoordinating Solvents: Tunable Reactivity of Monomers¹³. *Angewandte Chemie* **114**, 2474-2477, (2002).
- 152 Farag, B. S., Khodier, S. A. Direct and Indirect Transitions in Copper Telluride Thin Films. *Thin Solid Films* **201**, 231-240, (1991).
- 153 Mott, N. The mobility edge since 1967. *Journal of Physics C: Solid State Physics* **20**, 3075, (1987).
- 154 Esch, V., Fluegel, B., Khitrova, G., Gibbs, H. M., Xu, J., Kang, K., Koch, S. W., Liu, L. C., Risbud, S. H., Peyghambarian, N. State Filling, Coulomb, and Trapping Effects in the Optical Nonlinearity of CdTe Quantum Dots in Glass. *Physical Review B* **42**, 7450-7453, (1990).

Acknowledgements

This dissertation would not have been possible without the support of a great number of people. First, I would like to thank my supervisor, Professor Jochen Feldmann, for the support and encouragement he showed me throughout my dissertation. The opportunities I had in his lab were exceptional. I want to gratefully thank for the scientific environment he provided, a greatly equipped laboratory and motivating discussions. A very important aspect I am deeply grateful for is the chances I had to gain scientific experience abroad through the possibility to attend international scientific conferences and the opportunity of a research stay abroad. The experience gained under his supervision paved my scientific way and will significantly influence my future career.

I am particularly grateful for the possibility given by Professor Dmitri Talapin to stay in his lab at the University of Chicago (UChicago) for a couple of month and the fruitful collaboration resulting thereof. I would like to show my gratitude to Prof. Richard Schaller for performing the pump-probe measurements within this work and for assisting with his advice. I would like to offer my special thanks to Prof. Sasha Govorov for his support throughout the last couple of month leading to the successful completion of a very inspiring work. I want to thank Prof. Lukas Schmidt-Mende for serving as my supervisor in the international doctorate program NanoBioTechnology (IDK-NBT).

I am deeply grateful to Dr. Jessica Rodríguez-Fernández who was guiding me through my PhD with generous support. I had the chance to benefit from her experience in close cooperation and I hope that also in future we will profit from a productive teamwork together. Many thanks go to Dr. Enrico Da Como for his assistance and his guidance during the first half of my PhD.

I would like to show my gratitude to the people from the Chair of Physical Chemistry and the Analytical Electron Microscopy Group of the LMU who served as mentors for any chemistry or structure related problems. Most of all I want to thank Dr. Johann M. Szeifert and Andreas Wisnet who supported me with their great knowledge and patience. Many thanks also go to Markus Döblinger, Alesia Ivanova, Hans Feckl, Mirjam Dogru and Benjamin Mandelmeier for helping me with measurements.

A special thank also goes to the international doctorate program NanoBioTechnology (IDK-NBT) and the graduate program of the Nanosystems Initiative Munich (NIM-GP) for their financial and scientific support, and for offering an exceptional interdisciplinary and international environment.

My time at the Photonics and Optoelectronics Group (PhOG) has been shaped by the group members. It is a great pleasure to thank everyone for their helpful discussions and friendship

over the past few years. Each of you was always open to questions, scientific discussions, problems related to experimental setups or chemistry. Here, a special thank goes to Dr. Enrico Da Como who patiently supported my first steps in the Sommerfeld-Keller. I would also like to thank Raphael Tautz for his support throughout any laser related issue, and Tom Limmer and Felix Deschler for their help. Anna Helfrich and Mrs. Vrankovic, who were always very supportive in the chemistry lab, are gratefully acknowledged. A special thank also goes to Michael Fedoruk, Alexander Ohlinger, Raphael Tautz, Alexander Urban, and Felix Deschler for their patient help in computer related problems. Many thanks go to my sister Franziska Kriegel, Silke Kirchner, Raphael Tautz, Paul Kühler, Spas Nedev, Maxi Berr, and Felix Deschler for their support during thesis writing. The graphical assistance of Christoph Hohmann from the Nanosystems Initiative Munich (NIM) is greatly acknowledged.

I had an excellent time at the PhOG group due to the great colleagues and friends that provided a brilliant scientific atmosphere and a joyful climate. I want to especially thank my office mates Silke Kirchner, Raphael Tautz and the varying undergraduates. We experienced some wonderful times together - not only at work - which further promoted a motivating working climate. I want to thank the entire PhOG group, present and former: Lidiya Osinkina, Michael Fedoruk, Christian Mauser, Sol Carretero Papalcios, Nicolas Bouchonville, Aliaksei Dubavik, Michael Carlson, Spas Nedev, Paul Kühler, Jaekwon Do, Maxi Berr, Verena Baumann, Anastasia Babynina, Calin Hrelescu, Alex Ohlinger, Shany Neyshtadt, Andrey Lutich, Andras Deak, Julia Baldauf, Alexander Urban, and Sara Rupich and Dmitry Baranov (both from UChicago) for some wonderful moments together. A particular thank goes to my colleague and special friend Silke Kirchner. The highly exciting discussions on the balcony about science and whatsoever were very inspiring and helped me come through any crisis. Thanks for all your true sympathies and friendship.

Finally, I would like to thank my family. A special thank goes to my parents who were guiding me through my life, supporting me in any decision, and always believed in me. This allowed me to find the right way and keep on going. A special thank goes to my little sister Franziska. I think about the many times we went for lunch and the scientific discussions we had at the breakfast table. Finally I want to thank Matthias for accompanying me throughout the last couple of years, the motivation he provided me during difficult times, and for being there for me in any moment. Their love, support, encouragement and guidance helped me to get this far.

CURRICULUM VITAE

SCIENTIFIC EXPERIENCE

- 2009 – Present **(anticipated) Ph.D. in Physics**, Ludwig-Maximilians-University (LMU), Munich
Thesis: Near-infrared plasmonics with vacancy doped semiconductor nanocrystals - Photonics and Optoelectronics Group, Advisor: Prof. Dr. J. Feldmann
- 10/10-12/10 **Research visit at the Talapin Group (Department of Chemistry)**
Synthesis and characterization of semiconductor nanocrystals at the University of Chicago, Chicago, IL, USA
Advisor: Prof. Dr. D. Talapin
- 2007 – 2009 **Excellence Program Advanced Materials Science ('Excellent')**, Technical University Munich, Ludwig-Maximilians-University Munich and University of Augsburg
Thesis: Morphology correlated observation of charge transfer excitons in polymer/fullerene solar cells - Photonics and Optoelectronics Group, Chair of Prof. Dr. J. Feldmann
- 08/08-09/08 **Industrial Research** at the Siemens AG, Corporate Technology, Materials and Microsystems
Preparation and functionalization of mesoporous ceramics with sol-gel techniques for photocatalytic application
- 2004 – 2007 **Bachelor's Program Molecular Science ('very good')**, Friedrich-Alexander-University Erlangen-Nuremberg
Thesis: Stationary and time-resolved absorption and emission of functionalized single-wall carbon nanotubes - Physical Chemistry I, Chair of Prof. Dr. D. M. Guldi

SCHOLARSHIPS AND AWARDS

- 2009 – Present Member of the **International Doctorate Program NanoBioTechnology (IDK-NBT)**
- 2009 – Present Member of the **NIM Graduate Program**
- 2012 **CeNS Publication Award**
Tuning the Excitonic and Plasmonic Properties of Copper Chalcogenide Nanocrystals I. Kriegel, C. Jiang, J. Rodríguez-Fernández, R. D. Schaller, D. V. Talapin, E. da Como, and J. Feldmann, *J. Am. Chem. Soc.* 134, 1583–1590 (2012)
- 2012 **Best Poster Presentation Award**, 'NANAX 4 Nanoscience with Nanocrystals International Conference', Tutzing, Germany

FURTHER QUALIFICATIONS

- 2011 **Student Representative of the IDK-NBT**
- 2009 – Present **NIM-Mentoring-Program** as mentor for highly motivated and skilled pupils in physics, chemistry, and materials science
- 2009 – Present **Teaching Responsibility** at the Department of Physics (LMU)
- 2009 – Present Professional training as a dancer and ballet teacher graduated with the 'Teaching Certificate' awarded by the 'Royal Academy of Dance', England